Larhyss Journal, ISSN 1112-3680, n°64, Dec 2025, pp. 199-324

Monograph

EXACT THEORETICAL RATING LAW FOR SHARP-CRESTED ELLIPTIC, SEMI-ELLIPTIC, AND CIRCULAR WEIRS

ACHOUR B.[1]*, *AMARA L.*[2], *KULKARNI K.H.*[3]

[1] Professor, Research laboratory in subterranean and surface hydraulics (LARHYSS), University of Biskra, PO Box 145 RP, Biskra, Algeria
[2] Associate Professor, Department of Civil Engineering and Hydraulics, Faculty of Science and Technology, University of Jijel, PO Box 98, Jijel, Algeria
[3]Associate Professor, Department of Civil Engineering, Dr Vishwanath Karad MIT World Peace University, 411038, Pune, India

(*) bachir.achour@larhyss.net

Research Article – Available at http://larhyss.net/ojs/index.php/larhyss/index
Received March 18, 2025, Received in revised form November 19, 2025, Accepted November 22, 2025

ABSTRACT

The study derives an exact theoretical (loss-free) stage-discharge law for sharp-crested elliptic and semi-elliptic weirs, with the circular weir obtained as a rigorous specialization. The formulation cleanly separates universal hydraulic scaling from a dimensionless geometry-flow depth kernel, which is make analytically explicit by converting the defining integral into an exact Euler–Beta series valid on the full admissible range.

The kernel is shown to satisfy the two endpoint constraints by construction, square-root onset at small flow depth and the full-height anchor equal to 4/15, providing a transparent, first-principles reference for analysis and calibration. Building on this foundation, the study constructs a compact Padé-type surrogate with four-significant-figure coefficients that preserves the governing physics and achieves uniform, sub-0.05% deviation from the exact series; the worst case, = 0.04%, is near the upper range; even smaller at full height.

The result is a unified, practice-ready evaluator: differentiable for sensitivity, numerically stable across the entire range, and straightforward to implement in design tools and real-time control.

Because the theory isolates geometry from losses, discharge coefficients can be appended multiplicatively without contaminating the kernel, preserving the correct ordering between theoretical and actual discharge.

A table and error curve benchmark the Padé law against the exact series, confirming near-reference accuracy with computational economy suitable for design charts, calibration workflows, and embedded applications.

This work thus replaces empirical or fitted surrogates, with a shape-exact analytic kernel and a compact Padé evaluator of the theoretical discharge. Multiply the theoretical flow-rate relationship by the site-calibrated discharge coefficient C_d to obtain the operational stage-discharge relationship.

The in-depth sensitivity analysis section rigorously examines how variations in key physical and geometric parameters affect the theoretical discharge over elliptic and circular weirs.

In addition, the authors advance a suite of semi-empirical C_d -models, eight models, rigorously derived from canonical closed-form mathematical kernels, such as Hill/Michaelis–Menten saturations and stretched-exponential Weibull forms, and carefully tailored to the hydraulics of elliptic, semi-elliptic, and circular weirs. The in-depth analysis of the elasticity of C_d on each of the model parameters is also presented.

Keywords: Elliptic weirs, Circular weirs, Discharge law, Analytical modeling, Beta function, Padé approximation, Sensitivity analysis.

INTRODUCTION

Over the last few years, Achour and collaborators have advanced a first-principles, design-to-deployment program for flow metering: derive shape-exact relationships from momentum and energy equations, express the dependence through compact, implementable formulas, and validate against targeted laboratory datasets, thereby delivering meters and weirs that are both traceable to theory and ready for practice (Achour and Amara, 2021a; 2021b; 2021c, 2021-d; 2022a; 2022b, 2022c; 2022d; 2023a, 2023b; 2023c; 2024; Achour et al., 2025).

The line culminates in a modified H-flume that is developed and experimentally validated for accurate discharge measurement in rectangular channels, extending the family of standard flumes with a clear calibration pathway (Achour et al., 2025). In parallel, a new trapezoidal flume is introduced with full treatment, design, theory, and experiment, showcasing the same integration of analysis and metrology (Achour et al., 2024). Together these contributions emphasize repeatable geometry, explicit rating relationships, and laboratory-grade verification before field transfer (Achour et al., 2025; Achour et al., 2024).

Innovations across meter families is the recent work spans specialized triangular devices and flumes: the 2A triangular weir, including design, theory, and experiment, the SMBF flume, a shaped modular concept, and a curved-wall triangular flume (CWTF), each adding a distinct geometry with an explicit discharge relationship and supporting tests (Achour and Amara, 2023a; 2023b; Achour and De Lapray, 2023). Complementary studies refine jump control and stilling-basin compactness using strategically shaped sills, linking metering accuracy with downstream energy dissipation management (Achour, et al.; 2022e; Achour et al., 2022f).

Standard geometries, re-examined. Achour and Amara have produced accurate, closed discharge-coefficient relationship for widely used structures, the Crump weir, triangular broad-crested weirs, and rectangular broad-crested meters with lateral contraction, all framed to be directly usable in routine sizing and calibration (Achour and Amara, 2022a–c). In parallel, a sharp-edged width constriction meter was formulated and validated in Flow Measurement and Instrumentation, emphasizing reproducible laboratory calibration and compact prediction equations (Achour and Amara, 2022d). Earlier groundwork in rectangular and triangular sharp-crested weirs and parabolic weirs rounds out the catalog of thin-plate devices with transparent C_d relations (Achour and Amara, 2021a; 2022b; 2022c; 2022d).

A notable strand is the theoretical stage-discharge formulation for a circular sharp-crested weir, derived from critical-flow considerations and used as a physics-exact reference for rating and calibration (Amara and Achour, 2021). This work complements the broader catalogue by showing how a loss-free theoretical law can anchor practical meters and reveal where discharge coefficients and approach-velocity corrections matter most (Amara and Achour, 2021).

Across devices, Achour's group emphasizes (1) transparent derivations that isolate the controlling dimensionless parameters, contraction ratio, approach-flow terms, geometric proportions, (2) closed or compact relations for C_d or the rating curve that avoid black-box regressions, and (3) meticulous experimental validation with very small residuals, on the order of a few-tenths of a percent in representative campaigns (Achour et al., 2022f; Achour and Amara, 2022a; 2022b; 2022c; 2022d; 2023a–c; Achour et al., 2024; 2025). In one detailed study, more than a thousand measurements across multiple contraction rates yielded a maximum deviation ≈0.3% between theory and experiment, underscoring the reliability of the proposed relationships (Achour et al., 2022f).

This recent wave builds on earlier contributions to critical-flow metering, including the classic triangular-channel jump flowmeter, while generalizing to modern, compact geometries and controller-friendly formulations (Achour, 1989; Achour, 2013). In sum, the latest findings provide a coherent toolbox: shape-exact theory, short evaluators, and bench-tested calibrations that extend from triangular and rectangular families to trapezoidal and modified H-flumes, furnishing engineers with reliable, transferable rating laws for design and field use (Achour, 1989; Achour, 2013; Achour and Amara, 2021a; 2021b; 2021c; 2021d; 2022a; 2022b; 2022c; 202d; 2023a; 2023b; 2023c; Achour et al., 2024; 2025a; 2025b; 2025c).

Elliptic and semi-elliptic sharp-crested weirs occupy a distinctive niche in flow metering: their curved geometry concentrates discharge through a continuously varying width, offering compact structures with smooth stage–discharge behavior under free-flow conditions. Historically, the field has treated geometry largely through empirical coefficients or numerical quadrature, despite a long record of theoretical developments for nonrectilinear openings, including circular and elliptic forms (Greve, 1932; Stevens, 1957; Sommerfeld and Stallybrass, 1996; Swamee, 1988; Bijankhan and Ferro, 2018; Nicosia et al., 2023). What practitioners need is a formulation that is both traceable to first principles and practical at the point of use. The energy-equation route provides exactly that: it separates universal hydraulic scaling from a geometry- flow depth kernel that can be derived once for a shape family and then deployed with minimal computation (Vatankhah, 2010; 2011; 2016; 2018).

Within this framework, elliptic and semi-elliptic weirs admit a general, shape-exact theoretical stage-discharge law obtained by integrating elemental strips across the true aperture width. The resulting kernel can be expressed in closed analytic form, via elliptic integrals, and, for everyday engineering use, compressed with the method of undetermined coefficients into short, uniformly accurate surrogates whose errors are demonstrably small relative to experimental uncertainty (Vatankhah, 2011; 2016; 2018). Crucially, when the ellipse's semi-axes coincide, the same derivation collapses seamlessly to the circular case, reinforcing the unity of the approach and providing an internal consistency check (Vatankhah, 2010; Bijankhan and Ferro, 2018).

This theoretical hierarchy clarifies the role of discharge coefficients in practice. The theoretical (loss-free) relationship is the upper bound; actual discharges measured on site are necessarily lower because of velocity nonuniformity, contraction, and viscous losses, hence the need for a discharge coefficient $C_d < 1$ that maps reality to theory (Vatankhah, 2010; 2018). Analyses that reverse this ordering or imply $C_d > 1$ signal issues with data quality, instrumentation, or model setup. Recent critiques of semi-elliptical weir datasets illustrate precisely this point and argue against unnecessary reliance on brute-force quadrature when compact, accurate analytic approximations are available (Parsaie et al., 2025; Mohammed-Ali, 2012; Vatankhah, 2011; 2016).

For design and operations, the payoffs are concrete. A single, physics-exact kernel, paired with a short surrogate calibrated to four significant figures, supports: (1) capacity checks and diameter selection; (2) rapid generation of rating curves; (3) metrological traceability when calibrating C_d against laboratory or field data; and (4) transparent cross-comparison of legacy fits across elliptic, semi-elliptic, and circular configurations. Framed this way, the circular weir is not an isolated special case but a specialization of the same kernel architecture, ensuring consistency across the curved-weir family and a clean path from theory to practice (Vatankhah, 2010; Sommerfeld and Stallybrass, 1996; Bijankhan and Ferro, 2018).

The present work develops a physics-exact theoretical stage-discharge law for sharp-crested elliptic and semi-elliptic weirs, formulated so that universal hydraulic scaling is cleanly separated from a geometry-flow depth kernel. The authors first render that kernel analytically explicit by deriving an exact Euler–Beta series directly from the integral definition, thereby turning a long-recognized but implicit factor into a rigorous, verifiable object valid across the full admissible relative flow depth range. This exact representation captures both end-point behaviours, the square-root onset at small flow depths and the full-height anchor, by construction and without empirical tuning.

On this analytic foundation, the authors compress the kernel into a uniformly accurate Padé-type surrogate whose few coefficients are given to four significant figures. The surrogate preserves the governing physics at both ends of the range and achieves sub-0.05% deviations from the exact series, a level of accuracy that is negligible compared with uncertainties from discharge coefficients and instrumentation, precisely the balance needed for design charts, calibration workflows, and real-time implementation.

The formulation is intentionally unified across curved openings: the same kernel architecture governs elliptic, semi-elliptic, and, by specialization, circular apertures, with only the geometric scaling and admissible relative flow depth range changing by shape. Inserting the exact Beta-series into the benchmark discharge law yields a closed, loss-free evaluator for each geometry; the circular weir then appears naturally as a particular case of this framework rather than the primary focus.

This work derives the exact theoretical stage-discharge relationship for sharp-crested elliptic and semi-elliptic weirs, and, by rigorous specialization, for circular weirs as well, within a single, closed analytical framework. Unlike earlier treatments, which typically embed geometry within discharge coefficients, resort to numerical quadrature, or publish tabulated and fitted ratings, the present analysis builds the geometry-flow depth kernel analytically via Euler–Beta identities and integrates it into a physics-exact, loss-free law valid across the full admissible range. This closes a persistent gap in the literature by replacing surrogate calibrations with a transparent reference formulation that unifies elliptic, semi-elliptic, and circular apertures under the same kernel architecture, with only geometric scaling changing by shape, while no empirical tuning required.

Moreover, the analysis is situated within the classical and standards literature while addressing a gap it leaves: previous fitted forms emphasize global accuracy but do not enforce the exact end-point constraints. By contrast, the present normalization and Beta-series make those constraints explicit and provable, providing a transparent reference against which compact approximations can be judged.

GEOMETRIC AND ANALYTICAL METHODOLOGY

Elliptic weir geometry

Fig. 1 illustrates the geometry of an elliptic weir, which forms the foundation for deriving the theoretical discharge law. The diagram depicts an ellipse with the following features:

(1) Elliptical profile:

The weir is described by an ellipse with vertical semi-axis a and horizontal semi-axis b. The ellipse spans the vertical range $0 \le y \le 2a$.

(2) Local width function $T(y)$:

At any height y, the local width of the opening is denoted by $T(y)$. At the crest, $y = 0$, the opening vanishes $T(0) = 0$. At mid-height, i.e., $y = a$, the width is maximal, and $T(a)=2b$. At the top of the ellipse, i.e., $y = 2a$, the opening again closes, corresponding to $T(2a) = 0$

This variation captures the elliptical shape of the weir's aperture.

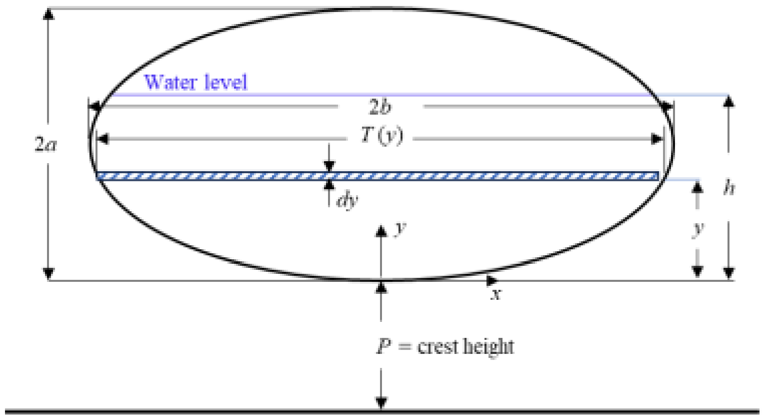

Figure 1: Geometry of the elliptic weir

In this frame, the following relationship expresses the local span $T(y)$ of an elliptic opening at a vertical coordinate y (Chow, 1959; Novak and al., 2010; Munson et al., 2013):

$$T(y) = 2b\sqrt{\frac{y}{a}\left(2-\frac{y}{a}\right)} \tag{1}$$

(3) Reference frame and water depth:

The vertical coordinate y is measured upward from the weir crest. The upstream flow depth of water above the crest height P is denoted by h. Thus, the flow depth is measured relative to the crest level P, with $0 \le h \le 2a$.

Theoretical stage–discharge law: Exact Euler–Beta kernel $\Psi(\beta)$ and loss-free rating

Fig. 1 sets up the mathematical framework by linking the elliptical geometry of the weir to its theoretical discharge characteristics. It visualizes the parameters a, b, h, and y, as well as the local opening width $T(y)$, which all feed into the exact discharge integral later derived in the paper.

With y from the crest and the upstream flow depth h above the crest height P, the ideal discharge, or the theoretical discharge, for both elliptical and semi-elliptical thin-crested weirs, is governed by the following relationship (Henderson, 1966; French, 1985; Bos, 1989):

$$Q_{Th} = \int_0^h T(y)\sqrt{2g(h-y)}\,dy \tag{2}$$

where the subscript "*Th*" denotes "Theoretical. Thus, Eq. (2) integrates the local elliptical width $T(y)$ against the Torricelli velocity Kernel.

By denoting $z = y/h$ and $\zeta = h/(2a)$, and $\beta = h/2a$, one may write what follows:

$0 \le z \le 1$, since $0 \le y \le 2a$ and $0 \le h \le 2a$, $0 \le \beta \le 1$, and $dy = h\ dz$. The infinitesimal element dy, or the very small vertical thickness of the water nappe, as represented in Fig 1, refers to a differential vertical segment within the flow domain, specifically used for the elemental discharge calculation through the elliptic weir.

Thus, Eq. (2) becomes as follows:

$$Q_{Th} = 4b\sqrt{2g}\, h^{3/2}\, \Psi(\beta) \tag{3}$$

where the function $\Psi(\beta)$ is written as follows:

$$\Psi(\beta) = \int_0^1 \sqrt{\beta z(1-\beta z)(1-z)}\, dz \tag{4}$$

In Eq. (3), the factor $\sqrt{(2g)} \times h^{3/2}$ comes directly from Torricelli's law and the dimensional dependence of discharge on flow depth. This part has nothing to do with the aperture shape; it would be the same for any thin-plate weir. The function $\Psi(\beta)$ is dimensionless. It contains only the effect of the ellipse geometry and how the upstream flow depth h "fills" that geometry, through β.

Moreover, in Eq. (3), or Eq. (4), $\Psi(\beta)$ is known as the dimensionless geometry-flow depth function that multiplies the Torricelli scale in the ideal, i.e., loss-free, rating law. It often called the "discharge Kernel". The prefactor $4b\sqrt{2g}\, h^{3/2}$ carries the physical units and the flow depth scaling, while $\Psi(\beta)$ collects all dependence on the aperture shape, i.e., the ellipse, and the vertical distribution of the flow depth within the opening.

Eq. (4) formally defines the following:

$$\Psi(\beta) = \int_0^1 f(z, \beta)\, dz \tag{4a}$$

where $f(z, \beta)$ is the integrand that combines the elliptic width function with the velocity distribution kernel.

Eq. (4) plays a pivotal role in the theoretical development because it explicitly isolates the geometry-flow depth interaction from the universal hydrodynamic scaling. The discharge law, expressed by Eq. (3), is structured so that all dimensional dependence and gravitational scaling are carried by the prefactor $\sqrt{2g}\, h^{3/2}$, while the dimensionless kernel $\Psi(\beta)$) captures only the geometric effect of the elliptic aperture. Herein, the parameter $\beta = h/(2a)$ directly links the upstream flow depth h to the full vertical axis $2a$, so that β represents the fraction of the ellipse's height that is submerged; it represents the penetration flow depth index. This ratio tells us how deeply the available flow depth "penetrates" the vertical extent of the aperture. Thus, this 'penetration' concept concerns the flow depth-to-aperture-height ratio $H/(2a)$, even if the gauge is located far upstream.

In this way, $\Psi(\beta)$ describes how the elliptical width distribution, when integrated against the Torricelli velocity kernel, adjusts the discharge relative to a simple $h^{3/2}$-law.

Thus, Eq. (4) defines the dimensionless discharge kernel $\Psi(\beta)$, which isolates the effect of geometry from the universal hydrodynamic scaling. While its explicit evaluation is deferred to later sections, two physical limits are already clear: (1) for small flow depths, i.e. $\beta \to 0$, incipient submergence dictates that $\Psi(\beta)$ must scale as $(\pi/8) \times \sqrt{\beta}$, and (2) for a fully wetted ellipse, i.e. $\beta = 1$, the kernel must reach the full-height condition $\Psi(1) = 4/15$. These limits will be rigorously derived and verified in the sequel, but they serve herein to illustrate the physical role played by Eq. (4).

Having defined the kernel $\Psi(\beta)$ in Eq. (4) and established its role as the geometry-flow depth function in the discharge law, the next task is to obtain an explicit analytical representation. Direct evaluation of the defining integral is not straightforward, but it admits an elegant reformulation through Euler's Beta function. By expanding the integrand in a uniformly convergent binomial series and integrating term by term, the kernel can be expressed as an exact infinite series involving Beta integrals. This approach not only provides a mathematically rigorous representation of $\Psi(\beta)$ valid for the full range $0 \le \beta \le 1$, but also connects the discharge kernel to classical special functions, laying the foundation for the asymptotic expansions and Padé-type approximations developed in the subsequent sections.

Write the integrand as follows:

$$\sqrt{\beta}\,\sqrt{z}\,\sqrt{(1-\beta z)}\,\sqrt{(1-z)} \tag{5}$$

and expand the last factor with the binomial series, valid and uniformly convergent for $0 \le \beta \le 1$, yields what follows:

$$(1-\beta z)^{1/2} = \sum_{n=0}^{\infty} \binom{\frac{1}{2}}{n} (-\beta z)^n \tag{6}$$

Term-by-term integration against what follows:

$$z^{1/2}(1-z)^{1/2} \tag{7}$$

yields the following Beta integrals:

$$\int_0^1 z^{n+1/2}(1-z)^{1/2}\,dz = \mathrm{B}\left(n+\frac{3}{2}, \frac{3}{2}\right) \tag{8}$$

Eq. (8) is precisely an instance, or an application, of the Euler Beta function. It evaluates an integral of the following form, by identifying it with $B\,(x, y)$:

$$\int_0^1 z^{\alpha}\left(1-z\right)^{\gamma}\,dz \tag{9}$$

However, Eq. (8) is not the definition of the Beta function, but a direct invocation of Euler's Beta identity, which is exactly what legitimizes the following exact series in Eq. (10).

Therefore, relationship (4) becomes as follows:

$$\Psi\left(\beta\right)=\sqrt{\beta}\sum_{n=0}^{\infty}\binom{\frac{1}{2}}{n}\left(-\beta\right)^{n}\mathrm{B}\left(n+\frac{3}{2},\frac{3}{2}\right) \tag{10}$$

This is the exact representation of $\Psi(\beta)$ expressed by the relationship (4). It is valid for both elliptic, semi-elliptic, and circular weirs. It evaluates the same geometry-driven function $\Psi(\beta)$, with $\beta = h/(2a)$ that comes from integrating the local elliptical width against the Torricelli velocity kernel. The only difference between "elliptic", "semi-elliptic", and circular weirs cases is the admissible relative flow depth range applying them on, i.e. $0 \le \beta \le 1$ for elliptic weirs, $0 \le \beta \le 0.5$ for semi-elliptic weirs, and $\beta = \xi = h/D$ for circular weirs of diameter $D = 2a$.

As an example, here's the four-term series expansion that follows directly from Eq. (10)'s Euler–Beta series, while taking $n = 0, 1, 2, 3$:

$$\Psi\left(\beta\right)=\frac{\pi}{8}\sqrt{\beta}-\frac{\pi}{32}\beta^{3/2}-\frac{5\,\pi}{1024}\beta^{5/2}-\frac{7\,\pi}{4096}\beta^{7/2}+O\left(\beta^{9/2}\right) \tag{10a}$$

Equivalently, factoring out the leading square-root onset yields the following:

$$\Psi\left(\beta\right)=\frac{\pi}{8}\sqrt{\beta}\left[1-\frac{1}{4}\beta-\frac{5}{128}\beta^{2}-\frac{7}{712}\beta^{3}+O\left(\beta^{4}\right)\right] \tag{10b}$$

As an illustrative example, let us examine the case where $\beta = 0.5$, which provides a clear indication of the series' convergence behavior and the rate at which the truncated form approaches the exact value.

Because the Euler–Beta series in Eq. (10b) is a binomial/Beta expansion with general term proportional to following, after factoring the onset $\sqrt{\beta}$:

$$\beta^{n}\,\mathrm{B}\left(n+\frac{3}{2},\frac{3}{2}\right) \tag{10c}$$

the terms decay essentially like

$$0.5^{n} \times n^{-3/2} \tag{10d}$$

At $\beta = 0.5$, this geometric factor dominates, so the truncation error is governed by the first neglected term.

A conservative bound using the alternating/binomial-term envelope and the following

$$\mathrm{B}\left(n+\frac{3}{2},\frac{3}{2}\right) \sim C\,n^{-3/2} \tag{10e}$$

shows that keeping up to $n = 10$; i.e., the first 11 terms $n = 0,\ldots,10$ in Eq. (10b)) makes the remainder smaller than 10^{-5} relative, that is, $\leq 0.001\%$, at $\beta = 0.5$. In practice, the decay is faster than the bound suggests; numerically the first 8 terms, $n = 0,\ldots,7$, already satisfy the same 0.001% target at $\beta = 0.5$, but $n = 10$ is a safe recommendation if users want a guaranteed margin.

As a practical recommendation for the users, truncate Eq. (10b) after $n = 10$ at $\beta = 0.5$ to ensure a maximum deviation ≤ 0.001 %; in many cases $n = 7$ suffices at this β.

Eqs. (10) - (10b) is the exact Euler–Beta series for the kernel $\Psi(\beta)$; after extracting the $\sqrt{\beta}$ factor, the remainder is a smooth power series with coefficients built from binomial factors and Beta integrals, giving the stated decay and fast convergence at $\beta = 0.5$.

The table below presents, for β varying within the practical range [0, 0.75] with a step of 0.05, the smallest truncation order n ensuring that the deviation between the exact and truncated forms of Eq. (10b) does not exceed 0.001%. The determination was based on a conservative bound for the first neglected term, as follows:

$$\frac{c\,\beta^{\,n+1}}{\left(n+1\right)^{3/2}} \leq 10^{-5},\ c = 0.5 \tag{10f}$$

It is emphasized that the computed n-values are deliberately over-minimal, slightly above the true minimal rank to ensure the 0.001% accuracy requirement under all practical β values.

β	Minimum truncation n (Deviation $\leq$ 0.001 %)
0	0
0.05	3
0.10	3
0.15	4
0.20	5
0.25	5
0.30	6
0.35	7
0.40	8
0.45	9
0.50	10
0.55	11
0.60	13

0.65	18
0.70	21
0.75	25

In view of the previous table, three relevant remarks can be pointed out: (1) The truncation order n increases sharply with β as the higher-order terms gain relative significance in the series expansion of Eq. (10b); (2) Beyond $\beta \approx 0.6$, the growth of n becomes quasi-exponential, indicating the series' slow convergence in the near-limit domain of $\beta \to 1$; (3) The proposed n-values remain conservatively accurate, ensuring that $\Psi(\beta)$ can be evaluated with negligible computational deviation, i.e., ≤ 0.001 %.

The following derived relationship for $n(\beta)$ provides a direct and reliable means of determining the minimum safe truncation order required to ensure that the truncated series representation of Eq. (10b) reproduces the exact function $\Psi(\beta)$ with a maximum deviation not exceeding 0.001 % over the full validity range $\beta \in [0, 0.75]$.

$$n(\beta) = 2.068 + 7.356\frac{\beta}{1-\beta} + 1.152\,\beta \tag{10g}$$

This analytical expression is of significant practical value because it allows the user to compute, for any given β, the smallest integer n that guarantees the target precision, without resorting to iterative convergence testing or empirical adjustment. The resulting formulation is deliberately over-minimal, providing a built-in safety margin that ensures the prescribed accuracy is met or not exceeded across the entire range of β.

It should be emphasized that the expression is not valid for $n = 0$, since the truncation of Eq. (10b) at zero order would fail to reproduce any of the functional behavior of $\Psi(\beta)$. Consequently, the practical domain of application begins at $n \geq 3$, or $\beta \geq 0.05$ according to the previous table, corresponding to the lowest truncation rank capable of achieving meaningful accuracy even at very small β.

The introduction of this compact formula thus provides both efficiency and consistency in analytical or computational applications. It enables users to determine the required series depth directly from the parameter β, ensuring that the approximate form of $\Psi(\beta)$ remains within the predefined tolerance limit of 0.001 % throughout the practical range of interest.

On the other hand, Eq. (10) is constructed to honor the physics at the ends of the range, matching the $(\pi/8) \times \sqrt{\beta}$ onset as $\beta \to 0$ and anchoring the full-height value at $\beta = 1$. That preserves the correct asymptotic while yielding a one-line formula that is easy to read, differentiate, and propagate through metrological.

For selected small β, one may compute the following:

(1) Exact $\Psi(\beta)$ from the exact Beta-series, i.e., Eq. (10);
(2) The asymptotic $A(\beta) \to (\pi/8) \times \sqrt{\beta}$;
(3) The ratios $\Psi(\text{exact})/A \to 1$ as $\beta \to 0$.

The numerical examples below corroborate the overmentioned statement:

For $\beta = 10^{-6}$, $\Psi(\text{exact}) = 3.92699\times10^{-4}$, $A = 3.92699\times10^{-4}$; $\Psi(\text{exact})/A = 1$.

For $\beta = 10^{-4}$, $\Psi(\text{exact}) = 3.9269\times10^{-3}$, $A = 3.92699\times10^{-3}$; $\Psi(\text{exact})/A = 0.999975$, $\Psi(\text{Pade})/A = 0.999723$; thus, the Padé relative error = 0.023%.

For $\beta = 10^{-2}$, $\Psi(\text{exact}) = 3.9172\times10^{-2}$, $A = 3.9270\times10^{-2}$; $\Psi(\text{exact})/A = 0.99727$.

Across all tested small β, varying from 10^{-6} to up to 0.10, $\Psi(\text{exact})/A$ remain very close to 1, confirming the $(\pi/8) \times \beta$ onset.

Across all tested small β, varying from 10^{-6} to up to 0.10, $\Psi(\text{exact})/A$ remain very close to 1, confirming the expected $(\pi/8) \times \beta$ onset.

It must be emphasized that in the classical hydraulics literature (e.g., Chow, 1959; Henderson, 1966; French, 1985; Bos, 1989), the dimensionless discharge function, often denoted $F(\eta)$, corresponding to $\Psi(\beta)/\sqrt{\beta}$, is introduced as the integral factor multiplying the universal flow depth law. In those works, however, the function is not evaluated in closed form; instead, its contribution is either tabulated from numerical quadrature or embedded into an empirical discharge coefficient C_d. Chow (1959) presents graphical solutions and tables of $F(\eta)$, while Henderson (1966) and French (1985) treat it implicitly, emphasizing experimental calibration of C_d. Bos (1989) systematically develops discharge-measurement structures using regression-based fitting laws, where $F(\eta)$ is absorbed into polynomial or rational expressions adjusted to experimental data. These procedures provided usable rating curves, but at the cost of relying on approximations or empirical fitting, since the explicit evaluation of the kernel was considered analytically intractable at the time.

Thus, in much of the hydraulics literature the dimensionless discharge function is introduced as an integral factor in the rating law and then treated empirically rather than evaluated in closed form. A prominent line of work by Vatankhah follows this curve-fitting paradigm: the flow depth-discharge relationship, or an equivalent Kernel $F(\eta)$, is first computed from laboratory data and/or numerically evaluated integrals over the admissible flow depth range, and then replaced by compact explicit formulas whose coefficients are identified by nonlinear regression (Vatankhah, 2010; 2012; 2021). This strategy yields practical, engineer-friendly expressions for circular and nonstandard sharp-crested weirs, but it does not furnish an analytic expansion of the Kernel itself, the dependence on η (or β) is ultimately parametric and data-calibrated.

This fitting philosophy extends to earlier and adjacent works, e.g., standard texts and engineering papers, where the Kernel's effect is absorbed into empirical discharge relations or compact flow depth-discharge equations tuned to experiments. In all such cases, the aim is practical accuracy with simple formulas, not an analytic expansion of the kernel itself. Near-crest asymptotic is not encoded, since fitting-based kernels, like those cited in the literature, are constructed to be O(1) and smooth at η (or β) $\rightarrow 0$, by design keeping the square-root behaviour outside the kernel. Consequently, they do not encode the incipient-submergence law $\Psi(\beta)\sim(\pi/8) \times \sqrt{\beta}$ within the kernel itself.

Moreover, no enforced full-height anchor is provided, since the fitted forms are tuned for small global error on $0 < \eta$ (or β) < 1 rather than to satisfy the exact end-point value $\Psi(1) = 4/15$. Hence the full-height condition is not guaranteed by construction.

The normalization used in the present study explains the difference. Indeed, the Kernel $\Psi(\beta)$ is defined so that all geometry-flow depth dependence stays inside Ψ; this is why the proper $\sqrt{\beta}$ onset and the $\beta = 1$ anchor can be imposed and proved for Ψ, then realized exactly via the Beta-series Eq. (10).

Eq. (10) advances beyond the traditional procedure, or the state of the art, by providing an exact, closed Beta-series representation of the kernel $\Psi(\beta)$. This formulation is not a reformulation of earlier results but a new development, and a new contribution: it recasts the integral definition of Eq. (4) into a rigorous convergent series involving Euler-Beta functions, valid uniformly on $0 \le \beta \le 1$. In so doing, Eq. (10) makes the kernel analytically explicit, opening the way for systematic asymptotic analysis, convergence checks, and direct numerical evaluation with guaranteed precision. Thus, while the existence of the integral kernel is well established in classical references, the exact Beta-series expansion of Eq. (10) appears herein for the first time. This distinction underscores the originality of the present work: it transforms a long-recognized but implicit discharge factor into a mathematically explicit, verifiable, and engineering-usable form. Eq. (10) provides a mathematically transparent and verifiable framework that bridges the integral formulation with precise analytical series, marking a genuine extension of classical weir theory.

Ultimately, Eq. (10) in this work provides an *exact* Euler–Beta series for the geometry-flow depth kernel $\Psi(\beta)$, obtained directly from the integral definition, i.e. Eq. (4), without recourse to empirical tuning, or any fitting procedure. The resulting representation is uniformly valid on $0 \le \beta \le 1$, encodes the $\Psi(\beta) \sim (\pi/8) \times \sqrt{\beta}$ onset and the $\Psi(1) = 4/15$ anchor by construction, and serves as a mathematically transparent benchmark against which any approximate, fitted, or reduced formulas may be assessed. In short, where prior work supplies *accurate fits*, Eq. (10) supplies the analytic object those fits approximate.

In addition, in Eq. (10), B denotes the Euler Beta function, which express as follows:

$$\mathrm{B}\left(n+\frac{3}{2},\frac{3}{2}\right)=\int_0^1 z^{\,n+1/2}\left(1-z\right)^{1/2} dz \tag{11}$$

In the Beta-function integral Eq. (11), the arguments $x = n + 3/2$ and $y = 3/2$ are positive, ensuring the convergence of Eq. (10).

Insertion of Eq. (10) into Eq. (3) leads to the exact theoretical discharge relationship valid for elliptic, semi-elliptic, and circular weirs. A detailed discussion of the circular configuration follows in a subsequent section:

$$Q_{Th} = 4b\sqrt{2g}\,h^{3/2}\sqrt{\beta}\sum_{n=0}^{\infty}\binom{\frac{1}{2}}{n}\left(-\beta\right)^{n}\mathrm{B}\left(n+\frac{3}{2},\frac{3}{2}\right) \tag{3a}$$

After rearrangement, Eq. (3a) can be rewritten in the following final form:

$$Q_{Th} = 2\sqrt{2}\frac{b}{\sqrt{a}}\sqrt{2g}\,h^2 \sum_{n=0}^{\infty}\binom{\frac{1}{2}}{n}(-\beta)^n \mathrm{B}\left(n+\frac{3}{2},\frac{3}{2}\right) \tag{3b}$$

Eq. (3a), or (3b), turns the benchmark rating law of Eq. (3) into an analytic evaluator: substituting the exact Beta-series of Eq. (10) for $\Psi(\beta)$ yields a closed, loss-free discharge formula that is uniformly valid on the full admissible range of flow depth for each geometry, i.e., elliptic: $0 \leq \beta \leq 1$; semi-elliptic: $0 \leq \beta \leq 0.5$; circular via the stated specialization. This is the exact theoretical discharge law sought, valid for the three overmentioned geometries. It preserves the core physics built into Ψ: the incipient-submergence onset $\Psi(\beta) \sim (\pi/8) \times \sqrt{\beta}$ and the full-height anchor $\Psi(1) = 4/15$. As a result, Eq. (3a) is both shape-exact, i.e., geometry handled by Ψ, and scale-exact, i.e., all dimensions carried by the Torricelli prefactor. Because $\Psi(\beta)$ in Eq. (3a) is given by a Euler–Beta series, the discharge becomes differentiable in closed form with respect to stage h and geometric parameters a and b. This enables trustworthy sensitivity, curvature, and uncertainty analyses, e.g., derivatives $\mathrm{d}Q/\mathrm{d}h$ and $\mathrm{d}^2Q/\mathrm{d}h^2$ used in error propagation and sensitivity study. Practically, the Beta series converges rapidly over $0 \leq \beta \leq 1$, so Eq. (3a) is both analytically transparent and computationally efficient, no empirical tuning, or fitting procedure, is required to achieve high precision. Unlike low-order fitted Kernels that are smooth O(1) functions of η (or β used herein) and do not enforce the $\sqrt{\beta}$ onset or the $\beta = 1$ anchor, Eq. (3a) inherits both limits by construction from the exact Kernel. Hence it serves as a physics-exact reference against which approximate rational forms, introduced later in the paper, or empirical relations can be objectively benchmarked across the entire flow depth range.

Eq. (3b) can be rewritten in the flowing reduced form:

$$Q_{Th} = 2\sqrt{2}\frac{b}{\sqrt{a}}\sqrt{2g}\,h^2\,\mathrm{P}(\beta) \tag{3c}$$

According to Eqs. (3a) and (10), the following can be written:

$$\mathrm{P}(\beta) = \frac{\Psi(\beta)}{\sqrt{\beta}} \tag{3d}$$

Thus, according to Eq. (10), one may write the following:

$$\mathrm{P}(\beta) = \sum_{n=0}^{\infty}\binom{\frac{1}{2}}{n}(-\beta)^n \mathrm{B}\left(n+\frac{3}{2},\frac{3}{2}\right) \tag{3e}$$

$\mathrm{P}(\beta)$ could be called the dimensionless discharge kernel for the elliptic and semi-elliptic weirs, or simply the elliptic kernel.

Eq. (3e) introduces the dimensionless discharge kernel for elliptic and semi-elliptic weirs, what the paper itself calls "the elliptic kernel." In plain terms, Eq. (3e) gathers all of the geometry–flow-depth coupling into a single, scale-free function of the nondimensional depth $\beta = h/(2a)$. All dimensional physics, $\sqrt{(2g)}$ and the overall h-scaling, is left in the outer Torricelli prefactor and the simple power of h; geometry lives inside the kernel.

Because Eq. (3e) descends from the exact Euler–Beta representation given earlier by Eq. (10), the kernel automatically enforces the two endpoint "anchors" of the theory, as follows:

(1) the incipient-submergence onset $\Psi(\beta) \sim (\pi/8) \times \sqrt{\beta}$ as $\beta \rightarrow 0$, Torricelli square-root, and
(2) the full-height value $\Psi(1) = 4/15$.

These are not fitted; they are consequences of the exact kernel.

Because the kernel in Eq. (3e) is given by a convergent Beta-series, the discharge law becomes analytically differentiable with respect to h and geometric parameters, crucial for sensitivity/elasticity analyses and error propagation.

The Beta series used to define the kernel converges rapidly on the full admissible β-range, so Eq. (3e) is both uniformly valid and computationally efficient; no empirical tuning is needed.

With the geometry isolated in the kernel, the flow-depth elasticity E_h, which will be developed later, becomes a clean combination of the outer h-power and one dimensionless derivative of the kernel. That structure lets the paper prove the correct endpoint limits directly from "kernel physics".

The exact kernel, underlying Eq. (3e), is non-analytic in β^2 and has a half-integer series starting with $(\pi/8) \times \sqrt{\beta}$, followed by $\beta^{3/2}\}$, $\beta^{5/2}$…. This is why successful global approximations factor out $\sqrt{\beta}$ and only approximate the smooth remainder. Eq. (3e) makes that structure explicit and preserves it exactly.

Eq. (3e) gives a shape-exact, scale-exact discharge law: geometry handled by the kernel; dimensions by the prefactor. It's a rigorous baseline against which compact fitted surrogates or empirical C_d-laws can be compared.

Because the kernel is analytic from the Beta-series, one can differentiate once or twice with respect to h or parameters, without leaving closed form; this is ideal for sensitivity, curvature, and uncertainty analyses used later in the paper.

In short, Eq. (3e) is the organizing principle of the elliptic/semi-elliptic rating: it isolates geometry in a dimensionless, physics-anchored kernel that is exact at both ends, uniformly accurate across the range, and tailor-made for robust sensitivity work.

Derivation of the exact β values

Leveraging the exact kernel in Eq. (10) together with the discharge law in Eq. (3a), the authors tabulate exact values of β as a function of the relative discharge denoted Q^*, which depends solely on $Q_{Th} = Q$, a, b, and g, admitting a maximum value 4/15 as $\Psi(1)$

is. The Table is presented and discussed in the theoretical Appendix A1, and draws the key inferences. Appendix A2, in turn, offers an analytic development of a practical approximation for the discharge coefficient C_d of a sharp-crested circular weir

Exact small-β series for $\Psi(\beta)$

To resolve the near-crest regime, where the upstream flow depth is small relative to the ellipse height, we extract a local asymptotic expansion of the geometry-flow depth kernel $\Psi(\beta)$ directly from its exact formulation. This small-β series exposes the non-analytic, half-integer structure of the Kernel, set by the Torricelli square-root, fixes the universal leading coefficient $(\pi/8) \times \sqrt{\beta}$, and determines the higher-order corrections that quantify how the elliptical geometry modifies the onset of discharge. In practice, the terms of the small-β expansion, namely the leading $(\pi/8) \times \sqrt{\beta}$ contribution together with the higher-order half-integer corrections $\propto \beta^{3/2}, \beta^{5/2}\ldots$ serve as benchmarks for numerics, certify the error of global approximations, and impose sharp constraints on compact closed-form laws at low flow depths.

Using the following:

$$\mathrm{B}\left(\frac{3}{2};\frac{3}{2}\right)=\frac{\pi}{8};\ \mathrm{B}\left(\frac{5}{2},\frac{3}{2}\right)=\frac{\pi}{16};\ \mathrm{B}\left(\frac{7}{2},\frac{3}{2}\right)=\frac{15\pi}{384}\ldots\text{with}$$

$$\binom{\frac{1}{2}}{0}=1;\ \binom{\frac{1}{2}}{1}=\frac{1}{2};\ \binom{\frac{1}{2}}{2}=-\frac{1}{8};\ \ldots.$$

One may obtain the following half-integer power series:

$$\Psi\left(\beta\right)=\frac{\pi}{8}\beta^{1/2}-\frac{\pi}{32}\beta^{3/2}-\frac{15\pi}{3072}\beta^{5/2}-\frac{7\pi}{4096}\beta^{7/2}-\ldots \tag{12}$$

This shows the correct near-origin behaviour:

$$\Psi\left(\beta\right)\sim\frac{\pi}{8}\sqrt{\beta} \tag{13}$$

which is non-analytic in β^2; hence any global rational approximation should factor, or extracts, out $\sqrt{\beta}$, thus, writing $\Psi(\beta) = \beta\,\mathrm{G}(\beta)$ with G smooth O(1) on $0 \leq \beta \leq 1$. This is precisely what many successful prior formulations *implicitly* do: they keep the square-root outside the Kernel and approximate only the smooth remainder, either by defining a finite Kernel, always denoted $\mathrm{F}(\eta)$, and placing $\sqrt{\eta}$ in the discharge prefactor, or equivalently by fitting in the variable $x = \sqrt{\eta}$. The present study's small-β analysis makes this necessity explicit, i.e., non-analyticity and the $(\pi/8) \times \sqrt{\beta}$ onset, while the fitted forms, cited in the literature, exemplify the "keep F smooth, O(1) at $\eta \rightarrow 0$" practice. The relevant references on this important matter are Bender et al. (1999), Bleistein and Handelsman

(1986), Olver et al. (2010), and Vatankhah (2010; 2012; 2022), ISO (2017), USBR (2001).

Compact, uniform Padé-type approximation of the kernel $\Psi(\beta)$ on [0, 1]

The exact Euler-Beta representation in Eq. (10) and the small-β expansion in Eqs. (12) and (13) provide a rigorous description of the geometry-flow depth kernel $\Psi(\beta)$ across its entire domain, including the square-root onset $\Psi(\beta) \sim (\pi/8) \times \sqrt{\beta}$ as $\beta \to 0$ and the full-height condition $\Psi(1) = 4/15$. The authors therefore construct a Padé-type rational approximation that is uniformly accurate on the full range [0, 1].

To capture the $\sqrt{\beta}$ singular slope at the origin while remaining simple and highly accurate on the whole interval, one may use the following Padé-type approximation:

$$\Psi(\beta) \approx \sqrt{\beta}\,\frac{p_0 + p_1\beta + p_2\beta^2}{1 + q_1\beta + q_2\beta^2} \tag{14}$$

The ratio of the two quadratic polynomials, whose Maclaurin/Taylor series matches the target function as far as possible, represents the rational approximation known as Padé [2/2] approximant.

As Eq. (10), Eq. (14) was expressly designed to respect the physics at both ends of the admissible range: it enforces the correct small-flow depth asymptotic $\Psi(\beta) \sim (\pi/8) \times \sqrt{\beta}$ as $\beta \to 0$, the $\pi/8$ factor coming from the Euler-Beta value $B(3/2, 3/2)$, and it anchors the full-height limit $\Psi(1) = 4/15$; as a result, the compact Eq. (14) Padé approximate form remains faithful to the governing geometry across the full range $0 \leq \beta \leq 1$. Also, with the chosen coefficients, Eq. (14) minimizes the global error against the exact integral. The maximal deviation caused by the approximate Eq. (14), with the full range $0 \leq \beta \leq 1$, is only 0.04% reached at $\beta = 0.96$. All the deviations caused by Eq. (14) will be calculated and tabulated (Table 1) in one of the next sections.

A numerically optimized set for 4 significant figures is as follows:

$$p_0 = 0.3926\,;\ p_1 = -0.4611\,;\ p_2 = 0.1207\,;\ q_1 = -0.9267\,;\ q_2 = 0.1225$$

Sanity checks:

As $\beta \to 0$, $\Psi(\beta) \sim p_0\sqrt{\beta} \approx 0.3926\sqrt{\beta}$, essentially $\pi/8 \approx 0.392699$

As $\beta = 1$, the exact value of $\Psi(\beta)$ is $\Psi(1) = 4/15 = 0.266666...$, the Padé-type approximation, expressed by Eq. (14), gives 0.266599, i.e., a relative error $\approx$ 0.026%.

Eq. (14) is a compact Padé-type law for the kernel $\Psi(\beta)$, and therefore it applies not only to the elliptic weir, for which $0 \leq \beta \leq 1$, but also to the semi-elliptic case corresponding to $0 \leq \beta \leq 0.50$ and to the circular weir obtained by the specialization $2a = 2b = D$ with $\beta \mapsto \xi = h/D$, where D is the circular weir diameter. All three cases evaluate the same geometry-driven kernel Ψ; only the geometric prefactor in Q_{Th} changes when passing from a general ellipse to the circle. The circular specialization is developed in the next section, where Eqs. (15) to (23) are introduced and analyzed.

Inserting Eq. (14) into Eq. (3) yields the following approximate theoretical stage-discharge relationship, valid for elliptic, semi-elliptic, and circular weirs;

$$Q_{app.,Th} = 4b\sqrt{\beta}\,\frac{p_0 + p_1\beta + p_2\beta^2}{1 + q_1\beta + q_2\beta^2}\sqrt{2g}\,h^{3/2} \tag{3f}$$

where the subscript "*app*" denotes "Approximate". After rearrangement, Eq. (3f) can be written in the following final form:

$$Q_{app.,Th} = 2\sqrt{2}\,\frac{b}{\sqrt{a}}\,\frac{p_0 + p_1\beta + p_2\beta^2}{1 + q_1\beta + q_2\beta^2}\sqrt{2g}\,h^2 \tag{3g}$$

Eq. (3g) is the practice-ready theoretical rating law obtained by inserting the compact Padé kernel [Eq. (14)] into the benchmark discharge relationship [Eq. (3)] and rearranging. It keeps the universal Torricelli scaling outside and packs all geometry–flow depth coupling into a single dimensionless kernel, so the law is both shape-exact via the kernel and scale-exact via the prefactor. In one line, it delivers a differentiable, closed-form evaluator for elliptic, semi-elliptic, and, by specialization, circular weirs.

Moreover, in Eq. (3g), physics are preserved at the endpoints. Indeed, because Eq. (14) is explicitly constrained to: (1) the small-flow depth onset $\Psi(\beta) \sim (\pi/8) \times \sqrt{\beta}$, and (2) the full-height value $\Psi(1) = 4/15$, thus, Eq. (3g) inherits those endpoint behaviors by construction, critical for trustworthy extrapolation near crest and at full height of the opening, i.e., $\beta = 1$. Considering, $\sqrt{(2g)}$, local width $\propto h$, and depth integration $\propto h$, it can be written the following: (1) Near crest: $Q_{app.} \propto h^2$, and (2) At full height: $\Psi(1) = 4/15$ fixes the constant in $Q_{app.,Th}$ at $\beta = 1$.

It is worth noting that Eq. (3g) is valid for: elliptic weirs for which $0 \le \beta \le 1$, semi-elliptic weirs for which $0 \le \beta \le 0.5$, circular weirs corresponding to case obtain by $2a = 2b = D$ and $\beta \mapsto \xi = h/D$ (or keep Eq. (3g) with $a = b = D/2$). This avoids off-range evaluation and clarifies the geometry mapping.

Since Eq. (3g) isolates geometry in the kernel, log-sensitivities split cleanly: the outer h-power dictates the baseline slope while a single dimensionless derivative of the kernel adds the geometry correction. This structure is what enables the neat endpoint exponents reported later (e.g., elasticity dropping from ≈ 2 near crest to ≈1.25 near full height for the elliptic case).

Circular weir - Exact kernel and rating law

In addition, exact Beta-series Eq. (10) and Padé-type approximation Eq. (14) remain valid for the circular weir, of diameter D, obtained by setting $2a = 2b = D$, corresponding to:

$$\beta = h / 2a = h / D = \xi \tag{15}$$

where $0 \le \xi \le 1$.

With this identification, i.e., $\beta \to \xi$, the same dimensionless geometry-flow depth kernel Ψ governs the flow; only the geometric prefactor in the discharge law changes when passing from an ellipse to a circle. Thus Eqs. (10) and (14) specialize verbatim to yield an exact kernel $\Psi(\xi)$ and a compact, uniform Padé-type law for $0 \le \xi \le 1$. The end-point physics are preserved by construction: $\Psi(\xi) \sim (\pi/8) \times \sqrt{\xi}$ as $\xi \to 0$, i.e., incipient submergence, and $\Psi(1) = 4/15$ at full height, which in turn produces the expected full-height scaling $Q_{Th} \propto [\sqrt{(2g)}] \times D^{5/2}$.

In what follows the authors formalize this specialization, deriving Eqs. (15) to (23) for the circular weir and presenting the corresponding exact theoretical rating law alongside its high-accuracy Padé counterpart.

Inserting Eq. (15) into Eq. (10), yields the following exact geometry-driven kernel $\Psi(\xi)$, valid for the circular weir:

$$\Psi(\xi) = \sqrt{\xi} \sum_{n=0}^{\infty} \binom{\frac{1}{2}}{n} (-\xi)^n \mathrm{B}\left(n + \frac{3}{2}, \frac{3}{2}\right) \tag{16}$$

According to Eqs. (3) and (16), and after rearrangement, the exact theoretical discharge relationship for circular weirs can be written as follows:

$$Q_{Th}^{\text{cicular}} = 2\sqrt{2gD}\, h^2 \sum_{n=0}^{\infty} \binom{\frac{1}{2}}{n} (-\xi)^n \mathrm{B}\left(n + \frac{3}{2}, \frac{3}{2}\right) \tag{17}$$

Eq. (17) specializes the general loss-free rating law to the circular geometry by setting $2a = 2b = D$ and $\beta \mapsto \xi = h/D$. It preserves the same dimensionless geometry-flow depth kernel Ψ defined earlier, so the physics and normalization are unchanged, i.e., the Torricelli prefactor carries the hydrodynamic scaling, while $\Psi(\xi)$ encodes the geometry-flow depth interaction. This immediately guarantees the two end-point anchors in the circular setting, namely incipient submergence and the full-height value. In short, Eq. (17) is the exact, loss-free circular rating obtained without any empirical tuning.

The most recognized classical monographs by Chow (1959), Henderson (1966), French (1985), Bos (1989) usually present the integral form of the discharge, or fold it into a discharge coefficient C_d, and then proceed by tabulation or calibration, rather than by deriving a closed, analytic kernel. Recent engineering contributions, notably in the Vatankhah line cited previously, deliver explicit, easy-to-use rating equations by first computing pointwise values of the discharge–flow depth relationship, from experimental datasets or numerical quadrature of the defining integral, and then regressing a short polynomial/rational form to those values. The result is accurate and convenient for practice, but it is still an empirical surrogate for the underlying geometry–flow depth kernel rather than an analytic evaluation of that kernel.

By contrast, Eq. (17) inherits from the prior sections an analytic kernel Ψ, via the Euler–Beta series, that is uniformly valid on $0 \le \xi \le 1$ and physics-exact at both ends; any real-flow effects can be appended multiplicatively via C_d without disturbing the underlying geometry kernel. In practical terms, since the same kernel Ψ governs elliptic, semi-elliptic, and circular openings, Eq. (17) establishes a unified baseline for circular weirs: it is differentiable in closed form useful for sensitivity, and, via the paper's Padé-type surrogate, admits a compact, uniformly accurate formula with a maximum relative error of 0.04%, i.e., sub-0.05%, (Table 1), far smaller than typical uncertainties in C_d or field measurements. Thus, Eq. (17) is the reference theoretical law to which fitted or coefficient-based relationships should be compared.

In addition, Eq. (17) can be rewritten in the following reduced form:

$$Q_{Th}^{\text{cicular}} = 2\sqrt{2gD}\,h^2\,\mathrm{P}(\xi) \tag{18}$$

where

$$\mathrm{P}(\xi) = \frac{\Psi(\xi)}{\sqrt{\xi}} \tag{19}$$

Thus, according to Eq. (16), one may write the following:

$$\mathrm{P}(\xi) = \sum_{n=0}^{\infty} \binom{\frac{1}{2}}{n} (-\xi)^n \,\mathrm{B}\left(n+\frac{3}{2}, \frac{3}{2}\right) \tag{20}$$

$\mathrm{P}(\xi)$ could be called the dimensionless discharge kernel for the circular weir, or simply the circular kernel.

Eq. (20) defines the dimensionless discharge kernel $\mathrm{P}(\xi)$ for the circular weir, often called simply "the circular Kernel". It is the circular analogue of the elliptic kernel Ψ after the specialization $2a = 2b =$ and $\beta \mapsto \xi = h/D$. In this normalization, all geometry-flow depth coupling for the circular opening is absorbed into a single dimensionless function (the "circular kernel"), while the universal hydrodynamic scaling remains in the Torricelli prefactor. Put differently, Eq. (20) isolates geometry from physics, exactly as Eqs. (3) and (4) do in the elliptic case, so that the discharge law can be written in a reduced and portable form. Because Eq. (20) inherits the same kernel structure as the elliptic formulation, it enforces the two anchors by construction: near the crest ($\xi \to 0$), the kernel exhibits the Torricelli-driven square-root onset $\propto\sqrt{\xi}$, and at full height ($\xi = 1$) it attains the exact value 4/15. These constraints are not added empirically; they flow from the exact formulation, via Eqs. (16) to (19)) and guarantee consistency with the circular full-height scaling $Q_{Th} \propto \sqrt{(2g)}\, D^{5/2}$. Eq. (20) is not a fit; it is the exact circular kernel implied by the general theory. As a result, any subsequent approximation, e.g., the compact Padé-type law introduced next, is measured against a physics-exact reference. This separation lets the user appends a discharge coefficient C_d for real-flow effects multiplicatively, without contaminating the geometry kernel, simplifying calibration and uncertainty analysis. With Eq. (20) in hand, the circular rating law inherits all the smoothness and differentiability properties of the kernel, via the Euler-Beta representation from the elliptic framework. That enables reliable sensitivities ($\partial Q/\partial h$), curvature ($\partial^2 Q/\partial h^2$) for sensitivity study. Where much of the literature either keeps the circular factor implicit, folded into C_d or replaces it with a fitted surrogate, Eq. (20) provides the explicit analytic kernel for the circle, closing the loop from geometry to rating without empirical tuning.

For $\beta = \xi$, and according to Eqs. (14) and (19), the Padé-type approximation for circular weirs can be written as follows:

$$\mathrm{P}(\xi) = \frac{p_0 + p_1\xi + p_2\xi^2}{1 + q_1\xi + q_2\xi^2} \tag{21}$$

The deviations between the exact Eq. (20) and the approximate Eq. (21) are the same than those affected Ψ ($\beta = \xi$) reported in Table 1 below. Accordingly, Eq. (21) provides a compact Padé-type surrogate of the exact circular kernel defined in Eq. (20). The endpoint behavior's, $\Psi(\xi) \sim (\pi/8) \times \sqrt{\xi}$ as $\xi \to 0$ and $\Psi(1) = 4/15$, originate from Eq. (20) and are imposed on Eq. (21) as matching constraints, yielding a uniformly accurate yet simple rating formula.

As can be seen in Table 1, the Padé-type approximate form delivers a maximum relative error of 0.04%, i.e., sub-0.05%, across the full range $0 \le \beta \le 1$ and $0 \le \xi \le 1$; the documented worst case is about 0.04% reached at $\beta = \xi = 0.96$, and the relative error at $\beta = \xi = 1$ is ~0.026%, far below typical discharge-measurement and C_d uncertainties. In short, it is "exact enough" for engineering while remaining closed-form. Thus, the Padé-type approximate formula, given by Eq. (21), is then a near-exact (0.04% maximum deviation) representation of this exact kernel for convenient, uniform use on $0 \le \xi \le 1$.

Thus, for $\beta = \xi$, and $2b = D$, considering Eqs. (3), (19) and (21), and after rearrangement, the following is an excellent approximate theoretical discharge relationship for the circular weirs, while remembering that the subscript "*App.*" denotes "Approximate".

$$Q_{app.,Th}^{\text{cicular}} = 2\left(\frac{p_0 + p_1\xi + p_2\xi^2}{1 + q_1\xi + q_2\xi^2}\right)\sqrt{2gD}\,h^2 \tag{22}$$

In Eq. (22), the term $\sqrt{(2gD)}$ is the reference velocity scale induced by using D as the reference length in the nondimensionalization ($\xi = h/D$). It does not assume $h = D$; the actual flow depth enters only through the dimensionless kernel $\mathrm{P}(\xi)$. Also, it is not the local slice velocity $\sqrt{(2g(h - z)}$; it is just like Torricelli's $\sqrt{(2gh)}$, but with the reference length D. Herein, nondimensionalization means replacing dimensional variables by unit-free ratios built from a characteristic scale. The flow depth h, which is a length, is scaled by the diameter D, which also a length. Grouping the discharge as follows, makes the physics transparent: area × velocity gives the baseline flow-rate scale, while the kernel $\mathrm{P}(\xi)$, with $\xi = h/D$, accounts for how the actual flow depth h fills the opening:

$$Q_{app.,Th}^{\text{cicular}} \sim \underset{\text{area scale}}{D^2} \times \underbrace{\sqrt{2gD}}_{\text{velocity scale}} \times \underset{\text{dimensionmess kernel}}{\mathrm{P}(\xi)} \tag{22a}$$

Thus, √(2*gD*) plays the role of a reference exit velocity, while D^2 supplies the geometric area scale; together they yield the classical √(2*g*) × $D^{5/2}$ scaling, which is exactly the capacity scaling reached at full wetting, where P(1) = 4/15. The kernel P(ξ) modulates this scale according to the actual relative flow depth $\xi = h/D$.

Eq. (22) is the paper's "engineering workhorse" for circular sharp-crested weirs, a near-exact, closed-form rating law which can be dropped straight into calculation routine. It's built by substituting the uniformly accurate Padé kernel into the loss-free circular formulation, so one may keep exact physics, i.e., Torricelli scaling, correct end-point anchors, while gaining a single compact evaluator. Eq. (22) is a short rational form means cheap, stable evaluation and smooth derivatives dQ/dh, d^2Q/dh^2 for sensitivity. It exhibits the same kernel architecture as the elliptic case; only the geometry scale changes. There is only one framework for elliptic, semi-elliptic, and circular openings. Eq. (22) is a rare combination, theory-near-exact structure with computationally light and real-time friendly. Moreover, it should be treated as the baseline circular rating; appending C_d for reality, and the users have a robust, high-fidelity law for the full usable flow depth range.

When the circular opening is fully wetted, the geometry reaches its natural end state and the discharge law locks to a single, universal constant set by the circle itself. This condition serves as the definitive anchor for the entire development: it removes ambiguity, collapses scaling cleanly to diameter and gravity, and yields a benchmark that any laboratory rig or field installation can reproduce. In practice, this end point is invaluable. It provides a one-point calibration check for instruments, sets the absolute capacity ceiling for a given diameter, and offers a simple pass/fail target for simulations and controller implementations. During commissioning and routine diagnostics, approaching full wetting cleanly separates geometric effects from hydraulic losses and instrumentation drift, allowing engineers to isolate the discharge coefficient and troubleshoot with confidence. In short, the fully wetted circular case is the model's keystone and the practitioner's most reliable reference state.

For the configuration in which the circular opening is fully wetted, corresponding to ξ = 1, the exact kernel reaches the endpoint value Ψ(1) = 4/15, which, by Eq. (19), implies P(1) = 4/15. Inserting this result into Eq. (18) and simplifying leads to the following exact theoretical discharge relationship governing the fully wetted circular case:

$$Q_{Th}^{\text{full cicular}} = \frac{8}{15}\sqrt{2gD^5} \tag{23}$$

The scaling $Q_{Th} \propto \sqrt{2gD^5}$ is the only one compatible with a gravity-driven, loss-free orifice whose wetted height equals its diameter; the √(2*g*) term is the Torricelli (gravity-driven) velocity scale; the factor $D^{5/2}$ comes from multiplying the circular length scale D by the flow depth law $h^{3/2}$, which at full height $h = D$ gives $D \times D^{3/2} = D^{5/2}$.

Eq. (23) yields the capacity diameter for full height under loss-free conditions, under the following form:

$$D = \left[\frac{15}{8\sqrt{2g}} Q_{Th} \right]^{2/5} \tag{23a}$$

Eq. (23a) can be rewritten in the following reduced form, where the discharge Q in (m^3/s) and the diameter D in (m):

$$D \sim 0.709\, Q_{Th}^{2/5} \tag{23b}$$

For operational ratings, Eq. (23a) can be used in the following form:

$$D = \left[\frac{15}{8\sqrt{2g}\, C_d} Q \right]^{2/5} \tag{23c}$$

where C_d is the discharge coefficient. This formula is a capacity anchor, loss-free and full height; in practice, the site-calibrated $C_d < 1$ should be applied.

The scaling $Q \propto D^{5/2}$ at full height is classical; it follows from integrating Torricelli velocity against the circular width. The inverted form $D \propto Q^{2/5}$ is a direct corollary, and is sometimes used implicitly in design charts or quick checks. However, many texts present the forward relation and/or fold geometry into empirical coefficients; they do not always print the inverted capacity law explicitly. Including the compact inverted law, i.e., Eq. (23b), is justified and helpful. However, the users must: (1) explicitly link it to Eq. (23), (2) note the full-height, loss-free regime, and (3) accompany it with the operational version with C_d. In short, the users can consider the following practical variant of Eq. (23b):

$$D \sim 0.709 \left(\frac{Q}{C_d} \right)^{2/5} \tag{23d}$$

C_d maps reality to theory. The theory cleanly separates geometry and flow depth through the kernel; all non-ideal hydraulic effects are then appended multiplicatively as C_d, preserving the correct ordering between the theoretical upper bound and the actual discharge. In other words, the following can be written:

$$C_d \equiv \frac{Q_{\text{measured}}}{Q_{Th}(h, D, g)} \tag{23e}$$

Meanwhile, C_d still accounts for installation-specific losses, non-ideal hydraulic effects, i.e., vena-contracta/edge sharpness and thickness, approach-flow nonuniformity and Froude effects, viscous/scale influences, surface tension at small flow depths, and possible downstream influence, i.e., approach flow conditions, appended multiplicatively to the loss-free circular law. That's exactly how the authors position the operational rating: $Q = C_d \times Q_{Th}$.

Exact Euler-Beta kernel vs. Padé surrogate - Full-range accuracy and engineering relevance

This section benchmarks the compact Padé approximation, expressed by Eq. (14), against the exact Euler-Beta representation of the kernel, Eq. (10), across the entire admissible depth range. Using high-precision evaluations of the exact series as reference and a numerically optimized Padé form with four-significant-figure coefficients, we quantify pointwise deviations and verify that the surrogate preserves the governing physics at both ends (incipient-submergence onset and full-height anchor). The tabulated results show a sub-0.05% maximum relative error (~0.04%), with the worst near the upper end of the range, with a still smaller deviation at full submergence, levels far below typical uncertainties associated with discharge coefficients and field instrumentation. In practice, this means the Padé law provides the accuracy of a reference model with the computational economy needed for design charts, calibration workflows, and real-time controllers, while remaining transparent and easy to differentiate for sensitivity.

Table 1 demonstrates that the Padé-type surrogate reproduces the exact Euler-Beta kernel with uniform, extremely small error over the entire admissible range $0 \leq \beta \leq 1$. The largest relative deviation is 0.04%, occurring near $\beta = 0.96$; at full height $\beta = 1$, the deviation drops to ~0.0255%. These numbers are fully consistent with the error curve shown in the accompanying Fig. 2 and confirm the surrogate's tight tracking of the reference values. This is attributable to the use of four-significant-figure coefficients in the Padé form: the analytic construction enforces the full-height anchor, but rounding the coefficients introduces a minute, practically irrelevant offset.

A ≤ 0.04% kernel mismatch is orders of magnitude smaller than uncertainties from discharge coefficients and field instrumentation, so the Padé surrogate will not be the limiting factor in engineering accuracy. It offers the convenience of a short, closed-form evaluator with performance indistinguishable from the exact series for design, calibration, and real-time use.

In addition, Table 2 is valid for elliptic, semi-elliptic, and circular weirs. The reason is structural: both the exact kernel and the Padé surrogate being compared in Table 1 are shape-unified objects. Eq. (10) gives an exact Euler–Beta series for the same geometry-flow depth kernel Ψ across the family, elliptic, semi-elliptic, and circular, with only the admissible range of the relative flow depth changing; the circular case is the specialization $2a = 2b = D$ with $\beta \mapsto \xi = h/D$. Eq. (14) is a compact Padé surrogate for that very kernel and was designed to respect the endpoint physics on the full range; it therefore inherits the same cross-geometry validity.

It can be observed from Table 1 and Fig. 2, a uniform smallness and upper bound in the semi-elliptic range. Therefore, on the semi-elliptic sub-range $0 \leq \beta = \xi \leq 0.50$, deviations are strictly smaller than the global worst case. Concretely, Table entries give $\delta(0.48)$ =

0.0071991% and $\delta(0.50)$ = 0.0083703%, i.e., well below 0.01% at the semi-elliptic ceiling. Across $0 \leq \beta = \xi \leq 0.50$, all listed deviations remain under 0.009%, as it can also be seen in Fig. 2. Finally, regarding the semi-elliptic weir, the deviations reported in Table 1 are negligible compared with typical rating-curves uncertainties.

Table 1: Deviation between Padé-Type approximation [Eq. (14)] and exact Beta-Series [Eq. (10)]

$\beta = h/(2a)$	**Exact $\Psi(\beta)$ Eq. (10)**	**Approximate $\Psi(\beta)$ Eq. (14)**	**Deviation (%)**
0	0	0	0
0.04	0.0777494	0.0777361	0.0170935
0.08	0.1088220	0.1088105	0.0105626
0.12	0.1318740	0.1318666	0.0055844
0.16	0.1506298	0.1506269	0.0018835
0.20	0.1665437	0.1665444	0.0004485
0.24	0.1803655	0.1803685	0.0016721
0.28	0.1925426	0.1925460	0.0017661
0.32	0.2033663	0.2033684	0.0010315
0.36	0.2130387	0.2130378	0.0004153
0.40	0.2217059	0.2217005	0.0024104
0.44	0.2294767	0.2294658	0.0047307
0.48	0.2364340	0.2364170	0.0071991
0.50	0.2395377	0.2395176	0.0083703
0.52	0.2426414	0.2426183	0.0095174
0.56	0.2481483	0.2481197	0.0115181
0.60	0.2529926	0.2529595	0.0130513
0.64	0.2572025	0.2571666	0.0139501
0.68	0.2607979	0.2607610	0.0141469
0.72	0.2637910	0.2637548	0.0137292
0.76	0.2661865	0.2661516	0.0130888
0.80	0.2679804	0.2679460	0.0128314
0.84	0.2691589	0.2691209	0.0141196
0.88	0.2696944	0.2696444	0.0185241
0.92	0.2695383	0.2694637	0.0276762
0.96	0.2686012	0.2684938	0.0399672
1.00	0.2666666	0.2665985	0.0255112
			Max. 0.0399672%

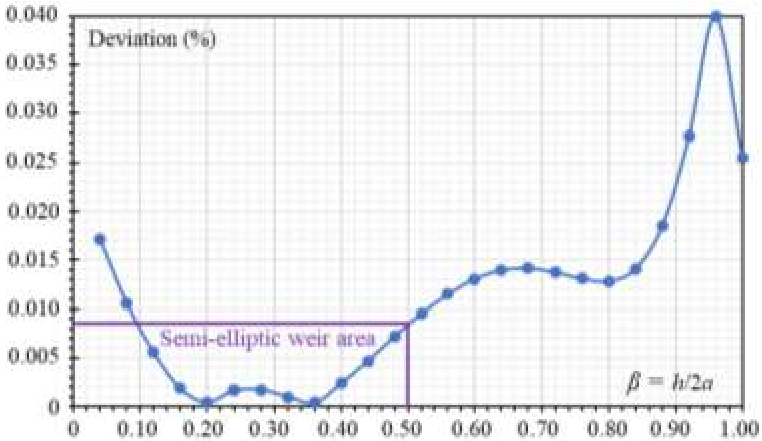

Figure 2: Deviation (%) between exact kernel Eq. (10) and the approximate Padé Eq. (14), according to Table 1

SENSITIVITY ANALYSIS

Definitions

For any quantity *x*, the absolute sensitivity of discharge to *x* is expressed as follows:

$$S_x = \frac{\partial Q}{\partial x} \tag{24}$$

S_x is the absolute sensitivity of discharge Q to the variable x. It tells how much Q changes for a small absolute change in x, for instance change in Q in m^3/s per mm of flow depth. Typical examples are the following:

$S_h = \frac{\partial Q}{\partial h}$ = Sensitivity to flow depth h

$S_D = \frac{\partial Q}{\partial D}$ or S_a , S_b = Sensitivity to geometry

$S_g = \frac{\partial Q}{\partial g}$ = Sensitivity to gravity

For operational ratings, $S_{C_d} = \frac{\partial Q}{\partial C_d}$ = Theoretical discharge Q

The elasticity, or the relative sensitivity, or the log-slope of the rating, is defined as follows:

$$E_x \equiv \frac{\partial \ln Q}{\partial \ln x} = \frac{x}{Q}\frac{\partial Q}{\partial x} = \frac{x}{Q} S_x \tag{25}$$

which quantifies the percent change in Q caused by a percent change in x. In rating-curve terms, E_h is the local exponent of the Q–h law.

Elliptic and semi-elliptic weirs

Sensitivity to flow depth h

Eq. (3b) is the cleanest way to see the parameter dependence, because it rewrites the loss-free rating as a product of a pure scale factor and a dimensionless kernel as follows:

$$Q_{Th} = 2\sqrt{2}\sqrt{2g}\,\underbrace{\left(\frac{b}{\sqrt{a}}\right)}_{\text{scale}} h^2 \underbrace{\Psi(\beta)}_{\text{dimensionless Kernel}} \tag{26}$$

Remember that $\beta = h/(2a) \in [0, 1]$, or $\in [0, 0.5]$ for semi-elliptic weir. With the help of Eq. (10), Eq. (26) can be rewritten in the following reduced form:

$$Q_{Th}(h,a,b,g) = \sqrt{2g}\,\underbrace{\left(\frac{b}{\sqrt{a}}\right)}_{\text{scale}} h^2 \underbrace{\Phi(\beta)}_{\text{dimensionless Kernel}} \tag{27}$$

where

$$\Phi(\beta) = 2\sqrt{2}\,\frac{\Psi(\beta)}{\sqrt{\beta}} \tag{28}$$

where the $\Phi(\beta)$ is the dimensionless geometry-flow depth kernel which absorbs the constant $2\sqrt{2}$, and any internal normalizations. This keeps the scale $b/\sqrt{a}$ cleanly separated from the shape–flow depth coupling, all in Φ.

Differentiate Eq. (27) with respect to h, while noting that $\partial\beta/\partial h = 1/(2a)$, the following can be written:

$$S_h = \frac{\partial Q}{\partial h} = \sqrt{2g}\,\frac{b}{\sqrt{a}}\left[2h\,\Phi(\beta) + \frac{h^2}{2a}\Phi'(\beta)\right] \tag{29}$$

E_h as defined by Eq. (29) is the logarithmic slope, or the log-slope of the rating, so any constant prefactor, such as $4b \times \sqrt{(2g)}$, as it can be seen in Eq. (3), cancels out. What matters is the h^2 term and the kernel $\Phi(\beta)$. Thus, with Eq. (29), and after differentiating $Q_{Th}(h)$ with respect to h, the flow depth elasticity can be expressed as follows:

The corresponding elasticity, i.e., log-slope of the rating, is obtained by combining Eqs. (25) and (29). It reads as, follows:

$$E_h = \frac{\partial \ln Q_{Th}}{\partial \ln h} = 2 + \beta \frac{\Phi^{'}(\beta)}{\Phi(\beta)} \tag{30}$$

Proceeding to the checks at the endpoints from Kernel's physics, yields the following:

As $\beta \to 0$, i.e., incipient submergence, $\Phi(\beta)$ tends to a constant determined by the exact kernel, hence $\beta\,\Phi'/\Phi \to 0$. Thus, Eq. (30) reduces to the following:

$$E_h = 2 \tag{31}$$

This can be written in the following symbolic form:

$$E_h \underset{\beta \to 0}{\to} 2 \tag{32}$$

This result indicates that, very near the crest, a 1% error in h produces ~2% error in Q. From the geometric intuition, near the crest, the local opening width of an ellipse grows like $\sqrt{h}$. Multiplying that by the Torricelli velocity scale $\propto\sqrt{h}$ and the usual depth integration $\propto h$ gives $Q \propto h^2$, whose log-slope is 2.

At full height $\beta = 1$, according to Eq. (30), one may write what follows:

$$E_h = 2 + \frac{\Phi^{'}(1)}{\Phi(1)} \tag{33}$$

Exact calculations show what follows: $\Psi(1) = 4/15$, and $\Psi'(1) = -1/15$. One can proceed to a numerical check against table 1. Using the exact values in Table 1, $\Psi(0.96) = 0.2686012$ and $\Psi(1) = 0.2666666$, the backward secant slope over [0.96, 1] is a follow: $(0.2686012 - 0.2666666)/0.04 = 0.048365$, which trends toward the analytic limit $-1/15 \approx -0.0667$ as $\beta \to 1^-$.

Differentiating $\Phi(\beta)$ using Eq. (28), yields the following:

$$\Phi^{'}(\beta) = 2\sqrt{2}\left[\Psi^{'}(\beta)\beta^{-1/2} - \frac{1}{2}\Psi(\beta)\beta^{-3/2}\right] \tag{34}$$

Thus, Eq. (34) leads to the following:

$$\Phi^{'}(1) = 2\sqrt{2}\left[\Psi^{'}(1)\beta^{-1/2} - \frac{1}{2}\Psi(1)\times 1^{-3/2}\right] \tag{35}$$

Or

$$\Phi'(1) = 2\sqrt{2}\left(-\frac{1}{15} - \frac{1}{2} \times \frac{4}{15}\right) = -\frac{2\sqrt{2}}{5} \tag{36}$$

Thus, according to Eq. (28), the following can be written:

$$\Phi(1) = 2\sqrt{2}\,\frac{\Psi(1)}{\sqrt{1}} = 2 \times \sqrt{2} \times \frac{4}{15} = \frac{8\sqrt{2}}{15} \tag{37}$$

Thus, Eq. (33) gives the final result as follows:

$$E_h = 2 - \frac{2 \times \sqrt{2} \times 15}{5 \times 8 \times \sqrt{2}} = 2 - \frac{3}{4} = \frac{5}{4} \tag{38}$$

This result can be written in the following symbolic form:

$$E_h \underset{\beta \to 1}{\longrightarrow} 5/4 \tag{39}$$

Thus, the following meanings can be deduced: (1) Near full wetting, i.e., at the top of the range, the theoretical rating behaves locally like a power law $Q \propto h^{1.25}$; (2) A 1% change in flow depth produces about a 1.25% change in theoretical discharge at this endpoint; (3) The elasticity drops from 2 near the crest (very sensitive) to 1.25 at full height (less sensitive). Thus, errors in h matter l**ess** as we approach full wetting than they do near onset.

In other words, these limits succinctly capture the decreasing flow depth-sensitivity as the opening becomes fully wetted: the rating is most sensitive to flow depths near the crest, less so near full height.

For any β value, the corresponding exact elasticity E_h can be computed using Eq. (30). For instance, when considering $\beta = 0.50$, the following can be written. From Eq. (10), confirmed by Table 1, one may write:

$$\Psi(0.50) = 0.2395377$$

And, according to Eq. (28), the following is derived:

$$\Phi(0.50) = 2 \times \sqrt{2} \times \frac{\Psi(0.50)}{\sqrt{0.50}} = 2 \times \sqrt{2} \times \frac{0.2395377}{\sqrt{0.50}} = 0.9581508$$

From Eq. (28), the following can be derived:

$$\Phi'(\beta) = 2\sqrt{2}\left[\beta^{-1/2}\Psi'(\beta) - \frac{1}{2}\beta^{-3/2}\Psi(\beta)\right] \tag{28a}$$

On the other side, using Eq. (10), i.e., the exact series for Ψ, the exact derivative at β = 0.50 is as follows, valid for elliptic and semi-elliptic weirs:

$$\Psi'(0.50) = 0.155185$$

On the basis of the foregoing numerical results, Eq. (28a) produces the following:

$$\Phi'(0.50) = 2 \times \sqrt{2} \times \left[0.50^{-1/2} \times 0.155185 - \frac{1}{2} \times 0.50^{-3/2} \times 0.2395377 \right]$$

Calculations give the following:

$$\Phi'(0.50) = -0.3374108$$

Final, using Eq. (30), the elasticity sought is obtained as follows:

$$E_h = 2 + 0.50 \times \frac{-0.3374108}{0.9581508}$$

That is

$$E_h = 1.8239205 \approx 1.824$$

Equivalently, since $\Phi \propto \beta^{-1/2} \times \Psi$, according to Eq. (28), the following can be written:

$$\underset{\beta \to 0.50}{E_h} = 2 - \frac{1}{2} + 0.50 \times \frac{\Psi'(0.50)}{\Psi(0.50)} = \frac{3}{2} + 0.50 \times \frac{0.155185}{0.2395377}$$

That is

$$\underset{\beta \to 0.50}{E_h} = 1.8239205 \approx 1.824$$

This coincides with the previously derived result.

Another method can be used to compute $\Psi'(0.50)$. This is based on the centered secant, or the central difference slope. To approximate a derivative at a point β_0, a centered secant uses two values symmetrically placed about β_0:

$$\Psi' = \frac{\Psi(\beta_0 + \delta) - \Psi(\beta_0 - \delta)}{2\delta}$$

It's "centered" because the two-evaluation points straddle β_0. For elliptic weirs the admissible range is $0 \le \beta \le 1$, so, $\beta_0 = 0.50$ is an interior point. That lets us use a symmetric pair, e.g., 0.48 and 0.52 around 0.50, which gives a more accurate (second-order) estimate than a one-sided difference. In addition, in the calculation, one may take $\delta = 0.02$ because

Table 1 provides exact-series values at β = 0.48, 0.50, 0.52. Hence, one may write what follows:

$$2\delta = 2\times 0.02 = 0.04$$

which is also simply the spacing between the two following symmetric points:

$$0.52 - 0.48 = 0.04$$

Thus, the following can be written:

$$\Psi'(0.50) = \frac{\Psi(0.50+0.02)-\Psi(0.50-0.02)}{2\times 0.02}$$

That is

$$\Psi'(0.50) = \frac{\Psi(0.52)-\Psi(0.48)}{0.04}$$

Table 1 provides the exact following values: $\Psi(0.52)$ = 0.2426414, and $\Psi(0.48)$ = 0.2364340. Thus, one may derive the following final result:

$$\Psi'(0.50) = \frac{0.2426414-0.2364340}{0.04} = 0.155185$$

Accordingly, this reproduces the previous result.

The previous final result $E_h \approx 1.824$ means that 1% relative error in h produces ≈ 1.824% relative error in the discharge Q. It is worth noting that E_h is the local "power-law exponent" of the stage–discharge curve. At $\beta = \xi = 0.50$, the value $E_h \approx 1.824$ means that a relative error in flow depth is magnified by a factor of ≈1.824 in the discharge. Thus, the following can be written:

$$\frac{\Delta Q}{Q} \approx 1.824\frac{\Delta h}{h}$$

For example, a 0.5% relative error in flow depth h yields ≈ 0.91% discharge relative error.

This mid-depth sensitivity sits below the near-crest limit, where $E_h \rightarrow 2$, as indicated in Eq. (32), for elliptic/semi-elliptic weirs, and above the upper-range values as the opening approaches full height, as indicated in Eq. (39). Physically, the square-root kernel flattens with depth, so the Q–h curve becomes progressively less steep, and E_h decreases from its onset value toward its upper-range limit.

The computed $E_h < 2$ reflects a negative kernel slope at β = 0.50, i.e., $\Phi'(0.50) < 0$: incremental increases in flow depth add proportionally less new effective width than at small flow depths, so Q grows a bit more slowly than h^2.

Users can use E_h as the magnification factor to size gauge precision and to propagate reading errors. If a project tolerates the following:

$$\frac{|\Delta Q|}{Q} \leq 1\%$$

around $\beta \approx 0.5$, then the allowable flow depth relative error is as follows:

$$\frac{|\Delta h|}{h} <\approx \frac{100 \times 0.01}{1.824} = 0.54824561 \approx 0.55\%$$

From a robustness point view, multiplicative factors like a discharge coefficient C_d do not affect E_h as they cancel in $\partial \ln Q$; the value 1.824 therefore characterizes the intrinsic shape of the theoretical rating at mid-depth.

From reproducibility point view, because the kernel is evaluated in closed form, or with a uniformly tight Padé surrogate, the numerical value is stable and repeatable to the reported precision.

Sensitivity to geometry b (horizontal semi-axis)

By construction, Φ depends solely on β, and hence on h and a, not on b. So, b appears only in the linear prefactor $b/\sqrt{a}$, according to Eq. (26).

Holding h, a, g, fixed, one may write the following:

$$\frac{\partial Q_{Th}}{\partial b} = \sqrt{2g}\,\frac{1}{\sqrt{a}}\,h^2\Phi(\beta) \tag{40}$$

On the other hand, by definition as expressed by Eq. (25), the following can be written:

$$E_b = \frac{\partial \ln Q_{Th}}{\partial \ln b} = \frac{b}{Q_{Th}}\frac{\partial Q_{Th}}{\partial b} \tag{41}$$

Substituting Eq. (27) and the derivative expressed by Eq. (40), Eq. (41) yields the following:

$$E_b = \frac{b}{Q_{Th}\sqrt{2g}\left(b/\sqrt{a}\right)h^2\Phi(\beta)}\left[\sqrt{2g}\left(1/\sqrt{a}\right)h^2\Phi(\beta)\right] = 1 \tag{42}$$

Thus

$$E_b = 1 \tag{43}$$

Therefore a 1% change in b produces a 1% change in Q. For operational discharge $Q = C_d \times Q_{Th}$: if C_d is independent of b, then E_b remains 1. If C_d depends on b in a particular installation, add $\partial \ln C_d / \partial \ln b$ to get the total operational elasticity.

Sensitivity to geometry a (vertical semi-axis)

Since $\beta = h/(2a)$, thus $\partial\beta/\partial a = -\beta/a$, and there is also $a^{-1/2}$ in the discharge law expressed by Eq. (27). Therefore, from Eq. (24), the following can be written:

$$S_a = \frac{\partial Q_{Th}}{\partial a} \tag{24a}$$

Takin into account Eq. (27), Eq. (24a) leads to the following:

$$S_a = \sqrt{2g}\,\frac{b}{\sqrt{a}}h^2\left[-\frac{1}{2a}\Phi(\beta) - \frac{\beta}{a}\Phi'(\beta)\right] \tag{44}$$

Therefore, one may derive the following:

$$E_a = \frac{\partial \ln Q_{Th}}{\partial \ln a} = -\frac{1}{2} - \beta\frac{\Phi'(\beta)}{\Phi(\beta)} \tag{45}$$

Proceeding to the checks at the endpoints from Kernel's physics, yields the following:

Previously, we have stated that as $\beta \to 0$, i.e., incipient submergence, $\Phi(\beta)$ tends to a constant determined by the exact kernel, hence $\beta\,\Phi'/\Phi \to 0$. Thus, Eq. (45) reduced to the following:

$$E_a = -\frac{1}{2} \tag{46}$$

This result can be written symbolically as follows:

$$\underset{\beta \to 0}{E_a} = -\frac{1}{2} \tag{46a}$$

At full height $\beta = 1$, according to Eqs. (36) and (37), Eq. (45) can be written as follow:

$$E_a = -\frac{1}{2} + \frac{2\times\sqrt{2}\times 15}{5\times 8\times\sqrt{2}} = -\frac{1}{2} + \frac{3}{4} = \frac{1}{4} \tag{47}$$

Thus

$$E_a = \frac{1}{4} \tag{48}$$

which can be written in the following symbolic form:

$$\underset{\beta \to 1}{E_a} = \frac{1}{4} \tag{48a}$$

The sign flip reflects the competing effects of a. As a increases (with h fixed), two things happen. First, the scale factor $b/\sqrt{a}$ decreases, which pushes Q_{Th} down. Second, $\beta = h/(2a)$ becomes smaller, so a larger portion of the ellipse is effectively open and the kernel $\Phi(\beta)$ increases, which pushes Q_{Th} up. Near full wetting, this second effect is stronger, so the net influence of a is slightly positive.

At $\beta \to 1$, It is worth noting the following:

$$E_h + E_a = \frac{3}{2} \tag{49}$$

This "sum rule" is an excellent sanity check for the user.

As a practical read-out, one may write the following: (1) Uncertainty in b maps 1:1 into Q_{Th} ($E_b = 1$); (2) Uncertainty in a has flow depth-dependent influence: it reduces Q_{Th} near onset (elasticity −0.5) but slightly increases it near full height (elasticity +0.25).

Sensitivity to gravity

According to the discharge law expressed by Eq. (27), gravity appears only as $\sqrt{(2g)}$. Thus, the following can be written:

$$S_g = \frac{\partial Q_{Th}}{\partial g} = \frac{1}{\sqrt{2g}} \frac{b}{\sqrt{a}} h^2 \Phi(\beta) \tag{50}$$

Therefore, according to Eq. (25), on may deduce the following:

$$E_g = \frac{g}{Q_{Th}} S_g = \frac{g}{Q_{Th}} \frac{1}{\sqrt{2g}} \frac{b}{\sqrt{a}} h^2 \Phi(\beta) \tag{51}$$

Replacing Q_{Th} by the discharge law expressed by Eq. (27), Eq. (51) reduces to the following:

$$E_g = \frac{g}{Q_{Th}} S_g = \frac{g}{\sqrt{2g}\, \frac{b}{\sqrt{a}} h^2 \Phi(\beta)} \frac{1}{\sqrt{2g}} \frac{b}{\sqrt{a}} h^2 \Phi(\beta) \tag{52}$$

After easy simplification, Eq. (52) gives the following:

$$E_g = \frac{1}{2} \tag{53}$$

This result means that discharge scales with the square root of gravity. Thus, a 1% change in g produces a 0.5% change in the theoretical discharge Q_{Th}, provided all else fixed. A 0.5% change in g causes 0.25% change in the theoretical discharge.

Gravity varies only slightly with latitude and elevation, thus, its effect on Q_{Th} is small. For operational discharge $Q = C_d \times Q_{Th}$, Eg stays 1/2 provided C_d does not depend on g. If it did, add $\partial \ln C_d / \partial \ln g$.

In field metering at the Earth's surface, g is effectively constant; this term matters mainly in laboratory calibration or metrology traceability discussions; high-accuracy calibration work where every quantity is tied back to SI units through an unbroken chain of standards (what labs call *traceability*). In those contexts, people explicitly account for local g because it appears in the physics, e.g., $\sqrt{g}$ in the theoretical law, such as $p = \rho g h$ for pressure sensors, or gravimetric weigh tanks where weight depends on g. Even though variation in g is tiny on Earth, traceable calibrations and inter-laboratory comparisons sometimes include it in the uncertainty analysis.

Circular weirs

Consider the theoretical discharge law, for circular weirs, expressed by Eq. (18) which we recall as follows:

$$Q_{Th}^{\text{cicular}} = 2\sqrt{2g}\, D^{1/2}\, h^2\, \mathrm{P}(\xi) \tag{18}$$

The circular Kernel $\mathrm{P}(\xi)$ exact formulation is given by Eq. (20), with $\xi = h/D$. As in the elliptic case, the circular kernel enforces the endpoint physics, as it was indicated in one of the previous sections. Herein the Torricelli scaling sits in $\sqrt{(2g)}$, the geometry scale is $\sqrt{D}$, and all coupling with flow depth appears through the dimensionless kernel $\mathrm{P}(\xi)$.

Sensitivity to flow depth h

According to the definition of S_h, the following can be written:

$$S_h = \frac{\partial Q}{\partial h} = 2\sqrt{2g}\left[2h\,\mathrm{P}(\xi) + \frac{h^2}{D}\mathrm{P}'(\xi)\right] \tag{54}$$

According to the definition expressed by Eqs. (25) and with the help of Eq. (18), one may write the following:

$$E_h = \frac{h}{Q_{Th}} S_h = \frac{h}{2\sqrt{2g}\, D^{1/2} h^2 \mathrm{P}(\xi)} 2\sqrt{2g} \left[2h\mathrm{P}(\xi) + \frac{h^2}{D} \mathrm{P}'(\xi) \right] \tag{55}$$

After easy simplification, Eq. (55) reduces to the following:

$$E_h = 2 + \xi \frac{\mathrm{P}'(\xi)}{\mathrm{P}(\xi)} \tag{56}$$

Near the crest, i.e., $\xi \to 0$, Eq. (20) gives the following:

$$\mathrm{P}(\xi) \sim \frac{\pi}{8}\sqrt{\xi} \text{ , and } \mathrm{P}'(\xi) \sim \frac{\pi}{16}\xi^{-1/2}$$

Therefore, the following can be written:

$$\lim_{\xi \to 0} \left[\xi \frac{\mathrm{P}'(\xi)}{\mathrm{P}(\xi)} \right] = \frac{1}{2} \tag{56a}$$

Thus, inserting Eq. (56a) into Eq. (56) yields the following:

$$E_h\left(0^+\right) = 2 + \frac{1}{2} = \frac{5}{2}$$

That is

$$E_h\left(0^+\right) = \frac{5}{2} \tag{56b}$$

Near the crest, i.e., $\xi = h/D \to 0$, the rating behaves locally like a power law $Q \propto h^{2.5}$. So, E_h, the log-slope or "percent-to-percent" sensitivity, says a 1% change in flow depth produces about a 2.5% change in discharge. Physically, that 2.5 comes from three factors multiplying at tiny heads: (1) the Torricelli velocity scale grows like $\sqrt{h}$, (2) the available width of a circular opening grows like $\sqrt{h}$ right above the crest, and (3) integrating over depth contributes another factor h; together $\sqrt{h} \times \sqrt{h} \times h = h^2$., that's what the discharge Eq. (18) shows. Thus, the rating is *most sensitive* to flow depth very near onset.
At full height, corresponding to $\xi \to 1$, one may write what follows. From the exact kernel values: P(1) = 4/15 (circular), and, by the elliptic kernel's exact derivative at full height, which carries over under $\beta = \xi$, one may derive $\Psi'(1) = -1/15$, hence $\mathrm{P}'(1) = -1/15$, according to Eq. (3d). Therefore, Eq. (56) gives what follows:

$$E_h(1) = 2 + 1 \times \frac{\mathrm{P}'(1)}{\mathrm{P}(1)} = 2 + \frac{-1/15}{4/15} = 2 - \frac{1}{4} = \frac{7}{4} \tag{56c}$$

That is

$$E_h(1)=\frac{7}{4} \tag{56d}$$

It can be observed that, for the circular weir, E_h monotonically relaxes from 2.5 near onset to 1.75 at full height. In addition, one may deduce from Eq. (56d), that at full height, $\xi\to 1$, the rating's local behavior is $Q \propto h^{1.75}$. Interpretationally, a 1% change in flow depth now yields only about a 1.75% change in discharge. The geometry explains the drop from 2.5 to 1.75: as the water level approaches the top of the circular opening, the added wetted area per unit flow depth becomes a thin lens with rapidly diminishing width; the kernel's slope is negative there, i.e., $\mathrm{P}'(1) = -1/15$, so the geometric "gain" weakens and the flow depth-elasticity relaxes. In short, once the opening is nearly fully wetted, extra flow depth adds relatively little effective area, so Q becomes *less sensitive* to h.

Two quick corollaries that help readers: (1) E_h is the local exponent of the Q–h law, so it directly tells the error magnification: $\Delta Q/Q \approx E_h \times \Delta h/h$; (2) the endpoint values of the flow depth-elasticity E_h come from the loss-free kernel; multiplying by a discharge coefficient C_d doesn't change E_h because elasticities ignore constant factors.

For the circular weir, the elasticity E_h at $\xi = 0.50$ is identical to the value obtained at $\beta = 0.50$ for elliptic and semi-elliptic weirs; more generally, the computation for any ξ proceeds in exactly the same way. Accordingly, the procedure outlined in the section on E_h sensitivity for elliptic/semi-elliptic weirs applies to circular weirs without modification. The rationale is straightforward: all three geometries share the same geometry–flow depth kernel Ψ under the mapping $\beta \mapsto \xi = h/D$. The only difference is a geometric prefactor, which cancels in the logarithmic definition of elasticity, so E_h depends solely on the common kernel evaluated at the same nondimensional depth.

Sensitivity to geometry D

By definition, the following can be written:

$$S_D=\frac{\partial Q_{Th}}{\partial D} \tag{57}$$

Let Eq. (18) be written in the following reduce form:

$$Q_{Th}=C\left(D^{1/2}\,h^{2}\right)\mathrm{P}\left(\xi\right) \tag{58}$$

with

$$C=2\sqrt{2g} \tag{59}$$

Let consider the following quantities:

$$S_D = \frac{\partial Q_{Th}}{\partial D} = C\,h^2 \left[\frac{\partial\left(\sqrt{D}\right)}{\partial D} \mathrm{P}\left(\xi\right) + \sqrt{D}\,\frac{\partial \mathrm{P}\left(\xi\right)}{\partial D} \right] \tag{60}$$

The following elementary derivatives can be written as follows:

$$\frac{\partial\left(\sqrt{D}\right)}{\partial D} = \frac{1}{2} D^{-1/2} \tag{61}$$

$$\frac{\partial \mathrm{P}\left(\xi\right)}{\partial D} = \mathrm{P}'\left(\xi\right)\frac{\partial \xi}{\partial D} \tag{62}$$

The chain rule for $\xi = h/D$, at h fixed is as follows:

$$\frac{\partial \xi}{\partial D} = -\frac{h}{D^2} = -\frac{\xi}{D} \tag{63}$$

Thus, Eq. (60) becomes as follows:

$$S_D = 2\sqrt{2g}\,h^2 \left[\frac{1}{2} D^{-1/2}\,\mathrm{P}\left(\xi\right) + \sqrt{D}\,\mathrm{P}'\left(\xi\right)\left(-\frac{\xi}{D}\right) \right] \tag{64}$$

After rearrangement, Eq. (64) reduces to the following final form:

$$S_D = 2\sqrt{2g}\,\frac{h^2}{\sqrt{D}} \left[\frac{1}{2} \mathrm{P}\left(\xi\right) - \xi\,\mathrm{P}'\left(\xi\right) \right] \tag{65}$$

The two-term bracket can be interpreted as follows:

(1) $+\frac{1}{2}\mathrm{P}\left(\xi\right)$ comes from the explicit $\sqrt{D}$;

(2) $-\xi\,\mathrm{P}'\left(\xi\right)$ comes from the implicit dependence P(ξ) has on D through $\xi = h/D$, hence the minus sign.

On other hand, Eq. (18) allows writing the following:

$$\ln Q = \text{Constant} + \frac{1}{2}\ln D + 2\ln h + \ln \mathrm{P}\left(\xi\right) \tag{66}$$

Differentiating with respect to ln$D$, while holding h fixed, and considering Eq. (25), yields the following:

$$E_D = \frac{D}{Q}\left(\frac{\partial Q}{\partial D}\right) = \frac{1}{2} + \frac{\partial \mathrm{P}(\xi)}{\partial D} = \frac{1}{2} + \frac{\partial \ln \mathrm{P}(\xi)}{\partial \ln \xi}\frac{\partial \ln \xi}{\partial \ln D} = \frac{1}{2} - \xi\frac{\mathrm{P}'(\xi)}{\mathrm{P}(\xi)} \quad (67)$$

That is

$$E_D = \frac{D}{Q}\left(\frac{\partial Q}{\partial D}\right) = \frac{1}{2} - \xi\frac{\mathrm{P}'(\xi)}{\mathrm{P}(\xi)} \quad (67a)$$

That is

$$E_D = \frac{1}{2} - \xi\frac{\mathrm{P}'(\xi)}{\mathrm{P}(\xi)} \quad (67b)$$

Considering both Eqs. (56) and (67b), yields the following:

$$E_h + E_D = \left(2 + \xi\frac{\mathrm{P}'(\xi)}{\mathrm{P}(\xi)}\right) + \left(\frac{1}{2} - \xi\frac{\mathrm{P}'(\xi)}{\mathrm{P}(\xi)}\right) = \frac{5}{2} \quad (68)$$

Thus, we obtain the elasticity sum rule for the circular weir, as follows:

$$E_h + E_D = \frac{5}{2} \quad (68a)$$

Hence the “sensitivity budget” is fixed: whenever geometry makes the rating more (less) sensitive to flow depth, it makes it equally less (more) sensitive to diameter, and the total stays at 2.5 for every ξ. From a physical interpretation point view, the following can be state: (1) The constant 2.5 decomposes as 2, from the h^2 in the discharge law, + 0.5 from the explicit $\sqrt{D}$; the remaining shape–flow depth coupling $\pm\xi\times \mathrm{P}'/\mathrm{P}$ merely redistributes sensitivity between h and D without changing their sum.
This identity is kernel-agnostic: it holds for the exact $\mathrm{P}(\xi)$ and for any surrogate that preserves the same normalization, because it is an algebraic consequence of Eqs. (56) and (67b).

In short, Eq. (68a) is a conservation law for sensitivities in the circular normalization: the geometry can only trade sensitivity between h and D; it cannot change their total, which is fixed at 5/2 by the structure of the rating law.

Regarding the endpoints check from the Kernel physics, one may derive the following:

For $\xi\to 0$:

$$\mathrm{P}(\xi) \sim \frac{\pi}{8}\sqrt{\xi} \quad (69)$$

and

For $\xi \to 1$:

$$\mathrm{P}\left(1\right)=\frac{4}{15} \tag{70}$$

Thus, near onset, the following can be written:

$$\mathrm{P}^{'}\left(\xi\right)\sim\frac{\pi}{16}\xi^{-1/2} \tag{71}$$

According to Eq. (65), the following can be derived:

$$\left[\frac{1}{2}\mathrm{P}\left(\xi\right)-\xi\,\mathrm{P}^{'}\left(\xi\right)\right]\sim\frac{\pi}{16}\left[\sqrt{\xi}-\sqrt{\xi}\right]=0 \tag{72}$$

This the leading order; i.e.; the dominant term in the asymptotic expansion as $\xi \to 0$. Because the $\sqrt{\xi}$-terms cancel, the first member of Eq. (72) is smaller than any constant multiple of $\sqrt{\xi}$; it is of higher order than $\sqrt{\xi}$; its next non-zero term in higher order in ξ, hence, S_D expressed by Eq. (65), satisfies $S_D = o(\sqrt{\xi})$ as $\xi \to 0$, i.e.:

$$\lim_{\xi\to 0}\frac{S_D}{\sqrt{\xi}}=0 \tag{73}$$

Below is a tight parenthetical we drop in right after the near-crest cancellation sentence, plus one clarifying sentence about the little-*o* claim. In particular, because the exact kernel, expressed by Eq. (20), admits a half-integer small-ξ expansion as follows:

$$\mathrm{P}\left(\xi\right)=\frac{\pi}{8}\sqrt{\xi}+c_{3/2}\xi^{3/2}+c_{5/2}\xi^{5/2}+.... \tag{74}$$

thus, the first non-vanishing term in the first member in Eq. (72) scales like $\xi^{3/2}$; if one uses a smooth surrogate, i.e.:

$$\mathrm{P}\left(\xi\right)=\frac{\pi}{8}\sqrt{\xi}+c_1\xi+c_{3/2}\xi^{3/2}+.... \tag{75}$$

then the remainder scales like ξ. In both cases the first member in Eq. (72) is $o(\xi)$.

It is worth noting to recall that $c_{3/2}$, $c_{5/2}$, …in Eq. (74) are the constant coefficients of the *higher-order* terms in the small-flow depth, i.e., $\xi \to 0$, asymptotic expansion of the circular kernel $\mathrm{P}(\xi)$ beyond the leading $(\pi/8) \times \sqrt{\xi}$ term. For the exact circular kernel expressed by Eq. (74), the constant coefficients are geometry-dependent.

Herein, *geometry-dependent* refers to dependence on dimensionless shape parameters, e.g., an ellipse's aspect ratio, not on absolute size. Because the circular kernel $P(\xi)$ is defined on the scaled variable $\xi = h/D$, its small-ξ coefficients $c_{3/2}$, $c_{5/2}$, …are pure numbers for the circular shape, and thus independent of g, D, and h. The size D enters only via the prefactor $2 \times \sqrt{(2g)} \times \sqrt{D}$ and the argument $\xi = h/D$, not through these coefficients.

SEMI-EMPIRICAL C_D-MODELS

The present section of the study develops a practical, physics-respecting framework for predicting the discharge coefficient, C_d, in sharp-crested meters with elliptic, semi-elliptic, and circular openings.

The authors underscore that the proposed discharge-coefficient C_d- models are not ad-hoc curve fits but principled translations of canonical mathematical kernels, most notably Hill/Michaelis–Menten saturations and stretched-exponential (Weibull) forms, into the hydraulics of elliptic, semi-elliptic, and circular weirs. Cast in nondimensional variables $X = h/b$ and the compound contraction index Γ, these families are complemented by compact rational-polynomial representations for the contraction-limited ceiling $C\infty(\Gamma)$ and are calibrated to enforce the key physical requirements: boundedness ($0 < C_d \leq C\infty < 1$), strict monotonicity with respect to X, and the correct shallow- and deep-flow asymptotes. The resulting parameterization, typically ($C\infty$, θ, m) for the saturation families, retains clear physical meaning (ceiling, half-saturation "knee," and steepness) while remaining sufficiently simple for robust estimation and cross-geometry comparison.

Starting from a clean dimensional analysis, the text isolates two similarity controls that matter most in the field: a relative flow-depth variable that captures how "thick" the driving flow depth is compared to the opening's span, and a compound contraction index that merges lateral and vertical contractions into one interpretable knob. These choices strip away secondary effects (viscosity and capillarity under appropriate operating ranges) and focus the modelling on what actually drives meter behaviour across regimes.

On top of this foundation, it is introduced herein eight complementary, semi-empirical families, Asymptotic One-Minus (AOM), Reciprocal-Power Saturation (RPS), Bounded Padé Saturation (BPS), Half-Saturation Exponential (HSE), Arctan Saturation (ATS), Residual-Difference Pyramid (RDP), Hill Saturation (HIS) model, and Exponential Saturation (SES) model that are expressly designed to be (1) bounded below unity, (2) monotone with increasing relative flow depth, and (3) asymptotically correct, plateauing at a contraction-limited ceiling at large flow depth while avoiding unphysical collapse at very low depth. Each model keeps parameters few, interpretable, and tied directly to geometry and operating regime, making them robust to fit by constrained least squares and easy to carry into design charts and calibration workflows.

Beyond point prediction, the presents section derives a closed-form elasticity of C_d with respect to upstream flow depth. This turns the models into tools for uncertainty propagation and sensitivity analysis, clarifying when flow depth effects dominate and when contraction effects matter more, precisely the information needed for defensible metering and decision-making in the field. Because geometry is factored into a dimensionless kernel and C_d represents real-flow effects multiplicatively, the same methodology transfers cleanly across opening shapes with only a change of similarity variables and a refit of coefficients.

In short, the present section of the study provides a disciplined path from first principles to fit-ready models, giving practitioners a compact set of curves that rise fast when shallow, flatten when deep, never exceed physical limits, and come with the diagnostics needed to quantify confidence.

Influencing parameters and C_d-dependency

The authors successfully conduct a systematic investigation, such as a dimensional analysis, to rigorously identify all parameters governing the discharge coefficient C_d. The authors state that the discharge coefficient C_d may be governed by the following functional relationship, excluding the approach-flow Froude number Fa, i.e., assuming a negligible approach-velocity head, and the crest-thickness ratio t/h, i.e., a thin, sharp crest:

$$C_d = f\left(h/a, a/b, 2b/B, P/h, \sqrt{gh}\,h/\nu, \rho g h^2/\sigma\right) \tag{76}$$

The two last terms can be identified as the Reynolds number based on h (Re) and the Bond number (Bo), or, equivalently for capillarity, the Weber number based on h (We), respectively. In a well-designed installation producing appropriate discharge and upstream flow depths, one may write that Re $\gg$ 1 and We $\gg$ 1, i.e., inertial forces dominate viscous and surface-tension effects; the previous C_d governing relationship can be simplified accordingly by neglecting viscosity and capillarity.

Moreover, one can compress the Π-set derived earlier by grouping the lateral and vertical contraction ratios into a single compound contraction index, while keeping only the minimum additional groups needed to capture shape and operating regime. Here's a clean reduction, while neglecting the viscosity and surface tension effects.

Let the following:

Semi-height penetration index: $2\beta = h/a$, $0 \le \beta \le 1$, for the full elliptic weir. The ratio $h/(2a)$ is the "penetration-flow depth index"; this ratio tells us how deeply the available flow depth "penetrates" the vertical extent of the aperture. Thus, this 'penetration' concept concerns the flow depth-to-aperture-height ratio $h/(2a)$, even if the gauge is located far upstream.

Aspect ratio, or the ellipse shape: $\lambda = a / b$

Compound Contraction Index (lateral + vertical), introduced recently in the literature related to flow measurement:

$$\Gamma = \frac{2b / B}{1 + P / h} \tag{77}$$

with $\Gamma \in]0, 1[$, and B the rectangular approach channel width.
It is therefore highly probable that the discharge coefficient C_d exhibits a strong dependence on the upstream flow depth h, either directly or through associated dimensionless parameters.

Thus, the functional relationship f, previously defined by Eq. (76), reduces to the following:

$$C_d = \Omega\left(\beta, \lambda, \Gamma\right) \tag{78}$$

Moreover, the functional form Ω can definitely be rewritten by compressing the two variables β and λ into a single dimensionless parameter, since $\beta \times \lambda = X/2 = h/(2b)$, which allows defining the following ratio:

$$X = \frac{h}{b} \tag{79}$$

$X = h/b$. Hence, the functional relationship Ω reduces to the following final form:

$$C_d = \Upsilon\left(X, \Gamma\right) \tag{80}$$

It must be emphasis that the ratio $X = h/b$ is a flow depth-based similarity variable, the upstream flow depth h normalized by the lateral half-width, the semi-horizontal axis, of the semi-elliptical opening. It measures how "thick" the driving flow depth is relative to the span of the opening. In other words, it compares the flow's gravitational driving scale to the aperture's lateral size. As $X = h/b$ increases, the low-flow depth (thin-nappe) losses become relatively less important and the discharge coefficient C_d moves toward its contraction-controlled ceiling, whereas small $X = h/b$ indicates a thin nappe over a wide opening, where entrance, curvature, and boundary-layer effects are proportionally stronger and C_d is lower. In other words, $X = h/b$ is the "relative flow depth" with respect to the opening's width, and it controls the transition from loss-dominated, i.e., small h/b, to asymptotically efficient, i.e., large h/b, discharge behavior.

Asymptotic One-Minus (AOM) model

Accordingly, if an analytical derivation of the governing law for the discharge coefficient is not available, which would clearly constitute the ideal solution, the users should supply a physics-consistent, empirically calibrated alternative against experimental data. This is the alternative One-Minus (AOM) model that stands out as a robust semi-empirical approach that balances physical plausibility with data-driven adaptability, making it particularly well-suited for hydraulic applications where a purely analytical derivation is not available. Using the measured variables h, b, B, P, and Q, the user must estimate the parameters of a robust saturating form that respects the physical bounds of C_d, and the monotonic approach to a contraction-controlled limit. Moreover, this model preserves the correct limits (monotone in h/b), contraction captured by Γ, and $C_d \rightarrow C_\infty(\Gamma) < 1$ as $h/b \rightarrow \infty$ as indicated in the Eq. (81) below, and is fit-ready on the dataset. The AOM model provides a minimal, interpretable flow depth–contraction rating surface $C_d(h/b, \Gamma)$, i.e., a family of rating curves $C_d(h/b)$ parameterized by the compound contraction index Γ, that honours the physics and calibrates cleanly against experimental data, making it a strong alternative when a closed-form analytical law for C_d is unavailable, as overmentioned.

According to the authors' calculation, the discharge coefficient C_d is given by the following Asymptotic "One-Minus" (AOM) model:

$$C_d\,(h/b;\Gamma) = C_\infty(\Gamma) - \frac{A(\Gamma)}{1+(h/b)^m} \tag{81}$$

where

$$C_\infty\left(\Gamma\right) = c_0 + c_1\Gamma + c_2\Gamma^2 \tag{82}$$

$$A\left(\Gamma\right) = d_0 + d_1\left(1-\Gamma\right) \tag{83}$$

The derivation of the previous C_d-formulation follows the asymptotic 'One-Minus' principle: the discharge coefficient C_d is expressed as an upper bound, $C_\infty(\Gamma)$, minus a diminishing flow depth-deficit term, $A(\Gamma)/(1+X^m)$. This guarantees both the correct asymptotic ceiling and the physically consistent decay of losses with increasing flow depth. Herein, "ceiling" means the upper bound or maximum limit that the discharge coefficient C_d can approach, but never exceed. In the AOM model, that ceiling is written as $C_\infty(\Gamma)$. Physically, it represents the value of C_d at very large relative flow depths, i.e., $h/b \rightarrow \infty$, as it can be seen in the previous C_d-relationship, when viscous and scale effects vanish and the discharge coefficient is controlled only by contraction geometry.

Herein, according to Eq. (83), d_0 is the baseline deficit at weak contraction, i.e., $\Gamma \rightarrow 1$; d_1 measures the extra deficit as contraction strengthens, i.e., smaller Γ. The function $A(\Gamma)$ is the flow depth-deficit amplitude: at very small relative flow depth h/b, i.e., a thin nappe, the discharge coefficient drops below its contraction-controlled ceiling $C_\infty(\Gamma)$ by an amount $A(\Gamma)$.
Weak contraction means $\Gamma \rightarrow 1$: the opening nearly spans the channel ($2b/B \rightarrow 1$) and/or the sill is low relative to the flow depth, i.e., $P/h \rightarrow 0$. In that case, $A(\Gamma \rightarrow 1) = d_0$. Stronger contraction means Γ gets smaller, i.e., narrower opening $2b/B\downarrow$ and/or larger $P/h\uparrow$. Also, c_0 is the asymptotic C_d at strongest contraction, meaning: $C_\infty(\Gamma \rightarrow 0) = c_0$ is the large-flow depth (viscous losses negligible) discharge coefficient when contraction is most severe, i.e., small Γ. The interpretation is that baseline ceiling set by geometry in the worst contraction case. The coefficient c_1 is the initial slope of the contraction asymptote, meaning: the derivative $C_\infty'(\Gamma)\big|_{\Gamma \rightarrow 0} = c_1$. It measures how quickly the large-flow depth ceiling improves as contraction relaxes from its strongest state. The interpretation is that higher c_1 implies C_∞ rises more rapidly with Γ near Γ = 0. The coefficient c_2 is the

curvature of the contraction asymptote, meaning: controls whether $C\infty(\Gamma)$ is slightly concave ($c_2 < 0$) or convex ($c_2 > 0$) over $\Gamma \in]0, 1[$. The derivative is $C\infty'(\Gamma) = c_1 + 2c_2\Gamma$. The interpretation is that it lets the fit capture mild nonlinearity in how contraction affects the asymptotic coefficient. The practical constraint lies in the fact that it keeps $C\infty$, requiting $c_1 > 0$ and $c_1 + 2c_2 \geq 0$; also enforces the following inequalities:

$$0 < c_0 < c_0 + c_1 + c_2 < 1 \tag{84}$$

Finally, the exponent m in Eq. (81) is the flow depth-approach rate to the asymptote, meaning: it governs how fast C_d approaches $C\infty(\Gamma)$ as $X = h/b$ increases in $C_d = C\infty(\Gamma) - A(\Gamma) / (1 + X^m)$. The interpretation is that larger m implies that the low-flow depth deficit collapses faster with increasing flow depth; smaller m implies a more gradual approach. It also sets the flow depth-elasticity of C_d. Furthermore, the exponent m is positive, i.e., $m > 0$, and, practically, it takes values between 0.6 and 2. For this study, no specific value of m is available; therefore, it should be estimated in accordance with the below procedure based on experimental measurements of the governing parameters.

Using Eq. (81) overmentioned, the six involved coefficients, i.e., c_0, c_1, c_2, d_0, d_1, m) should be calibrated by constrained nonlinear least squares using the experimental dataset h, b, B, P, and Q, with the predictors $X = h/b$ and $\Gamma = (2b/B) / (1+P/h)$, and the response $C_d = Q/Q_{Th}$, where Q_{Th} has already been defined as the theoretical discharge from the governing weir equation.

It is worth noting that since the paper's theory isolates geometry in a dimensionless kernel and appends C_d multiplicatively for real-flow effects, thus the *same kernel* governs elliptic, semi-elliptic, and circular openings; so, the C_d layer is portable across shapes. Consequently, the C_d–AOM based model is valid for circular sharp-crested weirs as well, provided using the circular specialization of the similarity variables and refit the coefficients on circular data.

Reciprocal-Power Saturation (RPS) model

The RPS model is introduced as a compact, physics-guided parameterization of the discharge coefficient that operates on the two key similarity controls established earlier, relative flow depth X, i.e., the upstream depth normalized by the weir's half-width, and a compound contraction index Γ that aggregates lateral and vertical contractions. It encodes two essentials of meter physics: (1) strict boundedness and monotonic approach to a contraction-limited ceiling at large relative depth, and (2) a progressive collapse of low-flow depth losses as flow depth increases. With a small set of interpretable parameters tied directly to contraction and depth effects, RPS-based C_d model, or simply C_d-RPS, is easy to calibrate by constrained least squares, numerically stable, and remains strictly below unity under all admissible conditions. It also connects naturally to the previously proposed "one-minus" family, recovering similar behavior for small deficits, while providing superior control of the very-low-depth regime through its reciprocal-power saturation. As such, RPS delivers a transparent, fit-ready surface C_d (relative flow depth, contraction) that honors the asymptotic structure of the problem, supports clear uncertainty propagation, and slots cleanly into design and field calibration workflows.

As it has been demonstrated in the previous section, the dimensional analysis show that the discharge coefficient C_d for the elliptic weir solely depends on the compound contraction index Γ defined by Eq. (77), and the dimensionless ratio X, defined by Eq. (79).

The new semi-empirical C_d-model, introduced herein, is defined as follows:

$$C_d(X;\Gamma) = \frac{C_\infty(\Gamma)}{1 + A(\Gamma)X^{-m}} \tag{85}$$

with $m > 0$

$C_\infty(\Gamma)$, and $A(\Gamma)$ are defined by Eqs. (82) and (83), respectively. In addition, the inequalities defined by Eq. (84) is still valid herein.

The model is strong due to the following physics-consistent bounds:

$$0 < C_d < C_\infty(\Gamma) < 1 \tag{86}$$

and

$C_d \uparrow$ with X, $C_d \uparrow$ with weaker contraction, i.e., larger Γ.

The model presents a clean asymptote, i.e.:

$$X \to \infty \Rightarrow C_d \to C_\infty(\Gamma) \tag{87}$$

In addition, the model is numerically stable and parsimonious since it presents the following three interpretable building blocks, with light constraints, meaning that no risk of $C_d > 1$ occurs:

$$\{C_\infty(\Gamma), A(\Gamma), m\}$$

It connects to AOM since for small deficits, i.e., $z \equiv A(\Gamma)\times X^{-m} \ll 1$, the following can be written:

$$\frac{1}{1+z} \approx 1 - z \tag{88}$$

Thus, RPS reduces to what follows:

$$C_d(X;\Gamma) \approx C_\infty(\Gamma)\left[1 + A(\Gamma)X^{-m}\right] = C_\infty(\Gamma) + \underbrace{C_\infty(\Gamma)A(\Gamma)X^{-m}}_{\text{scaled deficit}} \tag{85a}$$

which is the same "one-minus" structure used in AOM at large X (with the deficit amplitude scaled by $C\infty$). This small-deficit step is precisely what's captured in Eq. (88), derived from Eq. (85).

C_d-RPS behaves like a subtractive one-minus law but remains strictly bounded and often fits better at very low flow depths.

(1) Build predictors from your measurements h, b, B, P, Q: $X = h/b$, $\Gamma = (2b/B)/(1+P/h)$; response $C_d = Q/Q_{Th}$; (2) Parameterize $C\infty(\Gamma)$ and $A(\Gamma)$ as previously indicated; impose simple box constraints, e.g. $0 < c_0 < c_0 + c_1 + c_2 < 1$; $d_0 \geq 0$, $d_1 \geq 0$; $m > 0$; (3) Validate with k-fold or leave-one-geometry-out; report max/mean relative errors, not just R^2.

C_d-Elasticity **(for error propagation)**

Let's define following:

$$X = \frac{h}{b} \tag{79}$$

as the relative flow depth, related to the half horizontal axis of the elliptic weir.

$$k = \frac{2b}{B} \tag{89}$$

As the lateral contraction of the elliptic weir, applicable also to semi-elliptic and circular weirs, recalling that B is the rectangular approach channel width.

$$\Gamma = \frac{k}{1+P/h} = k\frac{h}{h+P} \tag{77a}$$

As the dimensionless compound contraction index.

(1) **Derivative of Γ with respect to ln*h***

A convenient closed form is the following:

$$\frac{\partial \Gamma}{\partial \ln h} = h\frac{d\Gamma}{dh} = \Gamma\left(1 - \frac{\Gamma}{k}\right) \tag{90}$$

As $h \to \infty$, $\Gamma \to k$ according to Eq. (77), and the above term expressed by Eq. (90) fades to 0.

(2) **Flow depth-elasticity of C_d**

Define the following:

$$\alpha\left(X,\Gamma\right) = A\left(\Gamma\right)X^{-m} \tag{91}$$

Then, the exact logarithmic sensitivity, i.e., elasticity E_h, of C_d to h is the following:

$$E_h^{(C_d)} \equiv \frac{\partial \ln C_d}{\partial \ln h} = \mathrm{E} + \mathrm{M} \times \mathrm{N} \tag{92}$$

where

$$\mathrm{E} = \underbrace{\frac{m\alpha}{1+\alpha}}_{\text{explicit in } h \text{ via } X=h/b} \tag{93}$$

$$\mathrm{M} = \underbrace{\frac{C_\infty^{'}(\Gamma)}{C_\infty(\Gamma)} - \frac{A^{'}(\Gamma)X^{-m}}{1+A(\Gamma)X^{-m}}}_{\text{effect of } \Gamma} \tag{94}$$

$$\mathrm{N} = \underbrace{\Gamma\left(1-\frac{\Gamma}{k}\right)}_{\text{chain rule } d\Gamma/d\ln h} \tag{95}$$

This splits cleanly into the following:

- a direct flow depth h term (E), dominated by m when X is small; and
- a contraction term (N), driven by how $C\infty$ and A vary with Γ, modulated by $\Gamma(1-\Gamma/k)$.

From this, the ordinary derivative follows immediately as:

$$\frac{dC_d}{dh} = \frac{C_d}{h} E_h \tag{96}$$

(3) **Plug-in for the suggested parameterizations**

If using the simple forms previously suggested, namely Eqs. (82) and (83), the following can be written:

$$C_\infty^{'}(\Gamma) = c_1 + 2c_2\Gamma \tag{97}$$

$$A^{'}(\Gamma) = -d_1 \tag{98}$$

and the elasticity, expressed by Eq. (92), becomes as follows:

$$E_h = \mathrm{E} + \left[\mathrm{I} + \mathrm{Z}\right]\mathrm{N} \tag{99}$$

where

$$\mathrm{I} = \frac{c_1 + 2c_2\Gamma}{c_0 + c_1\Gamma + c_2\Gamma^2} \tag{100}$$

$$\mathrm{Z} = \frac{d_1 X^{-m}}{1 + \left\{d_0 + d_1(1-\Gamma)\right\} X^{-m}} \tag{101}$$

$$\alpha(X,\Gamma) = \left[d_0 + d_1(1-\Gamma)\right] X^{-m} \tag{102}$$

(4) **Physical interpretation**

- For large flow depth, X → ∞ according to Eq. (79); $\alpha \to 0$ according to Eq. (102), and $\Gamma \to \beta$ according to Eq. (77). Hence $E_h \to 0$ according to Eq. (99) because E = 0 ($\alpha \to 0$) and N = 0 ($\Gamma \to k$): According to Eq. (81), the discharge coefficient C_d approaches its contraction-limited ceiling $C_d = C\infty(k)$ and stops changing with h.

- For small flow depth, according to Eq. (102) $\alpha \gg 1$; thus, according to Eq. (93) one may write $m\alpha/(1+\alpha) \approx m$, while Γ is still well below k, according to Eq. (77), so the contraction term N, expressed by Eq. (95), contributes modestly. Thus, as a net effect, C_d rises rapidly with h, but remains bounded.

- Monotonicity and bounds: With $m > 0$, $A(\Gamma) \geq 0$, and $0 < C\infty(\Gamma) < 1$, the model keeps $0 < C_d < C\infty(\Gamma) < 1$ and $E_h \geq 0$ under ordinary conditions, matching meter physics.

(5) **How to use this in practice**

(5.1) Compute:

$$X = \frac{h}{b}\text{, Eq. (79), and } \Gamma = k\,\frac{h}{h+P}\text{, Eq. (77a).}$$

(5.2) Evaluate C∞(Γ) from Eq. (82), and α from Eq. (102).

(5.3) Plug into E_h, Eq. (99), to get the flow depth-elasticity contributed by C_d.

(5.4) For total discharge elasticity, add this to the theoretical (loss-free) elasticity of $Q_{Th} - h$. That is meaning the following:

$$E_h = E_h^{(Th)} + E_h^{(C_d)} \tag{103}$$

where

$E_h^{(Th)}$ is from the loss-free evaluator Q_{Th}–h, and

$E_h^{(C_d)}$ is from the discharge coefficient C_d., as it is expressed by Eq. (92).

It is emphasis to note that the theoretical framework factors geometry into a dimensionless kernel and represents real-flow effects through a multiplicative C_d; because the same kernel governs elliptic, semi-elliptic, and circular apertures, the C_d parameterization transfers across shapes. Accordingly, the C_d–RPS model is fully applicable to circular sharp-crested weirs, provided that the circular specialization of the similarity variables is adopted and the coefficients are refitted on circular datasets.

Bounded Padé Saturation (BPS) model

In the present section, the authors we introduce the Bounded Padé Saturation (BPS) model as a compact, physics-respecting parameterization of the discharge coefficient C_d that combines strict bounds with flexible curvature. Built on the same similarity controls used throughout, relative flow depth and a compound contraction index, BPS employs a bounded rational (Padé-type) form that (1) is provably monotone in flow depth, (2) remains strictly below a contraction-limited ceiling for all admissible conditions, and (3) offers a tunable mid-range shape via two independent "deficit" knobs. This gives the model enough agility to fit datasets that bend slightly before plateau, without sacrificing asymptotic correctness: at large flow depth, it approaches the ceiling smoothly; at very low flow depth it avoids non-physical collapse. Locally (small deficits), BPS reduces to the familiar "one-minus" behaviour used in AOM, while globally it inherits the robustness of saturation models like RPS, delivering a best-of-both blend that is easy to calibrate under simple box constraints, numerically stable, and directly interpretable for design, calibration, and error-propagation analyses via E_h. The Padé saturation model is not only valid for elliptic and semi-elliptic weirs, but it can be also extended to circular weirs.

This model uses the same dimensionless parameters than those used in C_d-AOM and C_d-RPS based models, namely X, k, and Γ, expressed by Eqs. (79), (89), and (77), respectively.

The C_d-Bounded Padé Saturation (BPS) model is expressed in the following form:

$$C_d\left(X;\Gamma\right)=C_\infty(\Gamma)\frac{1+\gamma(\Gamma)\,X^{-m}}{1+\varphi\left(\Gamma\right)X^{-m}} \tag{104}$$

with

$$m>0 \tag{105}$$

$$0\leq\gamma\left(\Gamma\right)<\varphi\left(\Gamma\right) \tag{106}$$

$$0<C_\infty\left(\Gamma\right)<1 \tag{107}$$

$\gamma(\Gamma)$ and $\varphi(\Gamma)$ will be well-defined in the next section, especially:

$$\gamma(\Gamma) < \varphi(\Gamma) \tag{108}$$

Why BPS is strong

(1) **It presents strict bounds, everywhere, such as**:

$$0 < C_d \leq C_\infty(\Gamma) \tag{109}$$

(2) **According to Eq. (104), the following can be deduced**:

$$\lim_{X \to \infty} C_d = C_\infty(\Gamma) \tag{110}$$

At very low flow depth, i.e, $X \to 0$ according to Eq. (79), and considering Eq. (104), one may write the following:

$$\underset{X \to 0}{C_d}(X;\Gamma) = C_\infty(\Gamma)\frac{\gamma(\Gamma)}{\varphi(\Gamma)} \tag{111}$$

Thus, there is no unphysical collapse.

(3) **Monotone in flow depth**

For $m > 0$ [Eq. (105)], and $\gamma < \varphi$ [Eq. (108)], C_d increases with X, decreases with X^{-m}, matching meter physics.

(4) **Curvature control**

The two "deficit" knobs γ, and φ, independently tune mid-range curvature without breaking the bounds; this often fits better than single-knob models when data bend slightly before plateau.

(5) **Connects to AOM / RPS**

For small deficits t, such as the following:

$$t \equiv X^{-m} << 1 \tag{112}$$

the following can be written:

$$\frac{1+\gamma t}{1+\varphi t} \approx 1-(\varphi-\gamma)t \tag{113}$$

Thus, BPS reduces to a classic "one-minus" law with deficit amplitude ($\varphi - \gamma$), i.e., it locally recovers AOM-like behaviour while remaining strictly bounded like RPS.

A simple, interpretable parameterization

$$C_\infty(\Gamma) = c_0 + c_1\Gamma + c_2\Gamma^2 \tag{82}$$

$$\gamma(\Gamma) = a_0 + a_1(1-\Gamma) \tag{114}$$

$$\varphi(\Gamma) = \gamma(\Gamma) + \delta_0 + \delta_1(1-\Gamma) \tag{115}$$

with the following box constraints:

$$0 < c_0 < c_0 + c_1 + c_2 < 1 \tag{84}$$

$$a_0, a_1, \delta_0, \delta_1 \geq 0 \tag{116}$$

$$\delta_0 + \delta_1 > 0 \tag{117}$$

$$m \in (0.6,\ 2.5) \tag{118}$$

These ensure, for admissible Γ, the following:

$$0 < C_d < C_\infty(\Gamma) < 1 \tag{86}$$

and

$$\gamma(\Gamma) < \varphi(\Gamma) \tag{108}$$

C_d-Elasticity (for error propagation)

Let denote partial derivatives with respect to Γ by subscripts, such as the following:

$$C_{\infty,\Gamma} = \frac{dC_\infty}{d\Gamma} \tag{119}$$

Then, the following can be written:

$$E_h^{(C_d)} \equiv \frac{d\ln C_d}{d\ln h} = \omega_1 + \omega_2 \tag{120}$$

where

$$\omega_1 = mt\left(\frac{\varphi}{1+\varphi t} - \frac{\gamma}{1+\gamma t}\right) \tag{121}$$

$$\omega_2 = \Gamma\left(1-\frac{\Gamma}{k}\right)\left[\frac{C_{\infty,\Gamma}}{C_\infty}+t\left(\frac{\gamma_\Gamma}{1+\gamma t}-\frac{\varphi_\Gamma}{1+\varphi t}\right)\right] \tag{122}$$

- For large flow depths, i.e., $h \to \infty$, on may write $t \to 0$, or $X \to \infty$, since t is defined by $t = X^{-m} = (h/b)^{-m}$. Thus, ω_1 in Eq. (121) is equal to zero. Eq. (122) reduces to the following:

$$\omega_2 = \Gamma\left(1-\frac{\Gamma}{k}\right)\frac{C_{\infty,\Gamma}}{C_\infty} \tag{122a}$$

According to Eq. (77a), for $h \to \infty$, it can be written that $\Gamma \to k$, meaning that $\omega_2 = 0$, according to Eq. (122a). Thus, since $\omega_1 = 0$, and $\omega_2 = 0$, then C_d-elasticity = 0, according to Eq. (120), meaning the following:

$$E_h^{(C_d)} = 0 \tag{120a}$$

C_d plateaus at $C\infty(\Gamma)$.

It is emphasis that for large but finite flow depth, we keep the first non-zero terms to quantify *how fast* C_d-elasticity $E_h^{(Cd)}$ approaches 0. From the BPS expansion, the following can be written:

$$E_h^{(C_d)} \approx \underbrace{m(\varphi-\gamma)t}_{\text{explicit flow depth effect } \sim h^{-m}} + \underbrace{\Gamma\left(1-\frac{\Gamma}{k}\right)\frac{C_{\infty,\Gamma}}{C_\infty}}_{\text{contraction effect } \sim h^{-1}} + \underbrace{\Gamma\left(1-\frac{\Gamma}{k}\right)\left(\gamma_\Gamma-\varphi_\Gamma\right)t}_{\text{mixed term } \sim h^{-1-m}}$$

This is Eq. (120b).

What dominates?

$t = (h/b)^{-m}$ shrinks like h^{-m}.

If:

(1) If $m > 1$, the following term typically dominates at high flow depth:

$$\Gamma\left(1-\frac{\Gamma}{k}\right)$$

(2) If $m < 1$, the following explicit term dominates:

$$m(\varphi-\gamma)t$$

(3) If $m = 1$, both decay at the same rate; the larger coefficient wins.

In all cases, $E_h^{(Cd)} \to 0$ as $h \to \infty$; C_d approaches its ceiling $C\infty(\Gamma \to k)$.

In addition, setting in Eq. (120b), the following:

$$t = 0$$

and

$$\Gamma\left(1 - \frac{\Gamma}{k}\right) = 0$$

corresponding to $\Gamma \to k$, or $h \to \infty$ according to Eq. (77a), thus, Eq. (120b) reduces to the following:

$$E_h^{(C_d)} = 0$$

Thus, the exact result, given by Eq. (120a), is recovered.

- For small flow depth, i.e., $X << 1$, or $t >> 1$, the following can be written:

$$\frac{\varphi}{1 + \varphi t} = \frac{1}{t}\frac{1}{\varphi} + O\left(t^{-2}\right) \to 0 \tag{123}$$

Similarly, the following can be written:

$$\frac{\gamma}{1 + \gamma t} = \frac{1}{t}\frac{1}{\gamma} + O\left(t^{-2}\right) \to 0 \tag{124}$$

Thus, as $t >> 1$, from Eq. (121), one may write the following:

$$\omega_1 = 0 \tag{121a}$$

In addition, the second member in the brackets of ω_2 in Eq. (122) can be written as follows:

$$t\left(\frac{\gamma_\Gamma}{1 + \gamma t} - \frac{\varphi_\Gamma}{1 + \varphi t}\right) = t\left[\frac{\gamma_\Gamma}{t\left(\frac{1}{t} + \gamma\right)} - \frac{\varphi_\Gamma}{t\left(\frac{1}{t} + \varphi\right)}\right] \tag{122b}$$

The term t is cancelled, and for $t >> 1$, $1/t \to 0$. Thus, Eq. (122a) reduces to the following:

$$t\left(\frac{\gamma_\Gamma}{1 + \gamma t} - \frac{\varphi_\Gamma}{1 + \varphi t}\right) = \left(\frac{\gamma_\Gamma}{\gamma} - \frac{\varphi_\Gamma}{\varphi}\right) \tag{122c}$$

Thus, Eq. (122) reduces to the following:

$$\omega_2 = \Gamma\left(1-\frac{\Gamma}{k}\right)\frac{C_{\infty,\Gamma}}{C_\infty} \tag{122d}$$

Considering Eqs. (120), (121a), (122c), and (122d), the following can be written:

$$E_h^{(C_d)} = \Gamma\left(1-\frac{\Gamma}{k}\right)\left(\frac{C_{\infty,\Gamma}}{C_\infty}+\frac{\gamma_\Gamma}{\gamma}-\frac{\varphi_\Gamma}{\varphi}\right)+O\left(1/t\right) \tag{125}$$

Eq. (125) is the small-depth asymptote for the elasticity of the discharge coefficient within the BPS framework. It consolidates the upstream reductions just above it, where auxiliary terms are simplified and a cancellation removes the flow depth-ratio blow-up, into a single leading-order statement. The upshot is that the *direct* flow depth sensitivity dominates, while the *contraction* pathway survives only as a weaker correction. This nails the expected physics for a thin-nappe regime: elasticity is positive, bounded, and driven primarily by the exponent-controlled flow depth term.

Together with the large-depth results a few lines earlier, where elasticity dies out and the coefficient plateaus at its contraction-limited ceiling, Eq. (125) brackets the entire operating envelope. The user now has a clean "rises fast when shallow, flattens when deep" narrative that is internally consistent and easy to propagate through uncertainty analyses.

The equation makes the role of the depth-law exponent explicit: it controls how quickly losses collapse as flow depth grows from very small values. The text also clarifies which term wins depending on that exponent, reinforcing that the asymptotics are not just formal but practically discriminative.

In short, Eq. (125) is a well-targeted asymptotic that delivers the right physics for shallow flow and dovetails smoothly with the deep-flow ceiling, offering a robust, interpretable hinge for sensitivity and error-propagation analyses.

Half-Saturation Exponential (HSE) model

Predicting the discharge coefficient C_d across shallow and deep regimes usually needs a contraction measure that the user can't observe reliably in the field. HSE avoids that. It uses only the relative upstream flow depth $X = h/b$, as defined by Eq. (79) (upstream flow depth h scaled by a geometry length b), and three interpretable parameters. The result is a bounded, monotone, asymptotically correct curve that's easy to fit and compare across geometries, no contraction coefficient required.

C_d-HSE model

HSE assumes C_d rises smoothly from 0 and approaches a finite ceiling C_∞. The "half-saturation" parameter θ marks the relative flow depth X where C_d reaches exactly half the ceiling, and the shape exponent *m* controls how sharp or gentle the rise is. The C_d-HSE model can reads as follows:

$$C_d(X) = C_\infty \left[1 - 2^{-\left(X/\theta\right)^m}\right] \tag{126}$$

where $m > 0$, $\theta > 0$, and $0 < C\infty \leq 1$. Thus, the "half-saturation" parameter θ corresponds to $X = \theta$, implying the following:

$$C_d = \frac{1}{2} C_\infty \tag{126a}$$

The model does not present any overshoot, or wiggles, since $0 < C_d < C\infty$, and C_d increases strictly with X. In addition, in the HSE model, a Geometry-agnostic ceiling can be observed: $C\infty$ is the large-depth plateau that absorbs unmeasured geometry, edge, and entrance-loss effects, enabling calibration and comparison of $C_d(X)$ using only $X = h/b$, no contraction coefficient required.

The model presents correct limits. As the flows depth grows, i.e., $X \rightarrow \infty$, C_d approaches a finite plateau $C\infty$; when the flow depth is tiny, C_d follows a power law in X, as expected from leading-order flow depth scaling. The following is the authors' explanation:

From writing simplicity, set the following:

$$y = \left(X/\theta\right)^m \tag{127}$$

Then, Eq. (126) can be rewritten as follows:

$$C_d(X) = C_\infty \left(1 - 2^{-y}\right) \tag{126a}$$

which can be re-written as follows:

$$C_d(X) = C_\infty \left(1 - e^{-y \ln 2}\right) \tag{126b}$$

For tiny depth, i.e., $X \ll \theta$, or $y \ll 1$, the following expanding can be written:

$$e^{-y \ln 2} \approx 1 - y \ln 2 + \frac{1}{2}\left(\ln 2\right)^2 y^2 - ... \tag{128}$$

Thus, Eq. (126b) becomes as follows:

$$C_d(X) = C_\infty \left(\ln 2\right)\left(\frac{X}{\theta}\right)^m - \frac{C_\infty}{2}\left(\ln 2\right)^2 \left(\frac{X}{\theta}\right)^{2m} + O((X/\theta)^{3m}) \tag{129}$$

That's a power law in X with exponent m, while the leading order is expressed as follows:

$$C_d(X) \sim C_\infty \left(\ln 2\right)\theta^{-m} X^m \tag{130}$$

The error of the power-law approximation expressed by Eq. (129) can be estimated as follows, writing the next term as:

$$O((X/\theta)^{2m})$$

A handy relative-error estimate is the following:

$$\frac{\text{Error}}{\text{Leading term}} \approx \frac{\frac{1}{2} C_\infty \left(\ln 2\right)^2 y^2}{C_\infty \left(\ln 2\right) y} = \frac{\ln 2}{2} y \tag{131}$$

After calculation, and considering Eq. (127), Eq. (131) reduces to the following:

$$\frac{\text{Error}}{\text{Leading term}} = 0.3466\,(X/\theta)^m \tag{131a}$$

For instance, if $(X/\theta)^m = 0.2$, the power-law expressed by Eq. (129) is within ≈7%.

C_d-HSE model fitting

Three parameters are involved in the C_d-HSE model, namely $C\infty$, θ, and m, which can be estimated from data {hi, bi, C_d,i}, with Xi = hi/bi. In HSE model, $C\infty$ is not governed by a single universal physics law. In HSE, $C\infty$ is the large-depth plateau and is best treated as a fit parameter, per geometry/configuration.

The procedure of estimating the three overmentioned parameters is as follows:

Step 0

For each observation:

- compute Xi = hi/bi.
- Compute C_di from the ratio Q_{Th}/Qexp, where the subscripts "Th" and "Exp" denote "Theoretical" and "Experimental", respectively. Q_{Th} is given by Eq. (3a). Keep points with $0 < C_{d,i} \leq 1$; If any $C_{d,i} > 1$, or $C_{d,i} \leq 0$, cap or discard them.
- Sort the data by ascending Xi. Keep both small X (shallow) and large X (deep) points if available.

Step 1

- Estimate the plateau C∞, from deep points only. Take the deep subset: the top 20–30% largest Xi values, e.g., the largest 20% of Xi.

- Let C∞ be the median of their Cd,i values, i.e., compute the median of the corresponding Cd,i values in that deep subset.; the median is robust to outliers. If that median exceeds 1, set C∞ = 1.
- Thus, set the following:

$$C_{\infty,\,\mathrm{med}} = \min\left\{1,\ \text{median of deep } C_{d,\mathrm{i}}\right\} \tag{132}$$

where the subscript “med” denotes “median”.

Step 2

This section is devoted to the computation of θ_{med} This corresponds to:

$$C_d = \frac{1}{2} C_{\infty,\,\mathrm{med}} \tag{133}$$

This result provides from Eq. (126a), when writing the following:

$$C_d = C_{\infty,\,\mathrm{med}}$$

Thus:

- Compute the following normalized values:

$$Y_{\mathrm{i}} = \frac{C_{d,\mathrm{i}}}{C_{\infty,\,\mathrm{med}}} \tag{134}$$

- Find two consecutive points, in the *X*-sorted data, that straddle 0.5; thus, the following can be written:

$$Y_{\mathrm{i}} \le 0.5 \le Y_{\mathrm{i}+1} \tag{135}$$

Y_i is governed by Eq. (134).

If the users have such a pair, do a linear interpolation in (*X*, *Y*) as follows:

$$\theta_{\mathrm{med}} = X_{\mathrm{i}} + \frac{0.5 - Y_{\mathrm{i}}}{Y_{\mathrm{i}+1} - Y_{\mathrm{i}}}\left(X_{\mathrm{i}+1} - X_{\mathrm{i}}\right) \tag{136}$$

This gives the *X* at which the curve crosses half the plateau.

- If al**l** $Y_i < 0.5$, i.e., there is no deep data, you cannot locate half-saturation reliably; set a provisional θ_{med} to the median of X_i and note the limitation.

- If all $Y_i > 0.5$, i.e., there is no shallow data, set θ_{med} to the smallest X_i with $Y_i \ge 0.5$, i.e., a conservative estimate.

Step 3

This step aims to estimate the shape exponent *m* using shallow points only.

For shallow points, i.e., $X \ll \theta$, and according to Eq. (129), HSE behaves like a power law, as follows:

$$C_d(X) \approx C_{\infty,\mathrm{med}}(\ln 2)\left(\frac{X}{\theta_{\mathrm{med}}}\right)^m \tag{137}$$

Use the points with the following condition, as a shallow subset:

$$Y_{\mathrm{i}} = \frac{C_{d,\mathrm{i}}}{C_{\infty,\mathrm{med}}} \leq 0.3 \tag{138}$$

For each such point, compute; compute the following:

$$m_{\mathrm{i}} = \frac{\ln\left(\dfrac{C_{d,\mathrm{i}}}{C_{\infty,\mathrm{med}}}\right)}{\ln\left(\dfrac{X_{\mathrm{i}}}{\theta_{\mathrm{med}}}\right)} \tag{139}$$

Then take the median of $\{m\mathrm{i}\}$as you estimate the following:

$$m_{\mathrm{med}} = \mathrm{median}\left\{m_{\mathrm{i}}\right\} \tag{140}$$

If you have too few shallow points, e.g., fewer than 3, set the following as a practical default:

$$m_{\mathrm{i,\,med}} = 1 \tag{141}$$

Step 4

This step optional but recommended as a one quick polish of all three parameters. Use your current:

$$\left(C_{\infty,\mathrm{med}}, m_{\mathrm{med}}, \theta_{\mathrm{med}}\right)$$

as starting values and fit them jointly by minimizing the sum of squared differences between observed and model-predicted C_d, as follows:

$$\text{sum of squared errors} = \sum_{\mathrm{i}} \left\{ C_{d,\mathrm{i}} - C_{\infty,\,\mathrm{med}} \left[1 - 2^{-\left(X_{\mathrm{i}}/\theta_{\mathrm{med}} \right)^{m_{\mathrm{med}}}} \right] \right\}^2 \tag{142}$$

with the following bounds:

$0 < C_d \le 1$, $\theta > 0$, $m > 0$

This "polish" adjusts the three following HSE parameters a little so the full curve best matches the data.

$$\left(C_\infty, m, \theta\right)$$

Herein, "Polish" means a short nonlinear least-squares refinement starting from the initial estimate parameters:

$$\left(C_{\infty,\,\mathrm{med}}, m_{\mathrm{med}}, \theta_{\mathrm{med}}\right)$$

The user is required to report the maximum percentage deviation between the predicted and observed values of the involved parameters, especially the discharge coefficient C_d.

Flow-depth elasticity of Cd

(1) Differentiate *Cd* with respect to *X*

In previous sections, such as in Eq. (92), the exact logarithmic sensitivity, i.e., elasticity E_h, of C_d to h, has been define as follows:

$$E_h^{(C_d)} \equiv \frac{\partial \ln C_d}{\partial \ln h} = \frac{h}{C_d}\frac{\partial C_d}{\partial h} \tag{92}$$

Because $X = h/b$ as defined in Eq. (79), the following can be written:

On the other hand, the following can be written, which provides from the definition of elasticity:

$$E_X^{(C_d)} \equiv \frac{\partial \ln C_d}{\partial \ln X} = \frac{X}{C_d}\frac{\partial C_d}{\partial X} \tag{143}$$

Let consider the following chain rule:

$$\frac{\partial \ln C_d}{\partial \ln h} = \frac{\partial \ln C_d}{\partial \ln X}\frac{\partial \ln X}{\partial \ln h} \tag{144}$$

As $X = h/b$, the following can be written:

$$\frac{\partial \ln X}{\partial \ln h} = 1 \tag{145}$$

Thus, Eq. (144) allows writing what follows:

$$E_h^{(C_d)} = E_X^{(C_d)} \tag{146}$$

Let recall the following:

$$y = \left(X / \theta\right)^m \tag{127}$$

Then $C_d(X)$-HSE model given by Eq. (126) reduces to the following:

$$C_d(X) = C_\infty\left(1 - 2^{-y}\right) \tag{126b}$$

Differentiate C_d with regard to X, using the following chain rule:

$$\frac{dC_d}{dX} = C_\infty \frac{d}{dX}\left(1 - 2^{-y}\right) = -C_\infty \frac{d}{dX}\left(2^{-y}\right) \tag{147}$$

Now differentiate 2^{-y}. Write the following:

$$2^{-y} = e^{-y\ln 2} \tag{148}$$

Then, the following can be written:

$$\frac{d}{dX}\left(2^{-y}\right) = \frac{d}{dX}\left(e^{-y\ln 2}\right) \tag{149}$$

The result is the following:

$$\frac{d}{dX}\left(e^{-y\ln 2}\right) = e^{-y\ln 2}\frac{d}{dX}\left(-y\ln 2\right) = 2^{-y}\left(-\ln 2\right)\frac{dy}{dX} \tag{150}$$

Therefore, Eq. (147) becomes as follows:

$$\frac{dC_d}{dX} = -C_\infty \frac{d}{dX}\left[2^{-y}\left(-\ln 2\right)\frac{dy}{dX}\right] = C_\infty\left(\ln 2\right)2^{-y}\frac{dy}{dX} \tag{151}$$

It remains to compute the following:

$$\frac{dy}{dX}$$

From Eq. (127), one may write what follows:

$$y = \left(X / \theta \right)^{m} = \theta^{-m} X^{m} \tag{127a}$$

Then, the following can be written:

$$\frac{dy}{dX} = m\theta^{-m} X^{m-1} = m \frac{X^{m}}{\theta^{m}} \frac{1}{X} \tag{152}$$

Taking into account Eq. (127), Eq. (152) yields the following:

$$\frac{dy}{dX} = m \frac{y}{X} \tag{153}$$

Substituting Eq. (153) into Eq. (151), the following can be written:

$$\frac{dC_d}{dX} = C_\infty \ln\left(2\right) 2^{-y} \left(m \frac{y}{X} \right) \tag{154}$$

The final result can be written in the following form:

$$\frac{dC_d}{dX} = C_\infty m \ln\left(2\right) \frac{y}{X} 2^{-y} \tag{155}$$

(2) Convert to derivative with respect to h

Recall Eq. (79) as follows:

$$X = \frac{h}{b} \tag{79}$$

With b = constant, the following can be written:

$$\frac{\partial X}{\partial h} = \frac{1}{b} \tag{156}$$

Let consider the following chain rule:

$$\frac{\partial C_d}{\partial h} = \frac{\partial C_d}{\partial X} \frac{\partial X}{\partial h} \tag{157}$$

Substituting Eqs. (153) and (156) into Eq. (157), yields the following:

$$\frac{\partial C_d}{\partial h} = \left[C_\infty m \ln\left(2\right) \frac{y}{X} 2^{-y} \right] \frac{1}{b} \tag{158}$$

(3) Form the flow depth-elasticity $E_h^{(C_d)}$

Recall Eq. (92) as follows:

$$E_h^{(C_d)} = \frac{h}{C_d}\frac{\partial C_d}{\partial h} \tag{92}$$

Write Eq. (79) in the following form:

$$h = bX \tag{79a}$$

Recall Eq. (126b) as follows:

$$C_d(X) = C_\infty\left(1-2^{-y}\right) \tag{126b}$$

Substituting Eqs. (158), (79a); and (126b) into Eq. (92), yields the following:

$$E_h^{(C_d)} = \frac{bX}{C_\infty\left(1-2^{-y}\right)}\left[C_\infty\, m\ln\left(2\right)\frac{y}{X}2^{-y}\frac{1}{b}\right] \tag{159}$$

Cancelling C_∞, b, and *X*, Eq. (159) reduces to the following:

$$E_h^{(C_d)} = m\ln\left(2\right)y\frac{2^{-y}}{1-2^{-y}} \tag{160}$$

This is already a correct closed form. Now, it is required to simplify the factor:

$$\frac{2^{-y}}{1-2^{-y}} \tag{161}$$

(4) Algebraic simplification of the above factor

Let us use the following

$$2^{-y} = \frac{1}{2^y} \tag{162}$$

Thus, Eq. (161) can be rewritten as follows:

$$\frac{\frac{1}{2^y}}{1-\frac{1}{2^y}} = \frac{\frac{1}{2^y}}{\frac{2^y-1}{2^y}} = \frac{1}{2^y-1} \tag{163}$$

Substituting the result expressed by Eq. (163) into Eq. (160) yield the following:

$$E_h^{(C_d)} = m \ln(2) \frac{y}{2^y - 1} \tag{164}$$

Using Eq. (127), Eq. (164) can be written in the following final form:

$$E_h^{(C_d)} = E_X^{(C_d)} = m \ln(2) \frac{(X/\theta)^m}{2^{(X/\theta)^m} - 1} \tag{165}$$

This is the explicit expression for the flow depth-elasticity of C_d in the HSE model.

Eq. (165) can be rewritten in the following reduced form:

$$E_h^{(C_d)} = E_X^{(C_d)} = m \ln(2) \frac{y}{2^y - 1}, \quad y = (X/\theta)^m \tag{165a}$$

(5) Limiting checks to verify the formula

- As already stated in step 3, for shallow depth, the following can be written:

$$X << \theta \tag{166}$$

Then, from Eq. (127), one may deduce what follows:

$$y = (X/\theta)^m \to 0 \tag{167}$$

Let use the following:

$$\frac{y}{2^y - 1} = \frac{y}{y \ln 2 + O(y^2)} = \frac{1}{\ln 2} + O(y) \tag{168}$$

Substituting this result into Eq. (164) yields the following:

$$E_h^{(C_d)} \to m \tag{169}$$

Thus, Eq. (169) matches the expected power-law slope.

- For deep flow depth, i.e., $X \to \infty$, the following can be written:

$$X >> \theta \tag{170}$$

Then, from Eq. (127the following can be written:

$$y = (X/\theta)^m \to \infty \tag{171}$$

Consequently, the following is deduced:

2^y dominates

Then

$$\frac{y}{2^y - 1} \to 0 \tag{172}$$

Substituting this result into Eq. (164) yields the following final result:

$$E_h^{(C_d)} \to 0 \tag{173}$$

Thus, both limits agree with the model's physics.

Arctan Saturation (ATS) model

The ATS model gives a clean, bounded description of the discharge coefficient C_d across all regimes, rising smoothly at shallow flow depth and flattening toward a finite ceiling at large flow depth. It uses only the measurable relative flow depth, i.e., $X = h/b$ (flow depth scaled by a chosen geometric length), so you don't need any hard-to-observe contraction metrics. Because the core curve is an arctangent, the model is numerically tame, strictly increasing, and incapable of overshoot or spurious wiggles.

Each parameter has an immediate physical role. The geometry-agnostic ceiling, C-infinity, is the large-flow depth plateau that absorbs unmeasured geometry, edge, and entrance-loss effects. The theta parameter is a half-saturation marker: it is the relative depth at which the coefficient reaches exactly half of that ceiling, giving the user a precise "knee" for design and comparison. This marker is the same than that used in previous C_d-models. The *m* parameter controls curvature, how sharply the curve rises when flow is shallow and how crisply it approaches the plateau as flow depth grows.

Calibration is intentionally simple. First, read the plateau from your deepest measurements (a robust summary like a median works well). Second, locate theta by finding where the data cross half of that plateau; this is a straightforward visual and numerical step. Third, estimate *m* from the shallow-flow depth trend or with a quick straight-line fit after a simple one-step transformation; if data are limited, *m* can be fixed to a reasonable value and refined later. A brief bounded least-squares pass can then polish all three parameters in seconds.

ATS is robust to noise and small datasets. The arctangent core compresses extremes, limiting the leverage of a few very shallow or very deep points; the half-saturation property decouples horizontal positioning (theta) from vertical scaling (C-infinity), improving identifiability; and the shape control (*m*) gives just enough flexibility without introducing fragile curvature knobs. Because the model is framed entirely in relative flow depth, the same procedure transfers cleanly across circular, elliptical, and slot-type openings, only the scaling length you choose for nondimensionalization changes.

In short, ATS delivers a physically credible curve, easy calibration with minimal assumptions, stable behaviour from shallow to deep flow, and parameters that user can interpret at a glance, exactly what the user wants for field use, sensitivity studies, and design documentation.

The C_d-ATS model is defined as follows:

$$C_d(X) = C_\infty \frac{2}{\pi} \arctan\left[\left(\frac{X}{\theta}\right)^m\right] \tag{174}$$

where the shape exponent (dimensionless) is as $m > 0$, the half-saturation relative flow depth (dimensionless) is as $\theta > 0$, and the large-depth plateau (geometry-agnostic ceiling; dimensionless) is as $0 < C\infty \leq 1$. The relative flow depth X is defined by Eq. (79) as $X = h/b$. The "half-saturation" parameter θ corresponds to $X = \theta$, implying the following, knowing that arctan (1) = $\pi/4$:

$$C_d = \frac{1}{2} C_\infty \tag{175}$$

So θ is exactly the relative flow depth where C_d reaches half of its ceiling. This result is the same than that expressed by Eq. (126a) for the previous model, i.e., HSE model.

Let us recall Eq. (127) as follows:

$$y = (X/\theta)^m \tag{127}$$

Then, Eq. (174) can be rewritten as follows:

$$C_d(X) = C_\infty \frac{2}{\pi} \arctan(y) \tag{174a}$$

(a) **Boundedness**

Because:

$$\arctan(y) \in \left]0, \pi/2\right[\text{ for } y > 0 \tag{176}$$

Then, the following can be written:

$$0 < \frac{2}{\pi} \arctan(y) < 1 \tag{177}$$

Consequently, Eq. (174a) yields what follows:

$$C_d(X) < C_\infty \tag{178}$$

(b) **Monotonicity (strictly increasing)**

(b1) Derivative of y with respect to X

Reall Eq. (127a) as follows:

$$y = \left(X/\theta\right)^m = \theta^{-m} X^m \tag{127a}$$

Then, one may write the following:

$$\frac{dy}{dX} = m\theta^{-m} X^{m-1} \tag{179}$$

Takin into account Eq. (127), Eq. (179) becomes as follows:

$$\frac{dy}{dX} = \frac{my}{X} \tag{179a}$$

(b2) Derivative of arctan (y) with respect to X

The following can be written:

$$\frac{d}{dX}\arctan(y) = \frac{1}{1+y^2}\frac{dy}{dX} \tag{180}$$

Inserting Eq. (179a) into Eq. (180) yields the following:

$$\frac{d}{dX}\arctan(y) = \frac{1}{1+y^2}\left(\frac{my}{X}\right) \tag{181}$$

(b3) Chain rule for C_d

From Eq. (174a), the following can be written:

$$\frac{dC_d}{dX} = C_\infty \frac{2}{\pi}\frac{d}{dX}\arctan\left(y\right) \tag{182}$$

Inserting Eq. (181) into Eq. (182) yield what follows:

$$\frac{dC_d}{dX} = C_\infty \frac{2}{\pi}\frac{1}{1+y^2}\left(\frac{my}{X}\right) \tag{183}$$

After rearrangement, Eq. (183) can be written in the following form:

$$\frac{dC_d}{dX} = C_\infty \frac{2m}{\pi}\frac{y}{X\left(1+y^2\right)} \tag{183a}$$

From Eq. (183a), it can be observed that all factors on the right are positive for $y > 0$, as shown in Eq. (127). Thus, one may write what follows:

$$\frac{dC_d}{dX} > 0 \tag{184}$$

This result allows concluding that the discharge coefficient $C_d(X)$ is strictly increasing.

(c) Correct limiting behaviour

(c1) For shallow flow depth, corresponding to $X << \theta$, thus, according to Eq. (127), $y <<$ 1. Hence, one may write the following:

$$\arctan(y) = y + O\left(y^3\right) \tag{185}$$

Thus, Eq. (174a) reduces to the following:

$$C_d\left(X\right) = C_\infty \frac{2}{\pi} y + O\left(y^3\right) \tag{186}$$

Taking into account Eq. (127), Eq. (186) can be rewritten as follows:

$$C_d\left(X\right) = C_\infty \frac{2}{\pi}\left(\frac{X}{\theta}\right)^m + O\left(\left(X/\theta\right)^{3m}\right) \tag{186a}$$

Thus, one may write the leading order power law as follows:

$$C_d \propto X^m \tag{187}$$

(c2) For deep flow depth, corresponding to $X >> \theta$, thus, according to Eq. (127), $y >> 1$. Hence, one may write the following:

$$\arctan(y) \to \pi/2 \tag{188}$$

Then, Eq. (174a) reduces to the following:

$$C_d\left(X\right) \to C_\infty \tag{189}$$

(d) Elasticity (sensitivity) with respect to flow depth

(d1) Elasticity with respect to X

Recall Eq. (143) as follows:

$$E_X^{(C_d)} \equiv \frac{\partial \ln C_d}{\partial \ln X} = \frac{X}{C_d}\frac{\partial C_d}{\partial X} = \frac{X}{C_d}\frac{dC_d}{dX} \tag{143}$$

Recall also Eq. (183a) as follows:

$$\frac{dC_d}{dX} = C_\infty \frac{2m}{\pi} \frac{y}{X\left(1+y^2\right)} \tag{183a}$$

Recall also Eq. (174a) as follows:

$$C_d\left(X\right) = C_\infty \frac{2}{\pi} \arctan\left(y\right) \tag{174a}$$

Inserting Eqs. (183a) and (174a) into Eq. (143) yields the following:

$$E_X^{(C_d)} = \frac{X}{C_\infty \frac{2}{\pi} \arctan\left(y\right)} C_\infty \frac{2m}{\pi} \frac{y}{X\left(1+y^2\right)} \tag{190}$$

After simplification and rearrangement, Eq. (190) gives the elasticity of C_d with respect to X as follows:

$$E_X^{(C_d)} = \frac{m\,y}{\left(1+y^2\right)\arctan\left(y\right)}, \qquad y = \left(X/\theta\right)^m \tag{190a}$$

Furthermore, one may check the following:

d1-1) For shallow limit, corresponding to $X << \theta$, thus, according to Eq. (127), $y << 1$, and considering Eq. (185), Eq. (190a) allows writing what follows:

$$E_X^{(C_d)} \to m \tag{191}$$

This result agrees with the leading-order power law.

d1-2) For the half-saturation, corresponding to $X = \theta$, Eq. (190a) allows writing the following:

$$y \to 1 \tag{192}$$

Inserting Eq. (192) into Eq. (190) yields the following relationship of the elasticity of C_d with respect to X, for the half-saturation:

$$E_X^{(C_d)} = \frac{m \times 1}{\left(1+1\right)\times\left(\pi/4\right)} \tag{193}$$

Or

$$E_X^{(C_d)} = \frac{2m}{\pi} \tag{193a}$$

d1-3) For the deep limit, corresponding to one may write that $X >> \theta$; thus, according to Eq. (127), $y >> 1$, i.e., $y \to \infty$. Hence, one may write the following:

$$\lim_{y \to \infty} \frac{y}{\left(1+y^2\right)} = \lim_{y \to \infty} \frac{1}{y\left(1+\frac{1}{y^2}\right)} = 0 \tag{194}$$

Thus, Eq. (190a) allows writing what follows:

$$E_X^{(C_d)} \to 0 \tag{195}$$

(d2) Monotonic decrease of $E_X^{(C_d)}$

Let us adopt the following:

$$G\left(y\right) = \frac{y}{\left(1+y^2\right)\arctan\left(y\right)} \tag{196}$$

Substituting Eq. (196) into Eq. (190a) yields what following:

$$E_X^{(C_d)} = m\,G\left(y\right) \tag{190b}$$

In addition, let us denote the denominator of Eq. (196) as follows:

$$\mathrm{B}\left(y\right) = \left(1+y^2\right)\arctan\left(y\right) \tag{197}$$

This allows writing the following:

$$\frac{d}{d\,y}\mathrm{B}\left(y\right) = 2\,y\arctan\left(y\right)+1 \tag{198}$$

On the other hand, let's denote the numerator of Eq. (196) as follows:

$$\mathrm{A}\left(y\right) = y \tag{199}$$

Thus, the following can be written:

$$\frac{d}{d\,y}\mathrm{A}\left(y\right) = 1 \tag{200}$$

Let us adopt the following quotient rule:

$$\frac{d}{dy}G(y)=\frac{\mathrm{B}\dfrac{d\mathrm{A}}{dy}-\mathrm{A}\dfrac{d\mathrm{B}}{dy}}{\mathrm{B}^2} \tag{201}$$

Substituting Eqs. (197), (195), (199), and (200) into Eq. (201) yields the following:

$$\frac{d}{dy}G(y)=\frac{\left(1+y^2\right)\arctan(y)-y\left[2y\arctan(y)+1\right]}{\left[\left(1+y^2\right)\arctan(y)\right]^2} \tag{202}$$

The sign of the above derivative is the sign of the numerator, since the sign of the denominator is positive. Denoting N(y) the numerator of Eq. (202), the following can be deduced:

$$\mathrm{N}(y)=\left(1-y^2\right)\arctan(y)-y \tag{203}$$

For all $y > 0$, computation shows the following:

$$\mathrm{N}(y)<0 \tag{204}$$

(d2-1) If:

$$0<y\le 1 \tag{205}$$

and since:

$$\arctan(y)\le y \tag{206}$$

and

$$1-y^2\ge 0 \tag{207}$$

Thus, the following result can be written:

$$\mathrm{N}(y)\le\left(1-y^2\right)y-y=-y^3<0 \tag{208}$$

(d2-2) If:

$$y\ge 1 \tag{209}$$

Then, the following can be written:

$$1-y^2\le 0 \tag{210}$$

and

$$\arctan\left(y\right) > 0 \tag{211}$$

These allow writing the following:

$$\left(1-y^2\right)\arctan\left(y\right) \le 0 \tag{212}$$

Thus, Eq. (203) allow deducing the following:

$$\mathrm{N}\left(y\right) \le 0 - y = -y < 0 \tag{213}$$

Therefore, for all $y > 0$ and from Eqs. (202) and (203), the following can be written:

$$\frac{d}{dy}G\left(y\right) < 0 \tag{214}$$

Thus, according to Eqs. (190b) and (214), the following can be written:

$$\frac{d}{dy}E_X^{(C_d)} = m\frac{d}{dy}G\left(y\right) < 0 \tag{215}$$

Thus

$$\frac{d}{dy}E_X^{(C_d)} < 0 \tag{215a}$$

Since $y(X)$ is strictly increasing in X according to Eq. (127), Eq. (215a) implies that $E_X^{(C_d)}$ is strictly decreasing in X.

(d3) Elasticity with respect to the flow depth h and equality $E_h^{(C_d)} = E_X^{(C_d)}$

By definition [Eq. (92)], we know the following:

$$E_h^{(C_d)} = \frac{\partial \ln C_d}{\partial \ln h} = \frac{h}{C_d}\frac{\partial C_d}{\partial h} \tag{92}$$

Recall Eq. (156) as follows:

$$\frac{\partial X}{\partial h} = \frac{1}{b} \tag{156}$$

Let's adopt the following chain rule:

$$\frac{\partial C_d}{\partial h} = \frac{\partial C_d}{\partial X}\frac{\partial X}{\partial h} \tag{216}$$

Substituting Eq. (156) into Eq. (216) yield the following:

$$\frac{\partial C_d}{\partial h} = \frac{1}{b}\frac{\partial C_d}{\partial X} \tag{217}$$

Thus, Eq. (92) gives the following:

$$E_h^{(C_d)} = \frac{h}{C_d}\frac{1}{b}\frac{\partial C_d}{\partial X} = \frac{bX}{C_d}\frac{1}{b}\frac{\partial C_d}{\partial X} = \frac{X}{C_d}\frac{\partial C_d}{\partial X} = E_X^{(C_d)}$$

Finally, the following result is obtained:

$$E_h^{(C_d)} = E_X^{(C_d)} \tag{218}$$

Substituting Eq. (190a) into Eq. (218), the following result is derived:

$$E_h^{(C_d)} = E_X^{(C_d)} = \frac{m\,y}{\left(1+y^2\right)\arctan\left(y\right)}, \quad y = \left(X/\theta\right)^m \tag{219}$$

For rigid geometry, Eq. (219) holds exactly.

d4) Parameter elasticities (sensitivities to $C\infty$, θ, m)

d4-1) Elasticity to $C\infty$

For any parameter p, one may define the following:

$$E_p^{(C_d)} = \frac{\partial \ln C_d}{\partial \ln p} = \frac{p}{C_d}\frac{\partial C_d}{\partial p} \tag{220}$$

Since C_d is linear in $C\infty$, Eq. (174a) allows writing the following:

$$\frac{\partial C_d}{\partial C_\infty} = \frac{2}{\pi}\arctan\left(y\right) \tag{221}$$

On the other hand, Eq. (220) gives the following:

$$E_{C_\infty}^{(C_d)} = \frac{C_\infty}{C_d}\frac{\partial C_d}{\partial C_\infty} \tag{222}$$

Substituting Eqs. (174a) and (221) into Eq. (222) yields the following:

$$E_{C_\infty}^{(C_d)} = \frac{C_\infty}{C_\infty \dfrac{2}{\pi}\arctan(y)} \frac{2}{\pi}\arctan(y)$$

After simplification, the final result is as follows:

$$E_{C_\infty}^{(C_d)} = 1, \quad \text{everywhere} \tag{223}$$

« Everywhere » means at every flow depth.

Thus, 1% error in C_∞ produces the same error in C_d.

d4-2) Elasticity to θ

Let's recall Eq. (174) as follows:

$$C_d(X) = C_\infty \frac{2}{\pi}\arctan\left[\left(\frac{X}{\theta}\right)^m\right] \tag{174}$$

This allows to derive the following:

$$\frac{\partial C_d}{\partial \theta} = -C_\infty \frac{2}{\pi} m X^m \frac{\theta^{m-1}}{\theta^{2m} + X^{2m}} \tag{224}$$

On the other hand, from Eq. (127a), the following can be written:

$$X^m = y\theta^m \tag{127b}$$

Substituting Eq. (127b) into Eq. (224), while simplifying and rearranging, results in the following:

$$\frac{\partial C_d}{\partial \theta} = -C_\infty \frac{2}{\pi} \frac{m y}{\theta\left(1 + y^2\right)} \tag{225}$$

From the definition expressed by Eq. (220), the following can be written:

$$E_\theta^{(C_d)} = \frac{\theta}{C_d} \frac{\partial C_d}{\partial \theta} \tag{220a}$$

Substituting Eq. (225) into Eq. (220a) results in the following:

$$E_{\theta}^{(C_d)}=\frac{\theta}{C_d}\left[-C_{\infty}\frac{2}{\pi}\frac{m\,y}{\theta\left(1+y^2\right)}\right] \tag{226}$$

Recall Eq. (174a) as follows:

$$C_d\left(X\right)=C_{\infty}\frac{2}{\pi}\arctan\left(y\right) \tag{174a}$$

Inserting Eq. (174a) into Eq. (226), and simplifying, yields the following final result:

$$E_{\theta}^{(C_d)}=-\frac{m\,y}{\left(1+y^2\right)\arctan\left(y\right)} \tag{227}$$

Taking into account Eqs. (219) and (227), yields what follows:

$$E_{h}^{(C_d)}=E_{X}^{(C_d)}=-E_{\theta}^{(C_d)} \tag{228}$$

d4-3) Elasticity to *m*

Recall Eq. (174) as follows:

$$C_d\left(X\right)=C_{\infty}\frac{2}{\pi}\arctan\left[\left(\frac{X}{\theta}\right)^{m}\right] \tag{174}$$

This allows deriving the following:

$$\frac{\partial C_d}{\partial m}=\frac{C_{\infty}\frac{2}{\pi}\left(X/\theta\right)^{m}\ln\left(X/\theta\right)}{1+\left(X/\theta\right)^{2m}} \tag{229}$$

Recall Eq. (127) as follows:

$$y=\left(X/\theta\right)^{m} \tag{127}$$

Then, substituting Eq. (127) into Eq. (229), this reduces to the following:

$$\frac{\partial C_d}{\partial m}=C_{\infty}\frac{2}{\pi}\left(\frac{y}{1+y^2}\right)\ln\left(X/\theta\right) \tag{230}$$

According to Eq. (220), the following can be written:

$$E_m^{(C_d)} = \frac{m}{C_d}\frac{\partial C_d}{\partial m} \tag{231}$$

On the other hand, let's recall Eq. (174a) as follows:

$$C_d\left(X\right) = C_\infty \frac{2}{\pi}\arctan\left(y\right) \tag{174a}$$

Substituting Eqs. (230), and (174a) into Eq. (231) yield what follows:

$$E_m^{(C_d)} = \frac{m}{C_\infty \dfrac{2}{\pi}\arctan\left(y\right)} C_\infty \frac{2}{\pi}\left(\frac{y}{1+y^2}\right)\ln\left(X/\theta\right)$$

After simplification, the following final result is obtained:

$$E_m^{(C_d)} = m\left(\frac{y}{1+y^2}\right)\frac{\ln\left(X/\theta\right)}{\arctan\left(y\right)} \tag{232}$$

Let's recall Eq. (190a) as follows:

$$E_X^{(C_d)} = \frac{m\,y}{\left(1+y^2\right)\arctan\left(y\right)}, \qquad y = \left(X/\theta\right)^m \tag{190a}$$

Comparing between Eqs (190a) and (232) yields the following:

$$E_m^{(C_d)} = E_X^{(C_d)}\ln\left(X/\theta\right) \tag{233}$$

The following implications can be pointed out:

At $X = \theta$ the od C_d to m elasticity is zero; it is negative for $X < \theta$ and positive for $X > \theta$. The knee carries minimal information about m; shallow/deep tails inform m.

d5) From C_d to total discharge sensitivity

If the measured flow is modelled as $Q = C_d(X) \times Q_{Th}$,, with Q_{Th} the theoretical/loss-free discharge for the considering geometry, the flow depth-elasticity of total flow splits additively as follows:

$$E_h^{(Q)} = E_h^{(C_d)} + E_h^{(Q_{Th})} \tag{234}$$

d6) Calibration procedure

What is given is: (1) the data $\{h\text{i}, b\text{i}, Q\text{i}\}$, and (2) a given weir geometry. Compute observed C_d,i, then fit ($C\infty$, θ , m) following these steps:

d6-1) Step 0 – Build (Xi, C_d,i)

- Compute the relative flow depth Xi = hi/b, valid for the three weirs geometries considered in the present monograph:

- Compute the observed Cd,i = Qi / Q_{Th} (hi), with Q_{Th} (hi) provided from the exact loss-free formula for the geometry. Keep $0 < C_d,\text{i} \leq 1$.

d6-2) Step 1: Plateau $C\infty$ from deep points

Sort by Xi. Take the top 20–30% largest Xi and set. Then, consider the median value of $C\infty$, i.e., $C\infty$, med as follows:

$$C_{\infty,\,\text{med}} = \min\left\{ 1, \text{ median of deep } C_{d,\text{i}} \text{ in that deep subset} \right\} \tag{235}$$

Median is robust; "min with 1" enforces the physical bound.

d6-3) Step 2: Linearization to get θ and m

Normalize Ci = C_d,i / C∞, med. Keep points with 0 < Ci < 1. Using Eq. (174), provide the following identity:

$$\tan\left(\frac{\pi}{2} C\text{i}\right) = \left(\frac{X\text{i}}{\theta}\right)^m \tag{174b}$$

Take natural logs on both sides of Eq. (174b) and present the final result as follows:

$$\ln\tan\left(\frac{\pi}{2} C\text{i}\right) = m \ln X\text{i} - m \ln(\theta) \tag{174c}$$

This is a straight line in ln$X$i. Fit by least squares to get: (1) the slope m_{med} ; (2) intercept $\kappa_{\text{med}} = -m \ln(\theta)$ and provide the following:

$$\theta_{\text{med}} = \exp\left(-\kappa_{\text{med}} / m_{\text{med}}\right) \tag{236}$$

d6-4) Step 3: Optional short polish (joint fit)

Use the following as starting values:

$$\left(C_{\infty,\,\text{med}}; \theta_{\text{med}}; m_{\text{med}}\right)$$

The, minimize the sum of squared errors (SSE) in the original model, as follows:

$$\text{sum of squared errors} = \sum_{\mathrm{i}} \left[C_{d,\mathrm{i}} - C_{\infty,\,\mathrm{med}} \arctan\left(X_{\mathrm{i}} / \theta_{\mathrm{med}} \right)^{m_{\mathrm{med}}} \right]^2 \tag{237}$$

With the following bounds:

$$0 < C_{\infty} \le 1,\ \theta > 0,\ m > 0$$

A few iterations, e.g., Levenberg–Marquardt, typically "polish" the parameters.

d6-5) Step 4: Sanity checks

d6-5-1) For the half-saturation, the data points where the following:

$$C_{d,\,\mathrm{i}} \approx \frac{1}{2} C_{\infty,\,\mathrm{med}}$$

should lie nearby:

$$X\mathrm{i} \approx \theta_{\mathrm{med}}$$

d6-5-2) Shallow slope: on a log–log plot of C_d vs X, the initial slope should be near m median.

d6-5-3) Plateau: at the largest Xi, the fitted curve should flatten near $C\infty$ median.

d6-6) Notes for stability

Discard points with Ci extremely close to 0 or 1, e.g., $C\mathrm{i} < 0.02$ or $C\mathrm{i} > 0.98$; to avoid numerical blow-ups in tan ($\pi/2 \times C$i).
If data are scarce in the shallow tail, you may temporarily fix $m = 1$ in this step and refine later.

d7) Dominant knobs by regime

d7-1) For a shallow regime, m (slope) and θ (horizontal shift) dominate. For $X << \theta$, the arctangent in $C_d(X)$ formulation, [Eq. (174)], behaves like its argument. Precisely as follows:

$$C_d\left(X\right) \approx C_{\infty} \frac{2}{\pi} \left(\frac{X}{\theta} \right)^m \tag{238}$$

Thus, on a log–log plot of C_d vs X, the initial slope is m; larger m = steeper take-off, while; smaller m = gentler take-off.

d7-2) For a deep regime (large X), $C\infty$ (vertical scale) dominates. What "vertical scale" means herein:

The parameter $C\infty$ sets the overall height of the entire C_d curve on a plot of C_d (vertical axis) versus relative flow depth $X = h/b$ (horizontal axis). If you multiply $C\infty$ by any factor, every predicted C_d value is multiplied by the same factor. The curve is stretched (or compressed) up or down without changing its horizontal position or its shape. In both HSE and ATS models, C_d (X) is written as follows:

$$C_d\left(X\right) = C_\infty \times \text{dimensionless shape that depends on } X,\ \theta, \text{ and } m$$

That front factor $C\infty$ scales the vertical axis only.

For $X >> \theta$, or $y \rightarrow\infty$, the arctan in Eq. (174) approached π/2 from the following:

$$\text{arctang}\left(y\right) = \frac{\pi}{2} - \frac{1}{y} + o\left(\frac{1}{y}\right) \quad y \rightarrow \infty \tag{239}$$

With:

$$y = \left(X / \theta\right)^m \tag{127}$$

the gap to the ceiling is as follows:

$$C_\infty - C_d(X) \approx C_\infty \frac{2}{\pi} \frac{1}{\left(X/\theta\right)^m} = \underbrace{C_\infty \frac{2}{\pi}}_{\text{constant}} \left(\frac{\theta}{X}\right)^m \tag{240}$$

Thus, the tail decays to the plateau like a power m of θ/X.

d8) Identifiability: θ is pinned by the exact half-saturation, m by tail (very small X) curvature, and $C\infty$ by deep data. The parameter m governs how sharply the curve peels away from 0 when shallow and how fast it approaches its ceiling when deep.

Residual-Difference Pyramid (RDP) model

The C_d-RDP model is built to give practitioners a clean, bounded, and strictly increasing description of the discharge coefficient across all regimes, without asking for anything that is hard to measure in the field. It stays within your established similarity controls, so it drops naturally into the same plots, diagnostics, and workflows you already use. Like ATS, the emphasis is on numerical stability, physical credibility, and day-one interpretability rather than curve-gymnastics: the model rises briskly when the flow is shallow, then settles smoothly into a finite, geometry-aware plateau as depth grows.

What is new in RDP is how it explains the journey to the plateau. Instead of forcing one universal shape, RDP views the approach to the ceiling as the fading of two simple "loss channels." One governs the very shallow take-off; the other shapes the mid-range. Their influence shrinks with depth, so the model cannot overshoot and cannot wiggle; it simply climbs and levels out. This two-timescale view gives you just enough curvature to capture real-world behaviour, especially when edges, entrances, or mild secondary effects are present, without burdening the fit with fragile knobs.

Each parameter plays an immediate, observable role. The plateau sets the overall vertical scale; the two exponents govern how sharply the curve peels away from zero and how decisively it locks onto the ceiling; the mixing weight trades emphasis between those regimes. Because these roles are orthogonal, identifiability is strong: deep points pin the plateau; the shallow trend informs the take-off; the mid-range balances the mix. The result is a model you can read off a plot and defend in a design review.

Calibration follows the same plateau-first, shape-second rhythm you already use. Read the large-depth plateau from your deepest measurements, then fit the two-channel shape on the full dataset, and, if desired, run a short bounded least-squares polish. This keeps the workflow fast, transparent, and robust on small or noisy datasets, precisely the virtues that made ATS model attractive in practice.

Finally, Cd-RDP is deliberately portable. Because it is framed in the same nondimensional controls as the existing weir families, it transfers cleanly across circular, elliptical, and slot-type openings with only the scaling length and the fitted parameters changing. In short, RDP model gives the user the same trustable backbone as ATS, boundedness, monotonicity, and easy calibration, while adding a realistic, two-timescale pathway to the ceiling that often sharpens fit quality without sacrificing simplicity.

C_d-RDP model

Positioning within our established framework

The dimensional analysis and reduction isolate two similarity controls for the discharge coefficient C_d: the relative flow depth $X \equiv h/b$ and the compound contraction index Γ. These appear as Eqs. (79) and (77), respectively, and the dimensionless lateral contraction of the three considered geometries, $k \equiv 2b/B$, appears in Eq. (89). In regimes where viscosity and capillarity are negligible, i.e., large Reynolds and Weber/Bond numbers, C_d is modelled as a function of X and Γ [cf. Eqs. (76) – (80)]. In what follows, we keep exactly these controls, and we reuse the standard elasticity with respect to h, Eq. (92), as the vehicle for sensitivity/uncertainty analysis, together with the closed form of Eq. (90).

Model definition (RDP core)

The RDP core models the losses as a two-level residual pyramid, two simple, saturating deficits that decay with flow depth, bounded by a contraction-controlled ceiling, as follows:

$$C_d\left(X,\Gamma\right)=C_\infty\left(\Gamma\right)\left(1-\frac{\gamma}{1+X^{m_1}}-\frac{1-\gamma}{1+X^{m_2}}\right) \tag{241}$$

with the parameters such as follows:

$$m_1 > 0, m_2 > 0, \gamma \in \,]0, 1[\tag{242}$$

The two fractions in Eq. (241) act as near-field and mid-field deficits. Their convex weights γ and $(1 - \gamma)$ sum to 1, so the parenthesis transitions cleanly from 0 at $X = 0$ to 1 at $X \to \infty$.

The ceiling is the same light-weight quadratic we already used [Eq. (82)]; it reads as follows:

$$C_\infty(\Gamma) = c_0 + c_1\Gamma + c_2\Gamma^2, \;\; 0 < C_\infty(\Gamma) < 1 \tag{82}$$

with our usual mild constraints, defined as follows:

$$c_1 > 0, \; c_1 + 2c_2 > 0$$

$$0 < c_0 < c_0 + c_1 + c_2 < 1 \tag{84}$$

Physical consistent properties

(a) The RDP- model present bounds everywhere. Since the term in the parenthesis of Eq. (241) lies in the range]0, 1[, the following can be written:

$$0 < C_d(X, \Gamma) < C_\infty(\Gamma) < 1 \tag{243}$$

(b) The RDP-model is monotone in X, so that the following can be written:

$$\frac{dC_d}{dX} = C_\infty(\Gamma) \sum_{j=1}^{2} \omega_j \frac{m_j X^{m_j - 1}}{\left(1 + X^{m_j}\right)^2} > 0, \;\; X > 0 \tag{244}$$

with:

$\omega_1 = \gamma$, and $\omega_2 = 1 - \gamma$

Eq. (244) is written as follows:

$$\frac{dC_d}{dX} = C_\infty(\Gamma) \left[\gamma \frac{m_1 X^{m_1 - 1}}{\left(1 + X^{m_1}\right)^2} + (1-\gamma) \frac{m_2 X^{m_2 - 1}}{\left(1 + X^{m_2}\right)^2} \right] \tag{244a}$$

(c) Correct asymptotes

For small flow depths, i.e., $X << 1$, one may write the following:

$$C_d \approx C_\infty \left[\gamma X^{m_1} + (1-\gamma) X^{m_2} \right] \quad (245)$$

(d) For large flow depths, i.e., $X >> 1$, the following can be derived:

$$C_d \approx C_\infty \left[1 - \gamma X^{-m_1} - (1-\gamma) X^{-m_2} \right] \quad (246)$$

This corresponds to "One-Minus" with two decaying deficits, mirroring the "One-Minus" principle used in AOM model.

(d) Optional J-level extension

$$C_d(\Gamma) = C_\infty(\Gamma) \left(1 - \sum_{j=1}^{j} \frac{\omega_j}{1 + X^{m_j}} \right) \quad (247)$$

with

$$\omega_j \geq 0, \ \sum_j \omega_j = 1 \quad (248)$$

Flow-depth elasticity **(for uncertainty propagation)**

One may use the same decomposition as in the previous sections: the logarithmic sensitivity of C_d to h splits into a direct depth part E and a contraction pathway N [Eqs (93) and (95)].

Indeed, for RDP model, Eq. (241), the following can be written:

$$C_d(X, \Gamma) = C_\infty S(X) \quad (241a)$$

in which $S(X)$ is the term in the parenthesis of Eq. (241), independent of Γ; this is the base of RDP. Applied the following chain rule for Eq. (92):

$$\ln C_d = \ln C_\infty(\Gamma) + \ln S(X) \quad (249)$$

Knowing, by definition, that:

$$E_h^{(C_d)} = \frac{\partial \ln C_d}{\partial \ln h} = \underbrace{\frac{\partial \ln S}{\partial \ln X} \frac{\partial \ln X}{\partial \ln h}}_{\mathrm{E}(X)} + \underbrace{\frac{\partial \ln C_\infty}{\partial \Gamma} \frac{d\Gamma}{d \ln h}}_{\mathrm{N}(\Gamma)} \quad (250)$$

with the general form and notation as in Eq. (92), and with the same derivative of Γ with respect to h, according to Eq. (90), and with same parameter k expressed by Eq. (89). Below, we provide $\mathrm{E}(X)$ and $\mathrm{N}(\Gamma)$ for the RDP-model.

(a) Direct flow depth term $\mathrm{E}(X)$

Because $X = h/b$ as expressed by Eq. (79), the following can be derived:

$$\mathrm{E}_X^{(C_d)} = \frac{X}{C_d}\frac{\partial C_d}{\partial X} = \frac{\sum_{j=1}^{2} \omega_j \dfrac{m_j X^{m_j}}{\left(1+X^{m_j}\right)^2}}{1-\sum_{j=1}^{2} \dfrac{\omega_j}{1+X^{m_j}}},\ \omega_1 = \gamma,\ \omega_2 = 1-\gamma \tag{251}$$

In Eq. (251), E(X) it is the *direct* contribution through $X = h/b$ alone.

Eq. (251) can be rewritten in the following form:

$$\mathrm{E}_X^{(C_d)} = \frac{\gamma \dfrac{m_1 X^{m_1}}{\left(1+X^{m_1}\right)^2} + (1-\gamma)\dfrac{m_2 X^{m_2}}{\left(1+X^{m_2}\right)^2}}{1-\dfrac{\gamma}{1+X^{m_1}}-\dfrac{1-\gamma}{1+X^{m_2}}} \tag{252}$$

with $X = h/b, m_1, m_2 > 0, 0 < \gamma < 1$

On the other side, one may provide the following behaviour:

$$\mathrm{E}_X^{(C_d)} \sim \gamma m_1 + (1-\gamma) m_2 \text{ as } X \to 0 \tag{253}$$

and

$$\mathrm{E}_X^{(C_d)} \to 0 \text{ as } X \to \infty \tag{254}$$

Thus, RDP rises briskly when shallow and flattens when deep, our standard qualitative envelope.

(b) Contraction pathway N(Γ)

Since the term in parenthesis of Eq. (241) does not depend on Γ (base RDP), only the ceiling contributes. According to Eq. (250), the following can be written:

$$\mathrm{N}_\Gamma^{(C_d)} = \frac{\partial \ln C_\infty}{\partial \Gamma}\frac{d\Gamma}{d\ln h} = \frac{C_\infty'}{C_\infty}\Gamma\left(1-\frac{\Gamma}{k}\right) \tag{255}$$

C_∞' is given by Eq. (97) as follows:

$$C_{\infty}^{'}(\Gamma) = c_1 + c_2\Gamma\,,\; C_{\infty}^{'}(\Gamma) > 0\,,\;\; c_1 > 0,\, c_1 + 2c_2 > 0 \tag{97}$$

Thus, the following can be written:

$$\mathrm{N}_{\Gamma}^{(C_d)} \geq 0 \tag{256}$$

Moreover, as $h \to \infty$, $\Gamma \to k$ according to Eq. (77), and, thus, $\mathrm{N} \to 0$, according to Eq. (255), confirming the plateau.

In short, regarding elasticity, the following can be written:

$$E_h = \mathrm{E} + \mathrm{N} \geq 0 \tag{257}$$

with E dominant when $X << 1$, and N fading as $\Gamma \to k$ (deep regime). This is the same split and behaviour the authors documented for AOM/RPS/BPS/ATS.

Calibration procedure

Step 0

Build predictors/response. From $\{h\mathrm{i}, b\mathrm{i}, B\mathrm{i}, P\mathrm{i}, Q\mathrm{i}\}$, form $X\mathrm{i} = h\mathrm{i}/b\mathrm{i}$ [Eq. (79)], and $\Gamma\mathrm{i} = (2b\mathrm{i}/B\mathrm{i}) / (1 + P\mathrm{i}/h\mathrm{i})$ [Eq. (77)]. Compute observed $C_d,\mathrm{i} = Q\mathrm{i} / Q_{Th}\,(h\mathrm{i})$. Keep $0 < C_d,\mathrm{i} \leq 1$.

Step 1

Ceiling vs. contraction. Fit $C\infty(\Gamma) = c_0 + c_1\Gamma + c_2\Gamma^2$ [Eq. (82)] on the deep subset (top 20 to 30% Xi), enforcing Eqs. (84) and (86 so $0 < C\infty < 1$. This mirrors the AOM/BPS procedure of "reading the plateau" first.

Step 2

Depth-loss shape. With C∞ fixed, form the following:

$$C\mathrm{i} = \frac{C_{d,\mathrm{i}}}{C_{\infty}} \approx 1 - \frac{\gamma}{1 + X_{\mathrm{i}}^{m\,1}} - \frac{1-\gamma}{1 + X_{\mathrm{i}}^{m\,2}}$$

Search m_1, $m_2 \in [0.6, 2.5]$ on a coarse grid; for each pair, compute the bounded least-squares estimate of $\gamma \in [0, 1]$; the model is linear in γ given m_1, m_2. Pick the triplet minimizing SSE.

Step 3

Optional joint polish. Starting from Step 1–2, jointly refine c_0, c_1, c_2, m_1, m_2, and γ by constrained nonlinear least squares, with respect Eq. (84), $m_{1,2} > 0$, and $\gamma \in [0, 1]$. Report R^2 and max/mean relative errors, as in the other models.

Hill Saturation (HIS) model

The Hill Saturation (HIS) model, also known as the generalized Michaelis–Menten model, i.e., an extension of the classical Michaelis–Menten kinetics, extends the paper's semi-empirical framework for predicting the discharge coefficient C_d in sharp-crested meters by keeping the same two similarity controls, relative flow-depth and contraction, while offering a steeper, cooperative-like transition from shallow to deep regimes. Within this framework the behaviour is governed primarily by a dimensionless relative flow-depth and a compound contraction index; each proposed family is built to be bounded, monotone, and asymptotically correct, plateauing at a contraction-limited ceiling.

HIS uses a Hill-type saturation curve in the relative depth variable $X = h/b$, as defined in Eq. (79), to model how C_d rises from near zero at very small depths to a finite plateau as depth increases. The Hill construction preserves the key "half-saturation" landmark, there exists a $\theta > 0$ such that C_d reaches exactly half of its ceiling at $X = \theta$, and introduces a single shape (Hill) exponent that controls how abruptly the curve turns upward. In short: shallow regime → power-law in X; deep regime → finite ceiling.

As in the other families, HIS separates "how high" the curve can go from "how fast" it gets there. The large-depth plateau is handled by a geometry-agnostic ceiling $C\infty \leq 1$. When a contraction descriptor is available, the same quadratic ceiling used elsewhere, $C\infty(\Gamma) = c_0 + c_1\Gamma + c_2\Gamma^2$ as defined by Eq. (82), can be plugged in directly; when it isn't, $C\infty$ can be read from deep data as a single fit parameter.

HIS is deliberately compatible with the paper's design principles. Like HSE, it locates a clear knee at $X = \theta$, which is the "half-saturation" point, but HIS replaces HSE's exponential rise with a cooperative Hill rise that can be either gentler or sharper depending on the Hill exponent, giving users a tunable transition without sacrificing boundedness or monotonicity. The limiting behaviour mirrors the established envelope: a power-law onset at small X and a horizontal approach to $C\infty$ at large X.

The HIS parameters are estimated exactly as in the half-saturation families already in the paper: (1) read the deep-flow plateau from the largest 20–30% of X values (a robust median works well), yielding $C\infty$; (2) locate θ where the data cross half the plateau; (3) infer the shape exponent from the shallow-depth trend and then refine all parameters with a bounded least-squares pass.

As with other families, a closed-form flow-depth elasticity follows from the same master definition [Eq. (92)], revealing the same clean split between a direct depth term and a contraction pathway when a Γ-aware ceiling is used, depth effects dominate when $X \ll 1$, while contraction fades as the curve saturates. This gives HIS model the same uncertainty-propagation and sensitivity advantages already developed in the present monograph.

Practically, HIS is a one-equation, three-parameter surface since C_d depends on X, $C\infty$, θ, and shape, that (1) honours the monograph's physics and asymptotics, (2) remains interpretable at a glance, i.e., ceiling, knee, and steepness, (3) is easy to calibrate with sparse, noisy field data, and (4) nests naturally within the same contraction-aware ceiling that authors already use. It gives the practitioner a compact curve that rises briskly when shallow, flattens when deep, never overshoots, and exposes the parameters that matter for design and comparison.

C_d-HIS model

The Hill (generalized Michaelis–Menten) saturation gives a bounded, strictly increasing, half-saturating curve with an exact power-law take-off and a power-law tail to the ceiling. It stays within the X–Γ framework and slots directly into your (E + N) elasticity split [Eqs. (90), and (250)].

Definition and admissible parameterization

The core form of the C_d-HIS model can be written as follows:

$$C_d\left(X,\Gamma\right)=C_\infty(\Gamma)\frac{\left(X/\theta\right)^m}{\left(X/\theta\right)^m+\theta\left(\Gamma\right)^m}\quad m>0 \tag{258}$$

It is worth noting that the term $(X/\theta)^m$ in Eq. (258) corresponds to y in Eq. (127), according to the notation adopted by the authors.

Eq. (258) can be rewritten in the following reduced form:

$$C_d\left(X,\Gamma\right)=C_\infty(\Gamma)\,S\left(X,\theta,m\right) \tag{258a}$$

where

$$S\left(X,\theta,m\right)=\frac{\left(X/\theta\right)^m}{\left(X/\theta\right)^m+\theta\left(\Gamma\right)^m} \tag{S-1}$$

In Eq. (258), $C\infty(\Gamma)$ is the standard ceiling expressed by Eq. (82) with constraints expressed by Eq. (84). $\theta(\Gamma)$ locates the knee, i.e., half-saturation as defined by Eq. (174), which recalled as follows:

$$C_d=\frac{1}{2}C_\infty \tag{174}$$

A simple and monotone θ–Γ linkage that shifts the knee earlier as contraction weakens ($\Gamma\uparrow$) is as follows:

$$\theta\left(\Gamma\right)=\theta_0\left[1+q\left(1-\frac{\Gamma}{k}\right)\right],\ \theta_0>0,\ q\geq 0 \tag{259}$$

with $k = 2b/B$ expressed by Eq. (89).

Setting q = 0, Eq. (259) reduces to a geometry-agnostic knee, exactly like HSE/ATS models.

Bounds and monotonicity

Given the following:

$$0 < \frac{\left(X/\theta\right)^{m}}{\left(X/\theta\right)^{m} + \theta\left(\Gamma\right)^{m}} < 1 \tag{260}$$

$$0 < C_{d}\left(X,\Gamma\right) < C_{\infty}\left(\Gamma\right) < 1 \tag{261}$$

and the following obtained from Eq. (258):

$$\frac{\partial C_{d}}{\partial X} = C_{\infty}\left(\Gamma\right)\frac{m\,\theta^{m} X^{m-1}}{\left(X^{m} + \theta^{m}\right)^{2}} > 0 \tag{262}$$

then, one may deduce that the discharge coefficient C_d is strictly increasing in X. Below, we adopt the following notation $\theta(\Gamma) \equiv \theta$.

Correct asymptotes

For an easy asymptotic analysis, write Eq. (258) in the following form:

$$C_{d}\left(X,\Gamma\right) = C_{\infty}\left(\Gamma\right)\frac{\left(X/\theta\right)^{m}}{\left[1+\left(\dfrac{X}{\theta}\right)^{m}\right]} \tag{258b}$$

Thus, for shallow flow depth, or shallow regime, i.e., $X << \theta$ or $X/\theta \to 0$, one may write what follows:

$$\lim_{x\to 0}\frac{1}{1+x} = 1,\; x = \left(X/\theta\right)^{m}$$

Thus, Eq. (258b) allows writing the following:

$$C_{d} \sim C_{\infty}\left(\frac{X}{\theta}\right)^{m} \tag{263}$$

On the other side, Eq. (258) can be also rewritten as follows:

$$C_d = C_\infty \frac{1}{1+(\theta/X)^m} \tag{258c}$$

For deep flow depth, or deep regime, corresponding to $X >> \theta$ or $\theta/X \to 0$, the following can be written:

$$\frac{1}{1+x} = 1 - x + \left(O(x)^2\right),\ x = (\theta/X)^m \tag{264}$$

Thus, Eq. (258c) reduces to the following:

$$C_d = C_\infty\left[1-(\theta/X)^m\right] + \left(O(\theta/X)^{2m}\right) \tag{265}$$

Elasticity with respect to the upstream flow depth h

Let's reconsider the same formulation of that presented in Eq. (250), which defines the total depth elasticity as a clean split of a direct depth part E and a contraction part N via the chain rule. Thus, the following can be written:

$$E_h^{(C_d)} = \frac{\partial \ln C_d}{\partial \ln h} = \underbrace{\left.\frac{\partial \ln C_d}{\partial \ln X}\right|_{\Gamma\ \text{fixed}}}_{\mathrm{E}(X)} + \underbrace{\left.\frac{\partial \ln C_\infty}{\partial \Gamma}\right|_{X\ \text{fixed}} \frac{d\Gamma}{d\ln h}}_{\mathrm{N}(\Gamma)} \tag{266}$$

With $X = h/b$ given by Eq. (79) and using the exact decomposition expressed by Eq. (92), along with Eq. (90) giving the derivative of Γ with respect to $\ln h$, a short calculation provides the following:

(a) Direct X-path contribution

Using the authors' notation y expressed by Eq. (127), the kernel S [Eq. (S-1)] can be rewritten as follows:

$$S(y) = \frac{y}{1+y} \tag{S-2}$$

Because $C_\infty(\Gamma)$ is independent of X along the fixed-Γ path, and considering Eq. (266), the following can be written:

$$\mathrm{E}(X) = \left.\frac{\partial \ln C_d}{\partial \ln X}\right|_\Gamma = \frac{\partial \ln}{\partial \ln X} S(X,\theta,m) \tag{267}$$

Differentiating $S(y)$ given by Eq. (S-2) while considering Eq. (127) and θ held constant, the following can be written:

(a-1) The derivative of y with respect to X gives what follows:

$$\frac{dy}{dX} = \frac{d}{dX}\left(\frac{X}{\theta}\right)^m = \frac{m}{\theta^m} X^{m-1} = \frac{my}{X} \tag{268}$$

(a-2) Taking into account Eq. (127), the derivative of $S(y)$, expressed by Eq. (S-2), with respect to X yields the following:

$$\frac{dS}{dX} = \frac{(1+y)\dfrac{dy}{dX} - y\dfrac{dy}{dX}}{(1+y)^2} = \frac{1}{(1+y)^2}\frac{dy}{dX} \tag{269}$$

Converting to the requested log-derivative, and taking into account Eqs. (S-2), (268) and (269), the following can be written:

$$\mathrm{E}(X) = \frac{\partial \ln S}{\partial \ln X} = \frac{X}{S}\frac{dS}{dX} = \frac{X}{y/(1+y)}\frac{1}{(1+y)^2}\frac{my}{X}$$

After simplification, the following can be obtained:

$$\mathrm{E}(X) = \frac{m}{(1+y)} \tag{270}$$

Finally, substituting Eq. (127) into Eq. (270) results in the following:

$$\mathrm{E}(X) = \frac{m}{1 + \left(\dfrac{X}{\theta}\right)^m} \tag{271}$$

This is the compact closed form for the direct X-path elasticity of the HIS model implied by Eq. (258). It is the same quantity the manuscript calls for when it introduces the HIS asymptotics around Eqs. (258a) to (265) and then proceeds to the "(a) Direct X-path contribution." E(X) tends to m for $X << \theta$ corresponding to shallow flow depth, or shallow regime, while (X) tends to 0 for $X >> \theta$, corresponding to deep flow depth, or deep regime.

(b) Direct contraction path N(Γ) contribution through $C\infty(\Gamma)$

N(Γ) is expressed by the second term of Eq. (266). The derivatives have been already expressed by Eq. (255) as follows:

$$\mathrm{N}_{\Gamma}^{(C_d)} = \frac{\partial \ln C_\infty}{\partial \Gamma} \frac{d\Gamma}{d \ln h} = \frac{C_\infty^{'}}{C_\infty} \Gamma \left(1 - \frac{\Gamma}{k}\right) \tag{255}$$

As $h \to \infty$, corresponding to deep flow depth, or deep regime, $\Gamma \to k$, hence $\mathrm{N}(\Gamma) \to 0$.

(c) Total depth elasticity

The total depth elasticity is given by the sum of Eqs. (71) and (255). The final result is as follows:

$$E_h^{(C_d)} = \frac{m}{1 + \left(\frac{X}{\theta}\right)^m} + \frac{C_\infty^{'}(\Gamma)}{C_\infty(\Gamma)} \Gamma \left(1 - \frac{\Gamma}{k}\right) \tag{272}$$

Elasticity with respect to C∞

From Eq. (258), one may derive easily the following:

$$\frac{\partial \ln C_d}{\partial \ln C_\infty} = 1, \text{ everywhere} \tag{273}$$

Elasticity with respect to θ

From Eq. (258), the following can be written:

$$\frac{\partial \ln C_d}{\partial \ln \theta} = - \frac{m}{1 + \left(\frac{X}{\theta}\right)^m} = - \mathrm{E}(X) \tag{274}$$

Elasticity with respect to m

Using Eq. (258), yield the following:

$$\frac{\partial \ln C_d}{\partial \ln m} = - \frac{\theta^m}{\left(\frac{X}{\theta}\right)^m + \theta^m} \ln\left(\frac{X}{\theta}\right) \tag{275}$$

Thus, the sensitivity to m is negative for $X < \theta$, zero at $X = \theta$, and positive for $X > \theta$; the same qualitative structure proved for ATS in Eq. (233).

Calibration recipe

(a) Step 0 (Predictors and response)

AOM/RPS/BPS/HSE/ATS procedures, build:

Xi = hi/bi [Eq. (77)], and C_d,i = Qi / Q_{Th} (hi)

Keep $0 < C_d$,i ≤ 1.

(b) Step 1 (Plateau vs. Contraction)

On the deep subset (top 20–30% Xi), fit $C\infty(\Gamma) = c_0 + c_1\Gamma + c_2\Gamma^2$ with constraints expressed by Eq. (84), and $0 < C\infty < 1$; analogous to steps around Eqs. (82), (84), (86).

(c) Step 2 (half-saturation knee)

Normalize

Ci = C_d,i / $C\infty(\Gamma$i$)$ ∈]0, 1[.

Because the Hill core satisfies the following:

$$\frac{C}{1-C} = \left(\frac{X}{\theta}\right)^m \tag{276}$$

thus, the exact half-saturation occurs at $C = 1/2$ corresponding to $X = \theta$ according to Eq. (276). Estimate θ by locating where Ci crosses 0.50; linear interpolation between consecutive X values bracketing 0.50, as do for HSE/ATS [cf. Eqs. (126a), (175) and the median-based practice].

(d) Step 3 (Shape exponent m)

With θ fixed, linearize Eq. (276) as follows:

$$\ln\left(\frac{C}{1-C}\right) = m\,\ln(X) - m\,\ln(\theta) \tag{277}$$

Then, a least-squares fit of the following:

$$\ln\left(\frac{C\mathrm{i}}{1-Ci}\right) \text{ vs } \ln(X\mathrm{i}) \tag{278}$$

gives m (slope) and a check on θ (intercept). If shallow data are sparse, initialize $m \in [0.6, 2.5]$, as in your AOM guidance and polish jointly.

Simple Exponential Saturation (SES) model

The SES model is also known as the “Weibull CDF”, having the same mathematical form as the Cumulative Distribution Function of a Weibull distribution.

The SES model is a compact, three-parameter family for the discharge coefficient C_d that stays fully inside the adopted X–Γ framework while offering a steeper, yet still well-behaved, transition from shallow to deep regimes. It keeps the same similarity controls, i.e., relative flow depth X = h/b [Eq. (79)] and a contraction descriptor Γ, and the same light-weight quadratic ceiling C∞(Γ), as defined by Eq. (82), with the mild consistency constraints [Eqs. (82) and (84)]. In other words, SES changes only the *shape* of the rise toward the ceiling; all the definitions, constraints, and asymptotic targets remain exactly those already used throughout the paper.

Like HSE/ATS/HIS families, SES is built around a half-saturation marker θ: by design the curve reaches precisely half of its ceiling at $X = \theta$, giving the same clear “knee” used elsewhere for parameter reading and comparisons [cf. Eq. (175)], and its role in the ATS section. What SES contributes is a *stretched-exponential* approach to the ceiling: the onset at small X is an exact power law with exponent m, while the tail at large X decays faster than any power; there is no overshoot, strictly increasing, and numerically tame. The result is a bounded, monotone curve whose parameters (C∞, θ, m) keep the same immediate physical interpretation the authors already established: vertical scale (ceiling), horizontal location (knee), and steepness (shape).

SES slots directly into the adopted elasticity toolkit. The depth sensitivity with respect to the upstream flow depth is decomposed by the same chain-rule split into a direct depth term E and a contraction pathway N [Eq. (250)], with the contraction drift governed by the same dΓ/dln$h$ we already use [Eq. (90)]. Thus, the qualitative story carries over unchanged: E dominates in the shallow regime, i.e, $X << \theta$; both E and N fade as $X \rightarrow \infty$ and $\Gamma \rightarrow k$, so the total elasticity vanishes at flow depth and C_d levels off at the contraction-limited ceiling. Practically, this means SES can be analyzed, compared, and uncertainty-propagated with the very same equations and workflows as uses for:

AOM/RPS/BPS/HSE/ATS/HIS.

Because SES preserves the half-saturation convention, the users can lift the existing three-step field routine without modification: (1) read C∞(Γ) versus Γ using the familiar quadratic Eq. (82) under constraints in Eq. (84); (2) locate θ at the 50% crossing; (3) estimate the shape m from the shallow log–log slope and refine all parameters with a short bounded least-squares pass. No new knobs or hidden states are introduced; SES is simply a different, often sharper, “riser” plugged into the same ceiling and elasticity architecture.

In short, SES is strong, bounded, monotone, asymptotically correct, and contraction-aware, and simple, three interpretable parameters, half-saturation preserved, and full drop-in compatibility with the adopted ceiling [Eqs (82)/(84)], elasticity split [Eq. (92)], and Γ-drift [Eq. (90)]. It gives practitioners a crisp, noise-robust curve that rises briskly when shallow and flattens decisively when deep, without changing any of the surrounding machinery they already use.

C_d-SES model

The SES, similar to Weibull CDF, gives a bounded, strictly increasing, half-saturating curve with an exact power-law take-off and a power-law tail to the ceiling. It stays within the X–Γ framework and slots directly into your (E + N) elasticity split [Eqs. (90), and (92)].

Definition

The core form of the C_d-SES model is expressed as follows:

$$C_d\,(X,\Gamma) = C_\infty(\Gamma)\left\{1 - \exp\left[\left(-\ln 2\right)\left(X/\theta\right)^m\right]\right\} \tag{279}$$

Positioning inside the X–Γ framework

We keep the same similarity controls and ceiling we already adopted throughout the present monograph, as recalled in the following:

(a) The relative flow depth $X \equiv h/b$ define by Eq. (79);

(b) The contraction descriptor Γ, or the compound contraction index, expressed by Eq. (77a);

and

(c) the following geometry parameter, or the lateral contraction index, $k = 2b/\mathrm{B}$, as defined by Eq. (89).

(d) The quadratic ceiling defined by Eq. (84), with mild constraints given by Eq. (84), and no risk of $C_d > 1$:

$$C_\infty\left(\Gamma\right) = c_0 + c_1\Gamma + c_2\Gamma^2\,,\;\; 0 < C_\infty\left(\Gamma\right) < 1 \tag{82}$$

with our usual mild constraints, defined as follows:

$$0 < c_0 < c_0 + c_1 + c_2 < 1 \tag{84}$$

(e) The flow depth-elasticity is always split by the chain rule into a direct flow depth term E and a contraction pathway N, as presented in Eq. (250); the Γ-drift with flow depth uses the closed form of Eq. (90).

(f) To preserve the "half-saturation at $X = \theta$" convention (cf. knee definition we use elsewhere), we normalize SES so that the normalized core reaches 1/2 at $X = \theta$; thus, the following can be suggested:

$$C_d(X,\Gamma) = C_\infty(\Gamma) \underbrace{\left[1 - 2^{-\left(X/\theta\right)^m}\right]}_{S(X;\theta;m)} \tag{280}$$

The ceiling C∞(Γ) and its constraints are exactly those in Eqs. (82) and (84). Herein, $\theta > 0$ sets the knee, i.e., the half-saturation abscissa, and $m > 0$ sets the shape/steepness. This slots into exactly the same X–Γ architecture we used for AOM/RPS/BPS/HSE/ATS/HIS.

Let $y \equiv (X/\theta)^m$, the same auxiliary variable as in your Hill/HSE sections, cf. Eq. (127), so that the kernel is as follows:

$$S = 1 - 2^{-\left(X/\theta\right)^m}, \; y = \left(X/\theta\right)^m \text{ [Eq.}(127)] \tag{281}$$

Eq. (281) can be rewritten in the following reduced form:

$$S = 1 - 2^{-y} \tag{281a}$$

Physics-consistent properties

(a) Bounds and ceiling

Because

$$0 < 2^{-y} < 1 \text{ for } y > 0$$

we have the following:

$$0 < S < 1$$

Therefore, these conditions, along with Eq. (280), allow writing the following:

$$0 < C_d\left(X,\Gamma\right) < C_\infty\left(\Gamma\right) \tag{282}$$

(b) Monotonicity in the flow depth

One may write the following chain rule:

$$\frac{dS}{dX} = \frac{dS}{dy}\frac{dy}{dX} \tag{283}$$

On the other hand, it can be derived from Eq. (281a) what follows:

$$\frac{dS}{dy} = \frac{d}{dy}\left(1 - 2^{-y}\right) = -\frac{d}{dy}\left(2^{-y}\right) = 2^{-y}\ln 2 \tag{283a}$$

$$\frac{dy}{dX} = \frac{d}{dy}\left(\frac{X}{\theta}\right)^m = \frac{m\,X^{m-1}}{\theta^m} \tag{283b}$$

Introduction the y Eq. (127) into Eq. (283b) yields the following:

$$\frac{dy}{dX} = = \frac{m\,y}{X} \tag{283c}$$

Thus, substituting Eqs (283a) and (283c) into Eq. (283), the following can be written:

$$\frac{dS}{dX} = \ln(2)\; 2^{-y}\; \frac{m\,y}{X} > 0 \tag{284}$$

Eq. (280) allows writing the following:

$$\frac{dC_d}{dX} = C_\infty(\Gamma)\,\frac{dS}{dX} > 0 \tag{285}$$

Thus, one may deduce that SES is strictly increasing in X, mirroring our monotonicity checks used across models. Users can compare the monotonic proofs the authors write around Eq. (244) for RDP.

(c) Correct asymptotes

(c-1) For shallow regime, we know that $X << \theta$, or $y << 1$. Using the following development:

$$2^{-y} = e^{-y\ln(2)} = 1 - y\ln(2) + O\left(y^2\right) \tag{286}$$

Thus, Eq. (281a) allows writing the following:

$$S = 1 - 2^{-y} = y\ln(2) + O\left(y^2\right) \tag{287}$$

Substituting Eq. (127) into Eq. (287) yields the following:

$$S = \left(\frac{X}{\theta}\right)^m \ln(2) + O\left(\left(X/\theta\right)^{2m}\right) \tag{287a}$$

Thus, Eq. (280) becomes as follows:

$$C_d(X,\Gamma) \sim C_\infty(\Gamma)\left(\frac{X}{\theta}\right)^m \ln(2) \tag{288}$$

This is the power-law take-off with exponent m.

(c-2) For deep regime, we know that $X >> \theta$, or $y >> 1$, or $y \rightarrow \infty$. Since:

$$2^{-y} \rightarrow 0 \tag{289}$$

Thus, according to Eq. (281a), the following can be written:

$$S \rightarrow 1 \tag{290}$$

Substituting this result into Eq. (280) yields the following:

$$C_d\,(X, \Gamma) \sim C_\infty(\Gamma) \tag{291}$$

This is the contraction-limited ceiling.

Direct flow depth elasticity E(X) (Fixed Γ)

From Eqs. (266) and (267), the following can be written:

$$\mathrm{E}\left(X\right) = \left.\frac{\partial \ln C_d}{\partial \ln X}\right|_{\Gamma \text{ fixed}} = \frac{\partial \ln S}{\partial \ln X} = \frac{X}{S}\frac{dS}{dX} \tag{292}$$

Substituting Eqs. (281a) and (284) into Eq. (292) yields the following:

$$\mathrm{E}\left(X\right) = = \frac{X}{1-2^{-y}} \ln\left(2\right) 2^{-y}\ \frac{m\,y}{X}$$

After simplification, one may obtain the following:

$$\mathrm{E}\left(X\right) = = \frac{m \ln\left(2\right) y\, 2^{-y}}{1-2^{-y}} \tag{293}$$

Substituting Eq. (127) into Eq. (293) the following final form of E(X) is obtained:

$$\mathrm{E}\left(X\right) = \frac{m \ln\left(2\right)\left(\dfrac{X}{\theta}\right)^m\ 2^{-\left(X/\theta\right)^m}}{1-2^{-\left(X/\theta\right)^m}} \tag{293a}$$

Eq. (293a) can be rewritten as follows:

$$\mathrm{E}\left(X\right) = \frac{m \ln\left(2\right)\left(\dfrac{X}{\theta}\right)^m\ 2^{-\left(X/\theta\right)^m}}{1-2^{-\left(X/\theta\right)^m}} \tag{293b}$$

or in the following reduced form:

$$\mathrm{E}(X) = m\ln(2)\frac{y}{2^{y}-1}, \quad y=(X/\theta)^{m} \tag{293c}$$

Proceed to checks as follows.

(a) For shallow regime, we know that X << θ, or y << 1, or y → 0, one may first recall the following results:

$$2^{-(X/\theta)^{m}} \approx 1-\ln(2)(X/\theta)^{m} \tag{286}$$

$$1-2^{-y} \sim \left(\frac{X}{\theta}\right)^{m}\ln(2) = y\ln(2) \tag{287}$$

Substituting Eqs. (286) and (287) into Eq. (293a), and after simplification, yield the following final result for the initial log-log slope:

$$\mathrm{E} \approx m \tag{294}$$

(b) At the half-saturation, corresponding to X = θ, and after simplification, Eq. (293a) gives the following final result:

$$\mathrm{E} \approx m\ln(2) \tag{295}$$

(c) For deep regime, we know that X >> θ, or y >> 1, or y → ∞, one may derive the following result:

$$\lim_{y\to\infty}\left(\frac{y}{2^{y}}\right) = 0, \; y=(X/\theta)^{m} \tag{296}$$

Recall Eq. (289) for deep regime as follows:

$$2^{-y} \to 0 \tag{289}$$

Substituting firstly Eq. (289) into Eq. (293) yields the following:

$$\mathrm{E} \sim m\ln(2)\frac{y}{2^{y}} \tag{297}$$

Substituting secondly Eq. (296) into Eq. (297) yields the following final result:

$$\mathrm{E} \to 0 \tag{298}$$

Direct contraction path N(Γ) contribution

In this section, recall Eqs. (82) and (250) as follows:

$$C_\infty(\Gamma) = c_0 + c_1\Gamma + c_2\Gamma^2 \tag{82}$$

$$E_h^{(C_d)} = \frac{\partial \ln C_d}{\partial \ln h} = \underbrace{\frac{\partial \ln S}{\partial \ln X}\frac{\partial \ln X}{\partial \ln h}}_{\mathrm{E}(X)} + \underbrace{\frac{\partial \ln C_\infty}{\partial \Gamma}\frac{d\Gamma}{d\ln h}}_{\mathrm{N}(\Gamma)} \tag{250}$$

E(X) is expressed by Eq. (293) or Eq. (293a).

According to Eqs. (250), and (255), N(Γ) is expressed as follows:

$$\mathrm{N}_\Gamma^{(C_d)} = \frac{\partial \ln C_\infty}{\partial \Gamma}\frac{d\Gamma}{d\ln h} = \frac{C_\infty^{'}}{C_\infty}\Gamma\left(1-\frac{\Gamma}{k}\right) \tag{255}$$

Total depth elasticity E_h (C_d)

On the other hand, Eq. (82) allows writing the following:

$$C_\infty^{'} = \frac{\partial \ln C_\infty}{\partial \Gamma} = \frac{c_1 + 2c_2\Gamma}{c_0 + c_1\Gamma + c_2\Gamma} \tag{299}$$

Substituting Eqs. (82), (255), (293), and (299) into Eq. (250), yields what follows:

$$E_h^{(C_d)} = \frac{m\ln(2)\,y\,2^{-y}}{1-2^{-y}} + \frac{c_1 + 2c_2\Gamma}{c_0 + c_1\Gamma + c_2\Gamma}\Gamma\left(1-\frac{\Gamma}{k}\right) \tag{300}$$

Recall that y is given by Eq (127), while the compound contraction index is expressed by Eq. (77)/(77a).

As h → ∞, i.e., deep regime, according to Eqs. (77a) Γ→ k, implying that the right member of Eq. (300), i.e., N(Γ), falls to zero. On the other hand, for deep regime, Eq. (298) gives E → 0. Thus, the following final result can be written:

$$E_h^{(C_d)} \to 0 \tag{301}$$

Reall that, for deep regime, Eq. (291) gives the following:

$$C_d\,(X,\Gamma) \sim C_\infty(\Gamma) \tag{291}$$

Parameter elasticities (useful for uncertainty)

(a) Elasticity with respect to the ceiling C∞

Let's recall the following equations:

$$X = \frac{h}{b} \tag{79}$$

$$y = \left(X/\theta\right)^m \tag{127}$$

$$C_d\,(X,\Gamma) = C_\infty(\Gamma)\,S\left(X;\theta;m\right) \tag{280}$$

$$S = 1 - 2^{-y} \tag{281a}$$

Eq. (280) allows writing the following:

$$\ln C_d = \ln C_\infty + \ln S \tag{280a}$$

As S is independent of C∞, and holding X, θ, m fixed, differentiating ln (C_d) with respect to ln (C∞), yields the following:

$$\frac{\partial \ln C_d}{\partial \ln C_\infty} = \frac{\partial}{\partial \ln C_\infty}\left(\ln C_\infty + \ln S\right) = \frac{\partial \ln C_\infty}{\partial \ln C_\infty} + \frac{\partial \ln S}{\partial \ln C_\infty} = 1 + 0$$

Thus, the final result is as follows:

$$E_{C\infty}^{(C_d)} = \frac{\partial \ln C_d}{\partial \ln C_\infty} = 1 \tag{302}$$

This means that 1% change in (C∞) produces the same change in the discharge coefficient (C_d).

(b) Elasticity with respect to the knee θ

With X and m fixed, we seek what follows:

$$E_\theta^{(C_d)} = \frac{\partial \ln C_d}{\partial \ln \theta} \tag{303}$$

From Eq. (280a), the following can be written:

$$E_\theta^{(C_d)} = \frac{\partial \ln C_d}{\partial \ln \theta} = \frac{\partial}{\partial \ln \theta}\left(\ln C_\infty + \ln S\right) \tag{304}$$

As (C∞) is independent of the knee θ, Eq. (304) allows writing the following:

$$E_\theta^{(C_d)} = \frac{\partial \ln S}{\partial \ln \theta} \tag{305}$$

On the other hand, from Eq. (127), the following can be written:

$$\frac{\partial y}{\partial \theta} = -m\,X^{m}\,\theta^{-m-1} \tag{306}$$

Using the following identity:

$$\frac{\partial}{\partial \ln\theta} = \theta \frac{\partial}{\partial \theta} \tag{307}$$

Thus, one may write the following:

$$\frac{\partial y}{\partial \ln\theta} = \theta \frac{\partial y}{\partial \theta} \tag{308}$$

Substituting Eq. (306) into Eq. (308) yields the following:

$$\frac{\partial y}{\partial \ln\theta} = \theta\left(-m\,X^{m}\,\theta^{-m-1}\right) \tag{309}$$

Eq. (309) can be rewritten as follows:

$$\frac{\partial y}{\partial \ln\theta} = \theta\left(-m\,X^{m}\,\theta^{-m-1}\right) \tag{310}$$

After simplification, Eq. (310) gives the following:

$$\frac{\partial y}{\partial \ln\theta} = -\,m\left(\frac{X}{\theta}\right)^{m} \tag{311}$$

With Eq. (127) overmentioned, Eq. (311) reduces to the following:

$$\frac{\partial y}{\partial \ln\theta} = -\,m\,y \tag{312}$$

On the other hand, we use the following identity:

$$\frac{\partial \ln S}{\partial \ln\theta} = \frac{1}{S}\frac{\partial S}{\partial \ln\theta} = E_{\theta}^{\left(C_d\right)} \tag{313}$$

Since the C∞ is θ-independent, Eq. (280a) allows writing the following:

$$\frac{\partial \ln C_d}{\partial \ln\theta} = \frac{\partial \ln S}{\partial \ln\theta} \tag{314}$$

Substituting Eq. (313) into Eq. (314) yields the following:

$$\frac{\partial \ln C_d}{\partial \ln \theta} = \frac{1}{S}\frac{\partial S}{\partial \ln \theta} \tag{315}$$

However, one may write the following:

$$\frac{\partial S}{\partial \ln \theta} = \frac{dS}{dy}\frac{\partial y}{\partial \ln \theta} \tag{316}$$

Recall Eqs. (283a) and (312) as follows:

$$\frac{dS}{dy} = 2^{-y}\ln(2) \tag{283a}$$

$$\frac{\partial y}{\partial \ln \theta} = -\,m\,y \tag{312}$$

Substituting Eqs. (283a) and (312) into Eq. (316), one may derive the following:

$$\frac{\partial S}{\partial \ln \theta} = 2^{-y}\ln(2)\,(-\,m\,y)$$

which can be rewritten as follows:

$$\frac{\partial S}{\partial \ln \theta} = -\,m\,\ln(2)\,y\,2^{-y} \tag{317}$$

Substituting Eqs. (281a) that governs S, and (317) into Eq. (313) yields the following:

$$E_\theta^{(C_d)} = \frac{1}{1-2^{-y}}\left[-\,m\,\ln(2)\,y\,2^{-y}\right]$$

After rearranging, the following result is obtained:

$$E_\theta^{(C_d)} = -\,\frac{m\,\ln(2)\,y\,2^{-y}}{1-2^{-y}} \tag{318}$$

Substituting Eq. (127) into Eq. (318), yields the following final form:

$$E_\theta^{(C_d)} = -\,\frac{m\,\ln(2)\left(\dfrac{X}{\theta}\right)^m 2^{-(X/\theta)^m}}{1-2^{-(X/\theta)^m}} \tag{319}$$

This is the elasticity formulation with respect to the knee θ.

From Eqs. (293a) and (319), the following can be written:

$$\mathrm{E}(X) = -\,E_{\theta}^{(C_d)} \tag{320}$$

Eq. (319) can be written in the following form:

$$E_{\theta}^{(C_d)} = -\,m\,\ln(2)\,\frac{y}{2^{y}-1}, \quad y=(X/\theta)^{m} \tag{319a}$$

(c) Elasticity with respect to the shape m, with X, θ, Γ fixed.

By definition, we know the following:

$$E_{m}^{(C_d)} = \frac{\partial \ln C_d}{\partial \ln m} = \frac{m}{C_d}\frac{\partial C_d}{\partial m} = \frac{m}{C_\infty S}\frac{\partial C_d}{\partial m} \tag{321}$$

Because C∞ does not depend on m, only the kernel contributes, from Eq. (280) one may obtain the following:

$$\frac{\partial C_d}{\partial m} = C_\infty \frac{\partial S}{\partial m} = C_\infty \frac{\partial S}{\partial y}\frac{\partial y}{\partial m} \tag{322}$$

From Eq. (127), the following can be written:

$$\frac{\partial y}{\partial m} = y \ln\left(\frac{X}{\theta}\right) \tag{323}$$

On the ither side, Eq. (283a) provides the following:

$$\frac{dS}{dy} = 2^{-y}\ln(2) \tag{283a}$$

Let’s recall S(y) as follows [Eq. (281a)]:

$$S = 1 - 2^{-y} \tag{281a}$$

Substituting Eqs. (281a), (283a), and (322) into Eq. (321), yields the following:

$$E_{m}^{(C_d)} = \frac{m}{C_\infty\left(1-2^{-y}\right)}\, C_\infty\, 2^{-y}\ln(2)\, y \ln\left(\frac{X}{\theta}\right) \tag{324}$$

After simplification and rearrangement, the following final result is obtained:

$$E_m^{(C_d)} = m\ \ln(2)\ \frac{y}{\left(2^y - 1\right)}\ \ln\left(\frac{X}{\theta}\right),\quad y = \left(X/\theta\right)^m \tag{324a}$$

For X < θ, $E_m^{(C_d)}$ is negative, zero at X = θ, and positive at X > θ.

(c-1) For shallow regime, we know that X << θ, or y << 1, or y → 0, one may first recall the following results:

$$2^y - 1 \sim y\ln(2) \tag{287}$$

Thus Eq. (324a) becomes as follows:

$$E_m^{(C_d)} \to m\ \ln\left(\frac{X}{\theta}\right) \tag{325}$$

(c-2) For deep regime, we know that X >> θ, or y >> 1, or y → ∞. The term in Eq. (324a) can be in the following form:

$$\frac{y}{\left(2^y - 1\right)} = \frac{\dfrac{y}{2^y}}{\left(1 - \dfrac{1}{2^y}\right)} \tag{326}$$

For y → ∞, the following can be written:

$$\lim_{y\to\infty} \frac{1}{2^y} = 0 \tag{327}$$

On the other side, Eq. (296) provides the following:

$$\lim_{y\to\infty} \left(\frac{y}{2^y}\right) = 0 \tag{296}$$

With Eqs. (327) and (296), Eq. (326) gives the following:

$$\lim_{y\to\infty} \frac{y}{\left(2^y - 1\right)} = 0 \tag{328}$$

Thus, Eq. (324a) allows writing the following final result:

$$E_m^{(C_d)} \to 0 \tag{329}$$

Calibration recipe– C_d-SES (Exponential Saturation)

Core

Use the SES form (Weibull CDF kernel) already introduced for C_d-SES, with ceiling $C\infty(\Gamma)$, half-saturation θ, and shape m, all inside the existing X–Γ framework.

Build Xi ≡ hi/bi and Γ exactly as for the previous considered models; keep the quadratic ceiling and its mild constraints.

The normalized SES core reaches one-half at X = θ.

(a) Step 0: Predictors and response

From your measurements {hi, bi, B, P, Qi}, compute the following:

$$X\mathrm{i} = \frac{h\mathrm{i}}{b\mathrm{i}} \tag{79}$$

$$C_d\,\mathrm{i} = \frac{Q\mathrm{i}}{Q_{Th}\,\mathrm{i}} \tag{330}$$

Retain the following:

$$0 < C_d\,\mathrm{i} \le 1$$

(b) Step 1: Plateau vs. Contraction [Fit C∞(Γ)]

On the deep subset, i.e., top ~20–30% of the largest Xi, regress the following:

$$C_\infty(\Gamma) = c_0 + c_1\Gamma + c_2\Gamma^2 \tag{82}$$

under the same mild bounds and monotonicity constraints the authors already use for the ceiling. Keep the following:

$$0 < C_\infty < 1$$

c) Step 2: Half-saturation knee (θ)

Normalize by the fitted ceiling:

$$C\mathrm{i} \equiv \frac{C_d\,\mathrm{i}}{C_\infty(\Gamma\mathrm{i})}, \in\,]0,\, 1[\tag{331}$$

Locate θ at the 50% crossing because SES, by design, satisfies "half of the ceiling at X = θ. Use linear interpolation between the two consecutive X-sorted points that straddle C = 0.50; it is the same practice as in HSE/ATS.

(d) Step 3: Shape exponent m via SES straight-line fit

From the SES definition [Eq. (279)] and its half-saturation normalization [Eq. (280)], the normalized core is as follows:

$$C(X) = \left\{1 - \exp\left[(-\ln 2)(X/\theta)^m\right]\right\} \tag{332}$$

Therefore, the following can be written:

$$\ln\left[-\ln\left(1 - C\mathrm{i}\right)\right] = \ln(2) + m\ln\left(X\mathrm{i}\right) - m\ln(\theta) \tag{333}$$

It is linear in lnX.

Regress

$$\ln\left[-\ln\left(1 - C\mathrm{i}\right)\right] \text{on } \ln\left(X\mathrm{i}\right)$$

using points with reliable Ci ∈]0, 1[; the slope gives m and the intercept checks θ. If shallow data are sparse, initialize m ∈ [0.6, 2.5] before the polish.

(e) Step 4: Joint refinement of all parameters (bounded nonlinear least squares)

(e-1) Goal

Update all five parameters together (c_0, c_1, c_2, θ) using every data point (Xi, Γi, C_d,i), starting from the estimates obtained in Steps 1–3. This implements the brief "bounded least-squares pass" mentioned for SES.

(e-2) Model used in the fit

For each observation, compute the model-predicted discharge coefficient expressed as follows:

$$C_d^{\text{Predicted}}(X\mathrm{i},\Gamma\mathrm{i}) = C_\infty(\Gamma\mathrm{i})\left\{1 - \exp\left[(-\ln 2)(X\mathrm{i}/\theta)^m\right]\right\} \tag{334}$$

where

$$C_\infty(\Gamma\mathrm{i}) = c_0 + c_1\Gamma\mathrm{i} + c_2\Gamma\mathrm{i}^2 \tag{82}$$

It is the model-predicted discharge coefficient evaluated at the i-th data point, using that point's predictors Xi = hi/bi and Γi. The X–Γ framework and the ceiling C∞(Γ) are exactly the ones already defined in the present monograph. The ln (2) factor guarantees that the normalized response equals one-half at X = θ; the "half-saturation at X = θ" convention of Eq. (280).

(e-3) Objective function

Minimize the sum of squared residuals over all the n points, as follows:

$$\min_{c_0, c_1, c_2, \theta, m} \sum_{i=1}^{n} \left[C_{d,i} - C_d^{\text{Predicted}}(X\text{i}, \Gamma\text{i}) \right]^2 \tag{335}$$

If measurement uncertainties are available, users may use weighted least squares by dividing each residual by its standard deviation before squaring.

(e-4) Bounds and constraints

(e-4-1) Enforce θ > 0; use the same mild ceiling constraints already adopted for the quadratic $C\infty(\Gamma)$ [Eq. (84)], and keep $0 < C\infty(\Gamma) < 1$ over the Γ range covered by the data.

(e-5) Initialization

(e-5-1) Initialize (c_0, c_1, c_2) with the Step 1 ceiling fit.

(e-5-2) Initialize θ with the Step 2 50% crossing.

(e-5-3) Initialize m with the Step 3 straight-line estimate.

(f) Convergence and diagnostics

(f-1) After the optimizer converges, verify the half-saturation property by checking that C_d (θ, Γ) = 1/2 $C\infty(\Gamma)$ for representative Γ values; this follows directly from the normalization in Eq. (280).

(f-2) Report summary errors, for example, RMSE, mean absolute error, maximum relative error, and inspect residuals versus X and Γ to ensure no pattern remains.

(f-3) Context

This step keeps SES inside the same X–Γ architecture, i.e., X = h/b and Γ as in Eq. (77a), and uses the same light-weight ceiling as elsewhere [Eq. (82)], so it is directly compatible with the rest of the monograph.

ANALYTICAL FOUNDATIONS OF THE STUDY

Uniform convergence and truncation control

The manuscript replaces numerical quadrature with an exact Euler–Beta series for the dimensionless geometry–flow depth kernel, stated to be valid on the full admissible range and shared by elliptic, semi-elliptic, and circular openings. In practice, the paper supplements the exact series with a compact Padé surrogate whose uniform maximum deviation is ≈ 0.04% over the whole range, effectively providing a built-in truncation/error control for routine calculations. Users can rely on the series for arbitrarily tight accuracy and on the tabulated Padé bound when speed matters.

Endpoint behavior as anchors

The formulation yields a strictly increasing rating and a predictable flattening with flow depth. The manuscript states that the log-slope (elasticity) with respect to flow depth decreases from about 2 near the crest to about 1.25 at full height for the elliptic family, with a representative mid-range value ≈ 1.824 at $\beta = 0.50$, which the paper derives from the exact kernel and its table. These numbers quantify how responsive discharge is to small flow depth changes across the range.

Certified quadratic-over-quadratic surrogate

A short Padé-type law is built on the exact series and the endpoint constraints and then benchmarked point-by-point against the series. The worst deviation (~0.04%) occurs near the upper end of the range, and the table/figure pair in the manuscript documents this behavior. The bound is well below typical field or C_d uncertainties, making the surrogate safe for theoretical design charts and embedded use.

Circular-weir specialization

The circular opening is treated as a rigorous specialization of the same kernel after mapping β to $\xi = h/D$; only the geometric prefactor changes. Consequently, sensitivity metrics and elasticity values transfer directly at matched nondimensional flow depth, unifying elliptic, semi-elliptic, and circular devices within one framework.

Small velocity-of-approach and other non-idealities

The theoretical law is loss-free by design. The manuscript explains that operational ratings are obtained by multiplying the theoretical discharge by a site-calibrated coefficient $C_d < 1$, a clean separation that accommodates approach-flow and installation effects without contaminating the geometry kernel or its end-point physics.

Losses via a discharge coefficient -elasticity remains invariant

Because losses enter multiplicatively through C_d, the elasticity with respect to flow depth is unchanged, the coefficient cancels in the logarithmic derivative. The paper states this explicitly and uses it when discussing mid-range sensitivity at $\beta = 0.50$.

Uncertainty budgeting and measurement priorities

The manuscript uses the elasticity to propagate flow depth-reading errors into discharge uncertainty and to rank contributors. At $\beta = 0.50$, a 1% flow depth error produces ≈ 1.824% discharge error, illustrating that stage accuracy dominates the budget near mid-range, while sensitivity eases toward full height. Guidance follows on allocating measurement precision accordingly.

Reference implementation and pass–fail verification

Verification is table-driven: the manuscript tabulates the exact-series values and the Padé values across the range, with the maximum deviation reported explicitly (~0.04%) and an error curve (Fig. 2). These materials give a simple pass–fail criterion for any independent implementation: reproduce monotonicity and keep the surrogate's error below the tabulated bound.

Template for broader shape families

Within the manuscript's scope, the same kernel architecture already unifies elliptic, semi-elliptic, and circular weirs, differing only by geometric scaling and admissible flow depth range. This structural unification suggests a natural path to other smooth apertures, while keeping the analysis – surrogate - verification workflow intact.

MAIN FINDINGS OF THE STUDY

Unified, exact theoretical discharge law across three weir shapes

The work derives a loss-free, exact stage–discharge relationship for sharp-crested elliptic and semi-elliptic weirs, and obtains the circular weir as a rigorous specialization of the same formulation. The approach separates universal hydraulic scaling from a dimensionless geometry–flow depth kernel, so one analytical framework covers elliptic, semi-elliptic, and circular openings.

Exact Euler–Beta kernel with anchored endpoint physics

The kernel $\Psi(\beta)$ is expressed as an exact Euler–Beta series that enforces the square-root onset at small flow depth, i.e., $\Psi \sim (\pi/8)\times\sqrt{\beta}$ as $\beta \to 0$, and the full-height anchor $\Psi(1) = 4/15$, providing a physics-exact reference for analysis and calibration.

Practice-ready Padé surrogate with uniform sub-0.05% error

A compact Padé-type [2/2] approximation is constructed for $\Psi(\beta)$. Benchmarks against the exact series show a maximum relative deviation ≈ 0.04%, worst near $\beta \approx 0.96$, and even smaller at full height, well below typical field and discharge coefficient uncertainties. This makes the surrogate suitable for design charts and embedded use.

Circular-weir specialization via a simple depth mapping

The same kernel governs the circular case after mapping β to $\xi = h/D$; only the geometric prefactor changes. Consequently, formulas and sensitivities transfer across shapes at the same nondimensional depth.

Verified accuracy over the semi-elliptic operating range

Within $0 \leq \beta \leq 0.50$, the semi-elliptic sub-range, tabulated comparisons show deviations strictly below the global worst case; representative entries remain below 0.01% at the sub-range ceiling.

Differentiability enables sensitivity and uncertainty analysis

Because Ψ is analytic, via the convergent Beta series, the discharge law is differentiable with respect to stage and geometry, enabling trustworthy sensitivity/elasticity measures and error propagation without empirical tuning.

Depth sensitivity (elasticity) quantified across the range

The log-slope of the discharge Q with respect to the flow depth h decreases from ≈2 near the crest to ≈1.25 near full height for the elliptic family. At mid-range, i.e., $\beta = \xi = 0.50$, the computed elasticity is $E_h \approx 1.824$, meaning a 1% flow depth error produces ≈1.824% discharge error.

Geometry sensitivities are transparent

With the kernel depending only on β, sensitivity to the horizontal semi-axis b of the elliptic/semi-elliptic weirs is linear in the prefactor, yielding $E_b = 1$, i.e., a 1% change in b yields a 1% change in Q, while other dependencies follow directly from the closed-form structure.

Implementation and verification are table-driven

The paper tabulates exact-series values and Padé results and provides an error curve, offering a simple pass-fail criterion for any implementation: reproduce monotonicity and keep surrogate errors within the reported ≤ 0.04% bound.

Broader methodological value

The kernel-plus-surrogate architecture, already unifying elliptic, semi-elliptic, and circular weirs, provides a template for extending to other smooth apertures while retaining analytical clarity and computational efficiency.

CONCLUSION

The authors have established an exact theoretical, loss-free stage-discharge law for sharp-crested elliptic and semi-elliptic weirs, with the circular weir recovered as a rigorous specialization of the same kernel architecture. The geometry-flow depth interaction is made analytically explicit via an exact Euler–Beta series for the kernel, ensuring the two physical anchors by construction: the square-root onset at small flow depths and the full-height limit. Building on this foundation, the authors produced a compact Padé-type surrogate with four-significant-figure coefficients that reproduces the exact kernel with uniform, sub-0.05% (max. = 0.03996%) deviation across the full admissible range, well below typical uncertainties from discharge coefficients and instrumentation. Together, these results provide a transparent reference model (exact series) and a practical evaluator (Padé surrogate) that share one formulation across elliptic, semi-elliptic, and circular openings.

The theory cleanly separates physics from geometry: dimensional scaling remains in the Torricelli prefactor, while the kernel carries only shape and normalized flow depth. This separation lets practitioners obtain operational ratings by multiplying the theoretical relation by a site-calibrated discharge coefficient C_d, preserving the correct ordering between theoretical and actual discharge. The closed-form kernel and its surrogate are differentiable and numerically stable, supporting sensitivity analysis, and uncertainty propagation.

The study concluded with a section devoted to a thorough sensitivity analysis, in which, in particular, the authors quantified how the discharge Q is affected by the flow depth-reading error h. In terms of the local elasticity $E_h = \partial \ln Q / \partial \ln h$, a 1% error in h produces roughly 2% error in Q near the crest for elliptic/semi-elliptic weirs, while relaxing to ≈1.25% at full height. The E_h value reaches 2.5% near the crest for circular weirs, while relaxing to ≈1.75% at full height. Thus, the relative error $\Delta Q/Q \approx E_h \times \Delta h/h$ provides a direct rule-of-thumb for uncertainty budgeting: gauge accuracy matters most at small flow depths, while sensitivity decreases as the opening approaches full wetting. The closed-form expressions and endpoint checks reported herein turn these statements into quick, auditable theoretical calculations.

The results are theoretical (loss-free) and do not include approach-velocity effects, aeration, viscosity, surface tension, or contraction losses; these are appropriately absorbed in C_d. Future work should (1) pair the theoretical kernel with systematic C_d calibration for elliptic and semi-elliptic geometries, (2) assess approach-flow and crest-height influences, (3) extend the framework to additional curved apertures, and (4) compile interlaboratory datasets to benchmark combined (theory × C_d) ratings against high-quality measurements.

Declaration of competing interest

The authors declare that they have no known competing financial interests or personal relationships that could have appeared to influence the work reported in this monograph.

REFERENCES

ACHOUR B. (1989). Crestless Jump flow meter with triangular cross section, Journal of Hydraulic Research, Vol. 27, Issue 2, pp. 205-214. (In French)

ACHOUR B. (2013). Semi-modular Rectangular Broad-crested Flow Meter with Lateral Contraction, International Journal of Engineering & Technology Sciences (IJETS), Vol. 1, Issue 5, pp. 310-323.

ACHOUR B., AMARA L. (2021a). Theoretical discharge coefficient relationship for contracted and suppressed rectangular weirs, Larhyss Journal, No 45, pp. 165–182.

ACHOUR B., AMARA L. (2021b). Discharge coefficient of a parabolic weir: theory and experimental analysis, Larhyss Journal, No 46, pp. 77-88.

ACHOUR B., AMARA L. (2021c). Theoretical discharge coefficient relationship for a contracted triangular notch weir, experimental analysis for the 90° V-notch, Larhyss Journal, No 46, pp. 89-100.

ACHOUR B., AMARA L. (2021d). Discharge coefficient for a triangular notch weir: theory and experimental analysis, Larhyss Journal, No 46, pp. 7-19.

AMARA L., ACHOUR B. (2021e). Theoretical approach to stage-discharge relationship for a circular sharp-crested weir, Larhyss Journal, No 46, pp. 101-113.

ACHOUR B., AMARA L. (2022a). Accurate discharge coefficient relationship for the Crump weir, Larhyss Journal, No 52, pp. 93-115.

ACHOUR B., AMARA L. (2022b). Triangular broad-crested weir: theory and experiment, Larhyss Journal, No 49, pp. 37-66.

ACHOUR B., AMARA L. (2022c). Rectangular broad-crested flow meter with lateral contraction: theory and experiment, Larhyss Journal, No 49, pp. 85-112.

ACHOUR B., AMARA L. (2022d). Discharge coefficient relationship for the sharp-edged width constriction, new theory and experiment, Flow Measurement and Instrumentation, Vol. 88, Paper ID 102269, pp. 1-16.

ACHOUR B., AMARA L., MEHTA D. (2022e). Control of the hydraulic jump by a thin-crested sill in a rectangular channel, new experimental considerations, Larhyss Journal, No 50, pp. 31-48.

ACHOUR B., AMARA L., MEHTA D., BALAGANESAN P. (2022f). Compactness of hydraulic-jump rectangular stilling basins using a broad-crested sill, Larhyss Journal, No 51, pp. 31-41.

ACHOUR B., AMARA L. (2023a). The 2A triangular weir, design, theory, and experiment, Larhyss Journal, No 55, pp. 191-213.

ACHOUR B., AMARA L. (2023b). Discharge coefficient relationship for the SMBF flume, Larhyss Journal, No 53, pp. 95–115.

ACHOUR B., AMARA L. (2023c). Control of the hydraulic jump by a broad-crested sill in a rectangular channel, new theory and experiment, Larhyss Journal, No 54, pp. 145-174.

ACHOUR B., DE LAPRAY, G. (2023). Curved Wall Triangular Flume (CWTF): design, theory, and experiment, Larhyss Journal, No 56, pp. 139–178.

ACHOUR B., MEHTA D., AZAMATHULLA H.M. (2024). A new trapezoidal flume for open-channel flow measurement - design, theory, and experiment, Larhyss Journal, No 59, pp. 157–179.

ACHOUR B., AMARA L., KULKARNI K.H. (2025a). Development and validation of a modified H-flume for accurate flow measurement in rectangular channels, Larhyss Journal, No 61, pp. 241–286.

ACHOUR B., AMARA L., KULKARNI K.H. (2025b). In-depth investigation of flow measurement using sharp-edged width constriction in trapezoidal open channels, Larhyss Journal, No 62, pp. 7-35.

ACHOUR B., AMARA L., KULKARNI K.H. (2025c). Development and validation of a modified H-flume for accurate flow measurement in rectangular channels, Larhyss Journal, No 61, pp. 241–286.

BENDER C.M., ORSZAG S.A. (1999). Advanced Mathematical Methods for Scientists and Engineers I: Asymptotic Methods and Perturbation Theory, Book, Springer Editions, New York, NY, USA, 593p.

BIJANKHAN M., and FERRO V. (2018). Assessing stage-discharge relationships for circular overflow structure, Journal of Irrigation and Drainage Engineering, Vol. 144, Issue 1, Paper ID 04017053.

BLEISTEIN N., HANDELSMAN R.A. (1986). Asymptotic Expansions of Integrals, Book, Dover Publications, New York, NY, USA, 425p.

BOS M. G. (1989). Discharge Measurement Structures, Book, 3rd Edition, International Institute for Land Reclamation and Improvement (ILRI), Wageningen, The Netherlands, 410 p.

CHOW V.T. (1959). Open-Channel Hydraulics, Book, McGraw-Hill Book Company, Inc., New York, NY, USA, 680 p.

FRENCH R.H. (1985). Open-Channel Hydraulics, Book, Chapter 8 “Weirs and Orifices”, McGraw-Hill Book Company, New York, NY, USA, pp. 321-330.

GREVE F.V. (1932) Flow of water through circular, parabolic, and triangular vertical notch weirs, Engineering bulletin, Purdue university, Vol. 40, Issue 2, pp. 37-60.

HENDERSON F.M. (1966). Open Channel Flow, Book, Chapter 5 “Weirs and Critical Flow Structures”, Macmillan Publishing Co., New York, NY, USA, pp. 157-164.

ISO (International Organization for Standardization). (2017). ISO 1438: Hydrometry - Open channel flow measurement using thin-plate weirs, Geneva, Switzerland.

MOHAMMED-ALI W.S. (2012). Hydraulic characteristics of semi-elliptical sharp crested weirs, International Review of Civil Engineering (IRECE), Vol. 3, Issue 1, pp. 42-46.

MUNSON B.R., YOUNG D.F., OKIISHI, T.H., HUEBSCH W.W. (2013). Fundamentals of Fluid Mechanics, Book, 7th Edition, John Wiley & Sons, Inc., Hoboken, New Jersey, NJ, USA, 768p.

NICOSIA A., DI STEFANO C., SERIO M.A., FERRO V. (2023). Effect of the crest height on the stage-discharge formula of rectangular and triangular sharp-crested weirs under free-flow conditions, Flow Measurement and Instrumentation, Vol. 93, Paper ID 102421.

NOVAK P., GUINOT V., JEFFREY A., REEVE D. (2010). Hydraulics of Open Channel Flow, Book, 2nd Edition, Chapter 9 "Weirs and Critical Flow Structures", Chemical Rubber Company (CRC) Press, Boca Raton, Florida, FL, USA, pp. 278–283.

OLVER F.W.J., LOZIER D.W., BOISVERT R.F., CLARK C.W. Editions (2010). Handbook of Mathematical Functions, Chapter §5.12 "Beta Function", National Institute of Standards and Technology (NIST), Cambridge University Press, United Kingdom, UK, 968p.

PARSAIE A., BASITNEJAD M., BAHRAMI-YARAHMADI M. (2025). Numerical Modeling and Discharge Coefficient Analysis of Semi-Elliptical Sharp-Crested Weirs, Flow Measurement and Instrumentation, Vol. 106, Paper ID 103035.

SOMMERFELD J.T., STALLYBRASS M.P. (1996). Flow equations for parabolic and elliptical weirs, Journal of Environmental Science & Health Part A, Vol. 31, Issue 4, pp. 905-912.

STEVENS J.C. (1957). Flow through circular weirs, Journal of the Hydraulics Division, Vol. pp. 1455-1 – 1455-24.

SWAMEE P.K. (1988). Generalized rectangular weir equations, Journal of Hydraulic Engineering, Vol. 114, Issue 8, pp. 945-949.

USBR (U.S. Bureau of Reclamation**).** (2001)**.** Water Measurement Manual, 3rd Edition, U.S. Department of the Interior, Bureau of Reclamation, Denver, Colorado, CO, USA.

VATANKHAH A.R. (2010). Flow measurement using circular sharp-crested weirs, Flow Measurement and Instrumentation, Vol. 21, Issue 2, pp 118–122.

VATANKHAH A.R. (2011). Approximate solutions to complete elliptic integrals for practical use in water engineering, Journal of Hydrologic Engineering, Vol.16, Issue 11, pp. 942-945.

VATANKHAH A.R. (2012). Head–Discharge Equation for Sharp-Crested Weir with Piecewise-Linear Sides, Journal of Irrigation and Drainage Engineering, American Society of Civil Engineers (ASCE), Vol. 138, Issue 11, pp. 1011–1018.

VATANKHAH A.R. (2016). Discussion of "Stage-Discharge Models for Concrete Orifices: Impact on Estimating Detention Basin Drawdown Time" by WT Barlow and D. Brandes, Journal of Irrigation and Drainage Engineering, Vol. 142, Issue 11, Paper ID 07016016.

VATANKHAH A.R. (2018). Discussion of "Assessing Stage-Discharge Relationships for Circular Overflow Structure" by Bijankhan M. and Ferro V., Journal of Irrigation and Drainage Engineering, Vol. 144, Issue 11, Paper ID 07018033.

VATANKHAH A.R. (2022). Discussion of "Stage–Discharge Rating Equation for an Elliptical Sharp-Crested Weir", Journal of Irrigation and Drainage Engineering, American Society of Civil Engineers (ASCE), Vol. 148, Issue 2, Paper ID 07021005.

THEORETICAL APPENDIX A1

The present theoretical Appendix A1 develops explicit, end-point approximations that link the exact stage-discharge law of the main text to a practical, closed-form estimate of the flow depth (stage) normalized by the opening height $2a$. Starting from the exact kernel formulation of Eq. (3a), the appendix defines a relative discharge and recasts the rating into an implicit relationship $\beta^{3/2} \times \Psi(\beta)$ = constant. Two asymptotic regimes are then extracted directly from the kernel's built-in physics: the small-flow depth (near-crest) onset and the near-full-flow depth anchor. Each regime yields an explicit approximation for β, and their intersection identifies a natural crossover, a discharge and flow depth at which the two limits agree and where a piecewise explicit rule provides a uniformly accurate, easily computed estimate across the operating range. The theoretical appendix A1 also states admissibility bounds for the relative discharge, explains the uniqueness and good conditioning of the resulting β solution, and interprets the crossover in physical terms (transition from crest-dominated to deep-flow behavior). Finally, the text clarifies how these formulas support implementation: they supply fast initial values for solving the exact implicit equation and integrate seamlessly with the manuscript's exact kernel and its uniformly tight Padé surrogate.

β–Q^* relationship from the Exact Rating Law

Elliptic and semi-elliptic weirs governing relationship

From the exact discharge law (Eq. 3a), the nondimensional depth enters only through the geometry-flow depth kernel $\Psi(\beta)$, with $\beta = h/(2a)$. Introducing the following relative discharge:

$$Q^* = \frac{Q}{4b\sqrt{2g}\left(2a\right)^{3/2}} \tag{A1-1}$$

Eq. (3a) yields the following exact relationship:

$$\beta^{3/2}\Psi\left(\beta\right) = Q^* \tag{A1-2}$$

This follows directly from the "shape-exact, scale-exact" form of Eq. (3a), where the Torricelli prefactor carries all dimensions and the kernel carries the geometry-flow depth coupling. The same Q^*–β mapping applies to elliptic, semi-elliptic, and, by specialization to circular weirs, $\beta \rightarrow \xi$; only the geometric prefactor used in forming Q^* and the admissible range of the depth ratio change. This is why Q^* is the natural similarity variable across the curved-weir family.

Employing the exact Euler–Beta series of Eq. (10) together with the exact relation (A1-2), the authors tabulate below the exact β values, as a function of the relative discharge

Q^*. To compute the requested β values, the authors employ high-precision summation of the Euler–Beta series, as follows, with tight convergence tolerance:

$$\sqrt{\beta}\sum_{n\geq 0}(-1)^n\binom{\frac{1}{2}}{n}\mathrm{B}\left(n+\frac{3}{2},\frac{3}{2}\right)\beta^n \tag{A1-3}$$

The calculation included the endpoint verification, so that Ψ(1) = 4/15 = 0.266666679, giving $Q^*(1) = 4/15$, according to Eq. (A1-2); the table matches this to machine precision.

Table A1-1: Exact β–Q^* according to Eq. (A1-2); $\beta \in [0, 1]$, $\Delta\beta = 0.05$

β	**Exact $\Psi(\beta)$ Eq. (10)**	**Exact Q^* Eq. (A1-2)**
0.00	0.00	0.00
0.05	0.0867038279	0.0009693783
0.10	0.1210275037	0.0038272257
0.15	0.1462470311	0.0084961847
0.20	0.1665437079	0.0148961221
0.25	0.1835506661	0.0229438333
0.30	0.1981093815	0.0325526931
0.35	0.2107198381	0.0436322381
0.40	0.2217059452	0.0560876606
0.45	0.2312895570	0.0698191882
0.50	0.2396280469	0.0847213085
0.55	0.2468350677	0.1006817821
0.60	0.2529926458	0.1175803565
0.65	0.2581583433	0.1352870417
0.70	0.2623692706	0.1536597166
0.75	0.2656437147	0.1725406540
0.80	0.2679804104	0.1917511726
0.85	0.2693545210	0.2110827084
0.90	0.2697071294	0.2302799841
0.95	0.2689164493	0.2490019661
1.00	0.2666666679	0.2666666679

What the numbers in Table A1-1 show, and why that matters

Monotone, well-behaved map: $Q^*(\beta)$ increases smoothly from 0 at $\beta = 0$ to the endpoint $4/15 \approx 0.2666667$ at $\beta = 1$. This guarantees a unique β for any admissible Q^* and makes interpolation straightforward.

Near-crest behavior is gentle but quadratic: For small flow depths, the table values grow roughly like $\propto\beta^2$. Example: at $\beta = 0.10$, $Q^*(0.10) \approx 3.83\times10^{-3}$; at $\beta = 0.20$ it's $\approx 1.49\times10^{-2}$, about 4×larger, consistent with a β^2 trend. This tells that tiny flow depth errors are amplified near the crest, meaning that the user must use a precise gauge there.

Mid-range is the practical "workhorse": Around $\beta \approx 0.45$ - 0.55 the table entries climb quickly but predictably, e.g., $Q^*(0.50) \approx 0.08472$. This means that in that band, the elasticity, i.e., log-slope with respect to flow depth, is moderate, around $E_h \approx 1.8$, so the inverse problem $Q^* \mapsto \beta$ is numerically stable, Newton or even linear interpolation converges quickly and reliably. By contrast, very small β has higher sensitivity, small flow depth exaggerates relative errors, and β very close to 1 has a flatter slope, which can slow inversion slightly.

Full depth is capped and stable: The last row, $Q^*(1) = 4/15$, is a non-negotiable upper bound. If a computed Q^* exceeds ~0.26670, the inputs, or units, are inconsistent with the theory.

Why the table A1-1 is useful

(1) It gives a portable, dimensionless backbone for design charts and software: one table works for all sizes once one scales by $[4 \times b \times \sqrt{(2g)} \times (2a)^{3/2}]$, or the appropriate shape prefactor.

(2) It de-risks calibration since one can separate geometric scaling and site losses, via C_d, from the exact geometry-flow depth physics.

(3) It's a validation oracle as any implementation of the kernel or any surrogate must reproduce these values, within interpolation/rounding, while staying monotone over β.

(4) The table gives the dimensionless (relative) discharge $Q^*(\beta)$. Once β is picked, one may read, or interpolate, the corresponding $Q^*(\beta)$ from the table A1-1, and then use simply Eq. (A1-1) to get Q_{Th}, provided the geometric characteristics of the device are given.

Step-by-step: (1) Choose $\beta \in [0, 1]$; (2) Read Q^* from Table A1-1; If the picked β is not a listed row, use linear interpolation between the two nearest β entries; (3) Check that the derived Q^* value is within the admissible following range $0 \leq Q^* \leq 4/15 \approx 0.2667$. Values outside this range are not admissible for the loss-free theory, (4) Knowing the geometric characteristics of the device, compute the theoretical discharge Q_{Th} using the definition-Eq. (A1-1) for the elliptic case, as follows:

$$Q_{Th} = \left[4b\sqrt{2g}\left(2a\right)^{3/2} \right] Q^{*} \tag{A1-1a}$$

From Eq. (A1-1a), one may write the following for the circular case:

All quantities in consistent SI units: a, and b in meters, g ≈ 9.81 m/s^2.

The table A1-1 lists the dimensionless mapping expressed by the exact Eq. (A1-2). That kernel Ψ is common to elliptic, semi-elliptic, and circular openings. Therefore, the numerical Q^*–β pairs are shape-independent. What changes by shape is only the geometric scale (prefactor) used to convert between Q and Q^*; the table A1-1 itself does not change.

Exact β–Q^* variation

Fig. A1-1 plots the exact, dimensionless discharge $Q^*(\beta) = \beta^{3/2}\,\Psi(\beta)$ from Eq. (A1-2), evaluated with the kernel $\Psi(\beta)$ via the Euler–Beta series and tabulated in Table A1-1 at $\Delta\beta = 0.05$. It is therefore a direct graph of the loss-free rating law in dimensionless form.

It can be observed that the curve of Fig. A1-1 presents Monotonicity and bounds. The curve rises smoothly from $Q^* = 0$ at $\beta = 0$ to the endpoint $Q^*(1) = 4/15 \approx 0.2667$. This guarantees a unique β for every admissible Q^* and makes interpolation straightforward. Any value of Q^* outside [0, 4/15] is physically inadmissible for the ideal, loss-free theory.

The shape of Fig. A1-1 reveals endpoint physics. at small β, near the crest, i.e., $\beta \to 0$, the curve starts gently and steepens, a convex-up beginning. Close to full wetting, i.e., $\beta \to 1$, $\Psi(1) = 4/15$ flattens the curve as it approaches its cap. In elasticity terms, sensitivity drops from about 2 near the crest toward ≈1.25 at full depth, explaining the visible tapering of the slope.

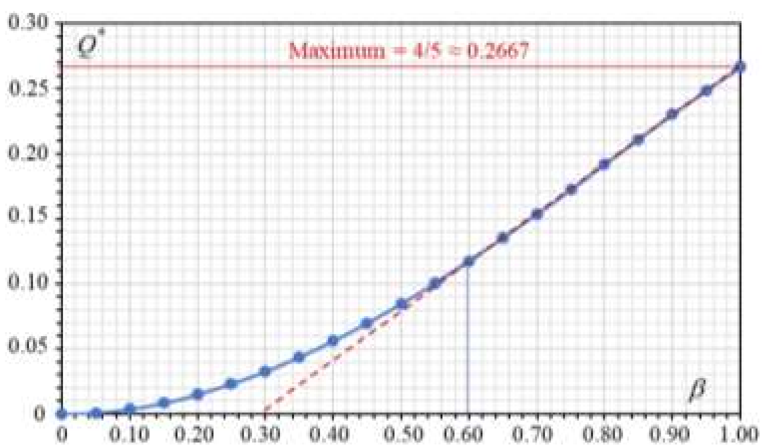

Figure A1-1: Variation in Q^* with respect to β, according to Table A1-1.

It can be observed from Fig. A2-1 that above about $\beta \approx 0.60$ the curve, expressed by the implicit Eq. (A1-2) is numerically almost linear, as shown by the dashed line. It does not become exactly a straight line, the kernel physics still apply, but over $0.60 \le \beta \le 1$ a line fits the Table A1-1 extremely well and is handy for quick calculations.

Consequently, one may derive a practical linear surrogate for $0.60 \le \beta \le 1$. Using the exact values in Table A1-1, a least-squares line constrained to pass through the endpoint $(\beta, Q^*) = (1, 4/15)$ gives the following:

$$Q^* \approx 0.3743\beta - 0.1063 \tag{A1-2a}$$

Eq. (A1-2a) was obtained with a coefficient of determination $R^2 = 0.99982$; when benchmarked against the exact values in Table A1-1, it yields a maximum relative error of less than 0.54% over $0.60 \le \beta \le 1$. The worst case occurs at $\beta = 0.60$.

Fig. A1-2 provides a clearer picture of how the deviations introduced by the approximate relationship (A1-2a) are distributed. By plotting, over $0.60 \le \beta \le 1$, the relative error computed as follows:

$$\varepsilon(\beta) = 100 \times \frac{\left| Q^*_{\text{approx}} - Q^*_{\text{exact}} \right|}{Q^*_{\text{exact}}}$$

it shows that discrepancies peak at $\beta = 0.60$ and remain below 0.54% across the interval, tapering toward zero near $\beta = 1$ because the line is constrained to pass through the endpoint $Q^*(1) = 4/15$.

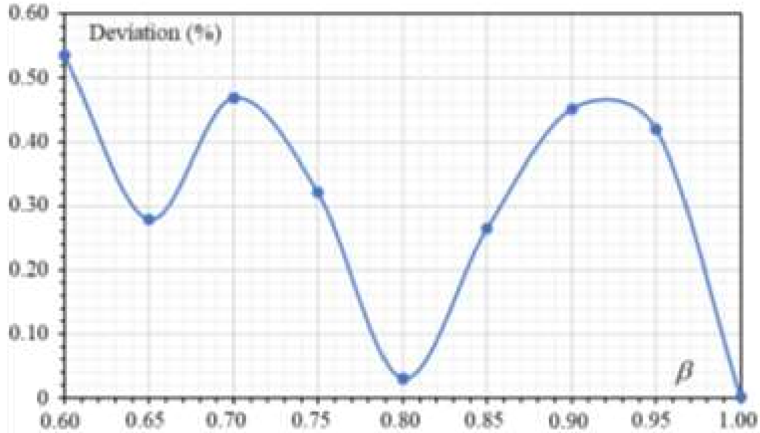

Figure A1-2: Deviation between the exact Eq. (A1-2) and the approximate Eq. (A1-2a) over $0.60 \le \beta \le 1$.

The authors explain the apparent linearity of the exact implicit relation (A1-2) over $0.60 \leq \beta \leq 1$ as follows:

For $\beta >\approx 0.60$, the kernel $\Psi(\beta)$ varies slowly and even turns slightly downward as $\beta \rightarrow 1$, while the prefactor $\beta^{3/2}$ in Eq. (A1-2) keeps rising. These opposing tendencies offset much of the curvature, leaving a near-constant slope in $Q^*(\beta)$ over this band, hence the visual straightness of the dashed trend. The law remains the same implicit relationship $Q^* = \beta^{3/2}\Psi(\beta)$; it's just *numerically* close to a line in this range. User must treat this as a convenience for $0.60 \leq \beta \leq 1$. If the user needs sub-0.05% kernel precision everywhere, the exact formula, or the paper's Padé kernel, remains the reference. Interpolation from Table A1-1 already yields very small errors; the line is most useful when the user wants a one-step, flow depth-to-discharge evaluator without Tables.

Inserting Eq. (A1-2a) into Eq. (A1-1a) yields the following theoretical approximate Q_{Th} relationship for the full elliptic weirs, valid over $0.60 \leq \beta \leq 1$:

$$Q_{Th} = \left[4b\sqrt{2g}\left(2a\right)^{3/2}\right]\left(0.3743\beta - 0.1063\right) \tag{A1-2b}$$

The semi-elliptic weir operating range is $\beta \leq 0.50$, so this linear shortcut, valid for $\beta \geq 0.60$, does not apply to the semi-elliptic case.

Although Eq. (A1-2b) does not have the usual Q–h form encountered in the field of flow measurement; it is still a stage–discharge relationship. It's the same rating recast in normalized stage, i.e., $\beta = h/(2a)$, and approximated over the upper range; since β is a one-to-one function of h for a given weir, one can always map it back to $Q(h)$.

As the ellipse approaches full submergence, $\beta \geq 0.60$, the aperture's incremental effective width gained by raising the flow depth shrinks, the geometry is "saturating", while the outer velocity/flow depth scale continues to grow. These opposing trends flatten the exact Q–h curve, making it almost linear in the normalized flow depth, hence the convenient upper-range approximation (A1-2b). It's the same physics encoded by the exact kernel and its compact surrogate; only the variable choice, β instead of h, and the local linearization change the look of the formula.

Use the exact Eq. (3a), or its compact Padé form, for an explicit $Q(h)$ anywhere; use Eq. (A1-2b) as a high-accuracy shortcut in its stated β-range. Both are stage-discharge laws; one is explicit in h, while the other is written in β but trivially mapped back via $\beta = h/(2a)$.

Circular weirs governing relationship

Combining the exact Eqs. (18) and (19), while considering $\xi = h/D$, one may easily obtain the following final result:

$$\xi^{3/2}\Psi\left(\xi\right) = Q^*_{\text{circular}} \tag{A1-2c}$$

where the relative discharge Q^* is expressed as follows:

$$Q^* = \frac{Q}{2\sqrt{2g}\, D^{5/2}} \tag{A1-1a}$$

Eq. (A1-2a) has exactly the same form as Eq. (A1-2); it is merely a variant. This is the essential reason why Table A1-1 also applies to the circular weir, where ξ spans the same admissible interval as β, namely [0, 1].

Similarly, Eq. (A1-1a) has exactly the same form as Eq. (A1-1); only the prefactor has changed. Moreover, Eq. (A1-1a) could have been readily be derived from Eq. (A1-1) by simply substituting $a = b = D/2$.

Using the prefactor expressed by Eq. (A1-1a); one may obtain the following theoretical approximate discharge Q_{Th} relationship for the circular weir, similar to Eq. (A1-2b):

$$Q_{Th} = 2\left(0.3743\xi - 0.1063\right)\sqrt{2g}\, D^{5/2} \tag{A1-2d}$$

Eq. (A1-2d) is valid over $0.60 \le \xi \le 1$:

Small-flow depth approximation (near the crest)

As $\beta \to 0$, the kernel enforces the incipient-submergence onset as follows:

$$\Psi(\beta) \sim (\pi/8)\sqrt{\beta} \qquad \text{(A1-4)}$$

Substituting this exact endpoint physics in Eq. (A1-2) and solving for β gives the following:

$$\beta \approx \sqrt{\frac{8}{\pi} Q^*} \tag{A1-5}$$

Eq. (A1-5) is only valid for $\beta << 1$.

This approximation is anchored in the manuscript's Euler–Beta series, which builds in the $(\pi/8) \times \sqrt{\beta}$ onset by construction.

Upper-range approximation (near full depth)

At complete wetting, the kernel takes the exact value $\Psi(1) = 4/15$. Approximating $\Psi(\beta) \approx 4/15$ in the neighborhood of $\beta \simeq 1$, Eq. (A1-2) yields the following:

$$\beta \approx \left(\frac{15}{4} Q^*\right)^{2/3} \tag{A1-6}$$

Eq. (A1-6) still valid only for $\beta < \approx 1$.

The full-height anchor Ψ(1) = 4/15 is explicitly stated and enforced by the exact kernel used in the paper.

Piecewise explicit rule and crossover

The two formulas, (A1-5) and (A1-6), provide a simple, explicit β–approximation across the range when used piecewise. Equating them and solving, they intersect at the following relative discharge:

$$\sqrt{\frac{8}{\pi}Q^*} = \left(\frac{15}{4}Q^*\right)^{2/3} \quad \text{(A1-7)}$$

After calculations, the following is obtained, where the subscript "Int" denotes "Intersect":

$$Q^*_{\text{Int}} \approx 0.0835 \quad \text{(A1-8)}$$

Inserting this result into Eq. (A1-5) or (A1-6), yields what follows:

$$\beta_{\text{Int}} \approx 0.461 \quad \text{(A1-9)}$$

Thus, a practical rule is the following:

$$\beta \approx \begin{cases} \sqrt{\frac{8}{\pi}Q^*} & Q^* \le Q^*_{\text{Int}} \\ \left(\frac{15}{4}Q^*\right)^{2/3} & Q^* > Q^*_{\text{Int}} \end{cases} \quad \text{(A1-10)}$$

This rule depends only on the manuscript's exact endpoint physics (no fitted parameters), and on the exact implicit relationship (A1-2).

This crossover has a clear physical interpretation: it marks the transition from the regime where crest (small-flow depth) physics controls the response to the regime where the deep, well-wetted behavior dominates. Below Q^*_{Int}, hence $\beta < \beta_{\text{Int}}$, the square-root onset captures the flow most faithfully; above Q^*_{Int}, hence $\beta > \beta_{\text{Int}}$, the full-flow depth trend is the better descriptor. Practically, Q^*_{Int} defines a convenient switch point for a piecewise explicit rule, as defined by Eq. (A1-10). At the switch, the two independent asymptotic descriptions agree, so the local errors are small and balanced.

The intersection also provides a useful design and computation threshold. In dimensional terms, it corresponds to the following when considering Eq. (A1-1):

$$Q_{\text{Int}} = 4b\sqrt{2g}\,(2a)^{3/2}\,Q^*_{\text{Int}} \quad \text{(A1-11)}$$

Q_{Int} is the actual at which the two endpoint-based, explicit β–Q^* formulas predict the same nondimensional depth β; concretely, t's defined by setting $Q = Q^*_{\mathrm{Int}}$ in the exact relationship (A1-2), where Q^*_{Int} is the constant given by Eq. (A1-8), i.e., 0.0835, and β_{Int} = 0.461 according to Eq. (A1-9). Substituting the value 0.0835 in Eq. (A1-11) yields the following:

$$Q_{\mathrm{Int}} = 0.334\, b\sqrt{2g}\left(2a\right)^{3/2} \tag{A1-12}$$

The corresponding depth is as follows:

$$h_{\mathrm{Int}} = 2a\beta_{\mathrm{Int}} \tag{A1-13}$$

Inserting the result given by Eq. (A1-9) into Eq. (A1-13) yields what follows:

$$h_{\mathrm{Int}} = 0.9222\, a \tag{A1-14}$$

Q_{Int} corresponds also to a flow depth of roughly 46% [Eq. (A1-9)] of the opening height. That single number is an excellent initial guess if one then refines β by solving the exact implicit equation; a single safeguarded Newton step typically suffices, since the rating is monotone and smooth. Finally, admissibility of the right-hand side is immediate from the kernel's endpoints: Q^* must lie in [0, 4/15]; this quick check screens inputs before computation and ensures a unique, physically meaningful solution for β.

Sanity checks and range

Because $0 \le \beta \le 1$ and $\Psi(1) = 4/15$, the right-hand side of the implicit Eq. (A1-2) must satisfy $0 \le Q^* \le 4/15$. This bound is convenient for quick consistency checks before solving or applying the approximations. The underlying discharge relationship is differentiable in closed form and exhibits positive elasticity throughout the range, so, the β-solution corresponding to a given Q^* is unique, with good numerical conditioning for any optional refinement by a single Newton step. The analysis below corroborates the preceding statement.

The admissible values of Q^* are constrained by the kernel's endpoint physics in the paper, i.e: as $\beta \to 0$, $\Psi(\beta) \sim (\pi/8) \times \sqrt{\beta}$, so $\beta^{3/2}\times\Psi(\beta) \to 0$; at full height $\beta = 1$, $\Psi(1) = 4/15$, giving $\beta^{3/2}\times\Psi(\beta) = 4/15$. Hence, a solvable Eq. (A1-2) right-hand side must lie within [0,4/15]; otherwise, no $\beta \in [0, 1]$ can satisfy the equation.

Role in implementation

The two explicit formulas, (A1-5) and (A1-6), are accurate near their respective endpoints and serve as excellent starting values for solving the exact implicit equation if a fully exact β is desired. The manuscript's Euler–Beta representation of Ψ ensures a closed, uniformly valid evaluator, and the accompanying Padé surrogate tracks it with a maximum uniform kernel deviation of about 0.04%, so a one-step refinement achieves essentially exact β while remaining computationally trivial.

THEORETICAL APPENDIX A2

For a circular sharp-crested weir of diameter D, it was shown by Amara and Achour (2021e) that the application of the energy equation between an upstream flow cross-section, in the rectangular approach channel of width B, and the weir crest, where the flow is in a critical state, yields the following dimensionless relationship:

$$h_1^{*\,3} - \left(\frac{3}{2}\right)^{6/5} \psi^{-3/5} h_1^{*\,2.1} + \frac{1}{2\left(1+P^*\right)^2} = 0 \qquad \text{(A2-1)}$$

where:

$$h_1^* = h_1 / h_{1c} \qquad \text{(A2-2)}$$

$$\psi = \frac{D}{B}\left(\frac{h_1}{D}\right)^{1/6} \qquad \text{(A2-3)}$$

$$P^* = P / h_1 \qquad \text{(A2-4)}$$

P^* is the dimensionless vertical contraction index parameter.

On the other hand, using the affinity propriety between ellipse and circle, one may replace the diameter D by the following:

$$2\sqrt{ab}$$

Thus, Eq. (A2-3) reduces to the following:

$$\psi = 2^{5/6} \frac{\sqrt{ab}}{B}\left(\frac{h_1}{\sqrt{ab}}\right)^{1/6} \qquad \text{(A2-5)}$$

Eq. (A2-5) can be rewritten in the following final form:

$$\psi = 2^{-1/6}\left(\frac{2b}{B}\right)\left(\frac{a}{b}\right)^{5/12}\left(\frac{h_1}{b}\right)^{1/6} \qquad \text{(A2-5a)}$$

It is emphasized to note that the ratio $2b/B$ is the dimensionless lateral contraction index parameter.

It is worth mentioning that this substitution is authorized by the fact that, in a critical regime, Q^2/g is proportional to A^3 as a dominant geometrical characteristic, where Q and A denote the discharge and the cross-wetted area, respectively. Thus, it is legitimate to privilege the equality of areas between the two cross-sections more than other characteristics. It is clear that a certain deviation from the exact relationship for the critical depth in the elliptical cross-section occurs, but this deviation will be dampened in the sense that a free correction function will be added at the end, to account for all the simplifying hypotheses introduced in the C_d derivation process.

Approximate solution

Eq. (A2-1) can be written in the following form:

$$h_1^{*3} - \varphi h_1^{*2.1} + \lambda = 0 \tag{A2-6}$$

where:

$$\varphi = \left(\frac{3}{2}\right)^{6/5} \psi^{-3/5} \tag{A2-7}$$

and

$$\lambda = \frac{1}{2\left(1+P^*\right)^2} \tag{A2-8}$$

Due to its implicit form, no closed form solution could be found. However, using perturbation method, it is possible to obtain an approximate solution to a suitable order for Eq. (A2-6). The application of the perturbation theory gives then the following second order approximation for the relative upstream flow h_1^*:

$$h_1^* = 0.5556\frac{\lambda^{4/3}}{\varphi^{10/3}} + 0.47619\frac{\lambda^{19/21}}{\varphi^{40/21}} + \left(\frac{\lambda}{\varphi}\right)^{1/2.1} \tag{A2-9}$$

Thus, given the values of both φ and λ, h_1^* is then worked out from Eq. (A2-9).

Stage-discharge and discharge coefficient relationships

The discharge Q law may be written as follows (Amara and Achour, 2021e):

$$Q = \frac{B\sqrt{g}}{h_1^{*3/2} h_1} h_1^{5/2} \tag{A2-10}$$

or as in the following form:

$$Q = \frac{\sqrt{2}}{2} \frac{B\sqrt{2g}}{h_1^{*\,3/2} h_1} h_1^{5/2} \tag{A2-10a}$$

After rearrangement, Eq. (A2-10a) can be rewritten as follows:

$$Q = \frac{\sqrt{2}}{(2b/B)(h_1/b)\,h_1^{*\,3/2}} \sqrt{2g}\, h_1^{5/2} \tag{A2-10b}$$

Eq. (A2-10b) adopts the canonical stage–discharge form for a weir, which reads as follows:

$$Q = C_d \sqrt{2g}\, h_1^{5/2} \tag{A2-11}$$

where C_d is the discharge coefficient of the weir, expressed as follows:

$$.\,C_d = \frac{\sqrt{2}}{(2b/B)(h_1/b)\,h_1^{*\,3/2}} \tag{A2-12}$$

Eq. (A2-12) is the governing C_d-formulation for the elliptic weirs' geometry. In light of this equation, the following observations merit emphasis:

(a) Consistent with dimensional analysis, the discharge coefficient C_d is affected by h_1/b rather than h_1/B. In addition, the reliance of C_d on h_1/b follows directly from Eq. (A2-12), and indirectly through φ and ψ, as established by Eqs. (A2-7) and (A2-5a).

(b) The discharge coefficient C_d depends on the dimensionless lateral-contraction index $2b/B$, directly via Eq. (A2-12), and indirectly through ψ and h^*_1, as established by Eqs. (A2-5a) and (A2-9), respectively.

(c) The discharge coefficient C_d depends on the dimensionless vertical contraction index parameter $P^* = P/h_1$, implicitly through λ and h^*_1 as it can be seen in Eqs. (A2-8) and (A2-9), respectively.

(d) The lateral and vertical contraction index parameters affect the discharge coefficient C_d separately, contrary to the prediction of dimensional analysis, which indicates that these two influential parameters should be combined into a single compound parameter, such as the following:

$$\Gamma = \frac{2b/B}{1 + P/h_1} \tag{A2-13}$$